



HAL
open science

Surgery of the anterior segment of the eye assisted by ultrashort pulse laser: optimisation of the parameters with respect to tissular transparency and cell viability

Syed Asad Hussain

► To cite this version:

Syed Asad Hussain. Surgery of the anterior segment of the eye assisted by ultrashort pulse laser: optimisation of the parameters with respect to tissular transparency and cell viability. Physics [physics]. École Polytechnique, 2014. English. NNT: . tel-01097301

HAL Id: tel-01097301

<https://hal.science/tel-01097301>

Submitted on 6 Jan 2015

HAL is a multi-disciplinary open access archive for the deposit and dissemination of scientific research documents, whether they are published or not. The documents may come from teaching and research institutions in France or abroad, or from public or private research centers.

L'archive ouverte pluridisciplinaire **HAL**, est destinée au dépôt et à la diffusion de documents scientifiques de niveau recherche, publiés ou non, émanant des établissements d'enseignement et de recherche français ou étrangers, des laboratoires publics ou privés.



Distributed under a Creative Commons Attribution - NonCommercial - NoDerivatives 4.0 International License

Thèse
Présentée pour l'obtention du titre de
Docteur es Science de l'École Polytechnique
Spécialité : Physique

Par
Syed Asad Hussain

**Surgery of the anterior segment of the eye assisted by
ultrashort pulse laser: optimisation of the parameters
with respect to tissular transparency and cell viability.**

Soutenue le :
19 Septembre 2014

Jury composé de :

THURET Gilles	Rapporteur
TUALLE Jean-Michel	Rapporteur
DRUON Frédéric	
GEORGES Gaëlle	
SCHANNE-KLEIN Marie-Claire	
PLAMANN Karsten	Directeur de thèse

**Préparée au Laboratoire d'Optique Appliquée
ENSTA ParisTech – École Polytechnique – CNRS UMR 7639
Palaiseau, France**

Abstract

The goal of this work was to study different microscopic and macroscopic effects that will ultimately help us to improve procedures in eye surgery assisted by ultrashort pulse lasers and most notably keratoplasty (corneal grafting), which requires laser systems which are operational in pathological and therefore strongly light scattering tissue. Previously, the Optique Photonique Santé (OPS) group at the Laboratoire d'Optique Appliquée (LOA) had identified 1650 nm as an optimum wavelength at which light scattering processes inside the pathological cornea are minimised.

During the present thesis, three main tasks have been addressed.

- An ultrashort pulse laser system based on non-linear optical crystals has been developed, optimised with respect to the requirements of laser eye surgery, and fully characterised. The finished set-up is compact, robust, simple and potentially qualified for clinical use.
- In collaboration with a group at IESL-FORTH (Iraklion, Greece) and with the participation of a previous PhD student of the group we have studied the interaction of ultrashort pulses with water, collagen (type I) solution and porcine cornea. Data on laser-tissue-interaction is precious because the interaction dynamics is usually only documented for water; our results will help to develop a tissue-specific model for the interaction process.
- We have investigated the interaction of the laser pulses and the effects it causes with live cells in the corneal endothelium. The preservation of endothelial cell viability is crucial notably for specific keratoplasty routines which require incisions close to the endothelium; compromised endothelial cell viability – which is likely caused by the effects of shock waves generated by optical breakdown and bubble formation – may lead to a failure of the surgical intervention. “Safe” sets of parameters concerning pulse energy and incision geometry need to be defined. We explored the maximum permitted pulse energy values at any given distance to the endothelial cells and minimal distances for given pulse energies and estimated the associated shock wave amplitudes.

Résumé

Le but de ce travail a été d'étudier les différents effets microscopiques et macroscopiques susceptibles de nous aider à améliorer les procédures de chirurgie oculaire assistée par les lasers à impulsions ultra-courtes ; plus particulièrement en kératoplastie (greffe de cornée), qui nécessite des systèmes lasers opérationnels dans les tissus pathologiques et donc de diffusant fortement la lumière. Antérieurement, le groupe Optique Photonique Santé (OPS) du Laboratoire d'Optique Appliquée (LOA) a identifié 1650 nm comme étant une longueur d'onde optimale à laquelle les processus de diffusion de la lumière à l'intérieur de la cornée pathologique sont minimisés.

Au cours de cette thèse, trois tâches principales ont été abordées.

- Un système laser à impulsions ultra-courtes à base de cristaux optiques non linéaires a été mis au point, optimisée par rapport aux exigences de chirurgie oculaire au laser, et entièrement caractérisé. Le montage achevé est compact, robuste, simple et potentiellement apte à un usage en clinique.
- En collaboration avec un groupe de l'IESL- FORTH (Iraklion, Grèce) et avec la participation d'un ancien doctorant du groupe, nous avons étudié l'interaction des impulsions ultra-brèves avec de l'eau, une solution de collagène (type I) et des cornées de porcs. Les données sur les interactions laser-tissu sont précieuses car la dynamique d'interaction est habituellement uniquement documentée pour l'eau; nos résultats aideront à élaborer un modèle spécifique de tissu pour le processus d'interaction.
- Nous avons étudié l'interaction entre les impulsions laser et les effets causés sur des cellules vivantes de l'endothélium cornéen. La préservation de la viabilité des cellules endothéliales est cruciale, notamment pour les routines de kératoplastie spécifiques exigeant des incisions à proximité de l'endothélium ; la viabilité des cellules endothéliales compromise – probablement causée par les effets des ondes de choc générées par claquage optique et la formation de bulles – peut conduire à un échec de l'intervention chirurgicale. Des jeux de paramètres « saufs » concernant l'énergie d'impulsion et de la géométrie de l'incision doivent être définis. Nous avons ainsi exploré les valeurs maximales autorisées de l'énergie de l'impulsion à une quelconque distance donnée des cellules endothéliales et les distances minimales pour les énergies d'impulsions données, et estimé les amplitudes des ondes de choc associées.

Acknowledgements

I would first like to thank Allah for everything that he has given to me. I would like to thank Karsten Plamann for giving me an opportunity to complete my PhD under his supervision. His constant guidance, support and encouragement made this dissertation possible.

Thank you also to Antoine Rouse, Carole Gratpanche, Sandrine Tricaud, Patricia Toullier, Octavie Verdun, and Lucie Huguet for their help and providing a great research environment.

I am thankful to Gilles Thuret, Jean-Michel Tualle, Druon Frédéric, Georges Gaëlle, Schanne-Klein Marie-Claire (jury members) for their valuable time and suggestions.

Then I would like to thank Caroline Crotti and Laura Kowalczyk for technical guidance and assistance during my PhD especially in my early months. Thank you also to Tal Marciano for his scientific discussion and the great time that we spend together. A big thank you to Fatima Alahyane and Zacaria Essaïdi for their help and suggestions. I admire your ability to come up with quick solutions for the various technical as well as administrative problems.

In addition, I would like to thank Stelios Tzortzakis, Dimitris G. Papazoglou and Michalis Loulakis for their help on our experiment on Dynamics of fs pulse interaction with corneal tissue and a collagen (type I) solution. Without their razor sharp knowledge of the field the experiment may not be possible. Thanks also to Marc Hanna for his advice and help for our parametric amplification and generation setup.

Thanks to Florent Deloison and H el ene Desrus for their time and interest during my whole stay at ALPhANOV.

I also would like to thank Arnaud Dubois, Philippe Gain, Zhiguo He, Valeria Nuzzo, Donald Peyrot, Mich ele Savoldelli, Iman Aloulou, Isabelle Tang, Mikael Guedj, Maxence Le Sourd, Charles Chalbot, Smail Khelifati, Jean-Pascal Caumes, Denis Tregogat, Florent Guichard, and Antoine Federici who have helped me on various occasions on various aspects during the past three years.

I have to specially thank Micka el Martinez and Jean-Lou Charles for helping me on various technical problems involving mechanics in my experiments.

I would like to thank the  cole Polytechnique graduate school for providing me funding for my PhD, LaserLab for funding our experiment at UNIS Heraklion, Greece. The seventh framework programme of the European Union for funding the acquisition of an infrared camera through their NEXPRESSO program.

At the end, I like to thank my family and friends for their support, prayers and encouragement in all my endeavours.

Table of contents

INTRODUCTION	16
SCIENTIFIC OBJECTIVES.....	17
THESIS PLAN	18
CHAPTER I	20
ANATOMY AND OPTICAL PROPERTIES OF THE CORNEA.....	20
1.1 THE HUMAN EYE.....	21
1.2 THE ANATOMY OF THE CORNEA	23
1.2.1 Epithelium.....	24
1.2.2 Bowman’s layer	24
1.2.3 Stroma	25
1.2.4 Dua’s layer.....	27
1.2.5 Descemet’s membrane	27
1.2.6 Endothelium	27
1.3 OPTICAL PROPERTIES OF CORNEA	28
1.3.1. Refractive index	28
1.3.2. Birefringence	29
1.3.3. Transmission and scattering.....	29
1.4 ANATOMICAL DIFFERENCES BETWEEN HUMAN AND PORCINE CORNEAS	34
1.5 SURGICAL ROUTINES FOR THE ANTERIOR SEGMENT OF THE EYE ASSISTED BY ULTRASHORT LASER PULSES	35
1.6 CONCLUSION	37
CHAPTER II	38
ULTRASHORT PULSE LASERS AND OPTICAL PARAMETRIC CONVERSION	38
2.1 ULTRASHORT LASER PULSES: THEORY	39
2.2 MODE LOCKING	40
2.2.1 Active mode locking.....	41
2.2.2 Passive mode locking.....	41
2.3 ARCHITECTURES OF ULTRASHORT PULSE LASER SYSTEMS.....	42
2.3.1 Long oscillator	42
2.3.2 Chirped pulse amplification	43
2.3.2.1 Regenerative amplifier	44
2.3.2.2 CPA based on optical fibres	44
2.4 GAIN MEDIA.....	45
2.5 WAVELENGTH CONVERSION BY NON-LINEAR OPTICS.....	46
2.5.1 Second order non-linear susceptibility.....	46
2.5.2 Coupled wave equations.....	48
2.5.3 Non-linear optical crystals.....	49
2.6 PHASE MATCHING	50
2.6.1 Birefringent phase matching	51
2.6.2 Quasi phase matching	51
2.7 OPTICAL PARAMETRIC PROCESSES.....	53
2.7.1 Optical parametric generation (OPG).....	53
2.7.2 Optical parametric amplification (OPA)	55
2.8 CONCLUSION.....	56

CHAPTER III	58
INTERACTION OF ULTRASHORT LASER PULSES WITH CORNEAL TISSUE.....	58
3.1 MECHANISMS OF LASER-TISSUE INTERACTION	59
3.1.1 Photochemical interaction.....	59
3.1.2 Photothermal interaction	60
3.1.3 Photoablation	60
3.1.4 Plasma induced ablation and photodisruption.....	60
3.2 NON-LINEAR OPTICAL BREAKDOWN IN TISSUE	60
3.2.1 Multiphoton ionisation (MPI)	61
3.2.2 Tunneling.....	61
3.2.3 Rate equation	63
3.2.4 Breakdown criterion	64
3.3 MECHANICAL EFFECTS ASSOCIATED WITH THE NON-LINEAR OPTICAL BREAKDOWN.....	65
3.4 CONCLUSION.....	69
CHAPTER IV.....	72
OPTICAL PARAMETRIC GENERATOR AND AMPLIFYER BASED ON A PERIODICALLY POLED MAGNESIUM DOPED LITHIUM NIOBATE CRYSTAL EMITTING MICROJoule FEMTOSECOND PULSES IN THE SHORT WAVE INFRARED	72
4.1 ABSTRACT	72
4.2 INTRODUCTION.....	72
4.3 OPTICAL PARAMETRIC GENERATOR (OPG).....	75
4.3.1 Experimental Setup.....	75
4.3.2. Results and Discussion.....	76
4.4 OPTICAL PARAMETRIC AMPLIFICATION (OPA).....	81
4.4.1 Experimental Setup.....	81
4.4.2 Results and Discussion.....	82
4.5 CONCLUSION.....	87
CHAPTER V	88
CELL VIABILITY IN THE ENDOTHELIUM OF PORCINE CORNEA EXPOSED TO ULTRASHORT LASER PULSES AT 1030 NM.	88
5.1 ABSTRACT	88
5.2 INTRODUCTION.....	88
5.3 MATERIALS AND METHODS.....	89
5.4 RESULTS AND DISCUSSION	98
5.5 CONCLUSION.....	105
CHAPTER VI.....	106
DYNAMICS OF FS PULSE INTERACTION WITH CORNEAL TISSUE AND A COLLAGEN (TYPE I) SOLUTION	106
6.1 ABSTRACT	106
6.2 INTRODUCTION.....	106
6.3 EXPERIMENTAL TECHNIQUE	107
6.3.1 Sample preparation	107
6.3.2 Experimental set-up.....	108
6.4 RESULTS AND DISCUSSION.....	109
6.5 CONCLUSION.....	114

CONCLUSION AND OUTLOOK.....	116
A. RESULTS AND CONCLUSION	116
<i>Development of femtosecond laser source</i>	<i>116</i>
<i>Cell viability in the endothelium of porcine cornea exposed to ultrashort laser pulses.....</i>	<i>117</i>
<i>Dynamics of fs pulse interaction with water, corneal tissue and a collagen (type I) solution.....</i>	<i>117</i>
B. FUTURE WORK.....	118
APPENDIX 1: TRANSPARENCY OF PORCINE LENS	120
APPENDIX 2: KERR EFFECT.....	126
APPENDIX 3: TRANSPARENCY OF HIGH PASS FILTER	127
APPENDIX 4: NEXPRESSO PROJECT	128
REFERENCES.....	142

List of figures

CHAPTER I

FIG. 1. 1: CROSS SECTIONAL AND EN FACE VIEW OF THE HUMAN EYE [MUS].	22
FIG. 1. 2: (A) HISTOLOGY OF HUMAN CORNEA (SCALE BAR = 30 MM) (B) HUMAN CORNEA (MICHELE SAVOLDELLI, HOPITAL HOTEL DIEU DE PARIS) [PLA10].	24
FIG. 1. 3: PRESENCE OF KERATOCYTE INSIDE THE STROMA SCALE BAR 10 MM (MODIFIED FROM [SSA06]).	25
FIG. 1. 4: REPRESENTATION OF THE TROPICOLLAGEN (TC) MOLECULE (A), DIFFERENT ARCHITECTURAL LEVELS OF THE COLLAGEN STRUCTURE OF THE SCLERA (B) (MODIFIED FROM [VOG03]).	26
FIG. 1. 5: LAMELLAR ORIENTATION INSIDE CORNEAL STROMA (A) [CBO05], CROSS SECTION OF CORNEA WHICH REPRESENT ORIENTATION OF CORNEAL LAMELLAR (B) (SCALE BAR 1 μ M) [CAR].	27
FIG. 1. 6: ENDOTHELIAL CELLS AND THEIR PUMP AND LEAK MECHANISM [NID] [GOW82].	28
FIG. 1. 7: DIFFERENCE BETWEEN CLEAR AND OEDEMATOUS CORNEA [PLA10].	30
FIG. 1. 8: A COMPARISON OF CLEAR AND OEDEMATOUS CORNEA. KERATOCYTES AND LAKES ARE VISIBLE IN THE OEDEMATOUS CORNEA (MICHÈLE SAVOLDELLI, HÔPITAL-HÔTEL DIEU DE PARIS).	31
FIG. 1. 9: EXPERIMENTAL SET-UP TO MEASURE THE (A) CORNEA SANDWICHED BETWEEN TWO LENS PAIRS, (B) TOTAL TRANSMISSION (TT), (C) DIRECT TRANSMISSION (TD) OF TISSULAR SAMPLES. (W-HAL=HALOGEN LIGHT SOURCE) [DAP10].	32
FIG. 1. 10: TOTAL, DIRECT AND SCATTERING OF A 450 μ M THICK CORNEA.	33
FIG. 1. 11: PERCENT OF SCATTERING FOR DIFFERENT WAVELENGTHS AT DIFFERENT THICKNESSES [DAP10].	34
FIG. 1. 12: FEMTOSECOND LASER PRODUCING INCISION INSIDE CORNEA [STO].	35
FIG. 1. 13: DIFFERENT SURGICAL PROCEDURES FOR WHICH FEMTOSECOND LASERS CAN BE USE [PLA10].	36
FIG. 1. 14: FEMTOSECOND SYSTEMS THAT CAN BE USED FOR THE ANTERIOR SEGMENT OF THE EYE.	37

CHAPTER II

FIG.2. 1: MODES INSIDE THE CAVITY COVERED BY THE LASER GAIN MEDIUM (A), TEMPORAL PROFILE OF THE PULSE WHEN THE LASER IS MODE LOCKED (B) (MODIFIED FROM [UKR03]).	41
FIG.2. 2: TI:SAPPHIRE OSCILLATOR BASED ON KERR LENS MODE LOCKING (MODIFIED FROM [DGE06]).	42
FIG.2. 3: SCHEMATIC OF MULTIPLE-PASS CAVITY (MODIFIED FROM [SHC99]).	43
FIG.2. 4: SCHEMATIC DIAGRAM FOR CHIRPED PULSE AMPLIFICATION (MODIFIED FROM [LLN95]).	43
FIG.2. 5: CHIRPED PULSE AMPLIFICATION BASED ON REGENERATIVE AMPLIFICATION.	44
FIG.2. 6: CHIRPED PULSE AMPLIFICATION BASED ON LMA FIBRE [PLA10].	45
FIG.2. 7: INTENSITY OF THE CONVERTED OPTICAL INTENSITY VERSUS CRYSTAL LENGTH (A) PHASE MATCHING, (B) QUASI-PHASE MATCHING SCHEMES AND (C) NO PHASE MATCHING.	51
FIG.2. 8: PERIODIC POLING FOR QUASI PHASE MATCHING. IN ORDER TO COMPENSATE THE PHASE SHIFT OF π THE FERRO-ELECTRIC DOMAINS SHOULD BE FLIPPED AFTER EVERY COHERENCE LENGTH (L_c).	52
FIG.2. 9: ENERGY LEVEL SCHEME FOR OPTICAL PARAMETRIC GENERATION (OPG).	53
FIG.2. 10: OPTICAL PARAMETRIC GENERATION. ω_P, ω_S , AND ω_I ARE PUMP, SIGNAL AND IDLER FREQUENCIES (SEE TEXT FOR DETAIL).	54
FIG.2. 11: OPTICAL PARAMETRIC AMPLIFICATION. ω_P, ω_S , AND ω_I ARE PUMP, SIGNAL AND IDLER FREQUENCIES (SEE TEXT FOR DETAIL).	55

CHAPTER III

FIG. 3. 1: CLASSIFICATION OF DIFFERENT INTERACTION REGIMES DEPENDING ON POWER DENSITY AND EXPOSURE TIME. THE CIRCLES INDICATE THE ORDERS OF MAGNITUDE OF EXPOSURE TIME AND POWER DENSITY TYPICAL FOR DIFFERENT TYPES OF INTERACTIONS. MODIFIED FROM [MHN93].	59
FIG. 3. 2: FREE ELECTRON GENERATION (A) MULTIPHOTON IONISATION; (B) TUNNELING IONISATION; (C) COMBINED MULTIPHOTON EXCITATION AND TUNNELING (SEE TEXT). MODIFIED FROM [CBS01].	61
FIG. 3. 3: DIFFERENT PHYSICAL PROCESSES THAT CAN LEAD TO THE GENERATION OF A FREE ELECTRON. AN ELECTRON IN THE VALENCE BAND CAN BE ELEVATED INTO THE CONDUCTION BAND BY MULTIPHOTON IONISATION OR TUNNELING. ONCE IN THE CONDUCTION BAND, IT CAN ABSORB PHOTONS THROUGH INVERSE BREMSSTRAHLUNG. IF ENERGY IS SUFFICIENT IT IS POSSIBLE FOR THE ELECTRON TO EXTRACT ANOTHER ELECTRON FROM THE VALENCE BAND COLLISION. THE RESULTING TWO ELECTRONS MAY REPEAT THE PROCESS AND THEREBY LEAD TO THE FURTHER GENERATION OF AN "AVALANCHE" OF FREE ELECTRONS THROUGHOUT THE VOLUME OF THE LASER FOCUS. (MODIFIED FROM [VOG05]).	62
FIG. 3. 4: FRACTION OF FREE ELECTRONS (IN PERCENT) AS A FUNCTION OF TEMPERATURE. ρ_{therm} AND ρ_{bound} REPRESENT THERMALLY GENERATED ELECTRON DENSITY AND BOUND ELECTRON DENSITY [NOB10].	63
FIG. 3. 5: NUMERICALLY CALCULATED THRESHOLD RADIANT EXPOSURE FOR DIFFERENT PULSE DURATIONS [VOG05].	65
FIG. 3. 6: THRESHOLD ENERGY DENSITY FOR BUBBLE FORMATION IN WATER. (SEE TEXT FOR DETAIL, DATA FROM [NOB10]).	66
FIG. 3. 7: ABLATION THRESHOLD OF PORCINE CORNEAL STROMA ASSISTED BY FEMTOSECOND LASER PULSES FOR DIFFERENT WAVELENGTHS [GOL08].	67
FIG. 3. 8: SHOCK WAVE AMPLITUDE AT DIFFERENT TIMES IN RADIAL (R) AND AXIAL (Z) DIRECTIONS WHERE Z REPRESENT OPTICAL AXIS, DESCRIPTION OF AXIAL AND RADIAL DIRECTION USE IN THE SIMULATION(A), SHOCK WAVE AMPLITUDE IN RADIAL DIRECTION (B), SHOCK WAVE AMPLITUDE IN AXIAL DIRECTION (C) (MODIFIED FROM [VOG05]).	68
FIG. 3. 9: BUBBLE DYNAMICS (A) BUBBLE SIZE \ll FOCAL VOLUME, (B) BUBBLE SIZE \geq FOCAL VOLUME.	69

CHAPTER IV

FIG. 4. 1: SCHEMATIC OF THE OPG SET-UP: THE LENS L FOCUSES THE PUMP BEAM INSIDE THE CRYSTAL. THE GENERATED SIGNAL PASSED THROUGH THE HIGH PASS FILTER FOLLOWED BY THE DETECTOR.	75
FIG. 4. 2: SIGNAL AND IDLER PULSE ENERGY VERSUS INPUT ENERGY MEASURED AND CORRECTED FOR TWO DIFFERENT GRATINGS ON EACH CRYSTAL: CRYSTAL A (A), CRYSTAL B (B).	77
FIG. 4. 3 (A) - (B): OPG SPECTRUM MEASURED FOR CONSTANT GRATING AT DIFFERENT TEMPERATURE: 30.46 μm FOR CRYSTAL A (A) 26 μm FOR CRYSTAL B (B).	78
FIG. 4. 4 (A) - (B): OPG SPECTRUM MEASURED FOR DIFFERENT GRATINGS AT CONSTANT TEMPERATURE OF 100°C FOR CRYSTAL A (A) AND B (B).	79
FIG. 4. 5 (A) - (B): TEMPERATURE TUNING CURVES MEASURED FOR DIFFERENT GRATINGS: CRYSTAL A (29.37, 29.60, 29.86, 30.13, 30.46, 30.84 μm)(A) CRYSTAL B (24, 24.5, 25, 25.5, 26, 26.5 μm)(B).	80
FIG. 4. 6: SCHEMATIC OF THE OPA SET-UP: STAGE1 CONTAINS M1, BEAM SPLITTING CUBE, A1, NONLINEAR CRYSTAL (PPMLN1), HIGH PASS FILTER, A3, BANDPASS FILTER, M2, A4 AND M3. STAGE2 CONTAINS M1, BEAM SPLITTING CUBE, M4, A2, DELAY LINE, M5, M6, M7, NONLINEAR CRYSTAL (PPMLN2), WHERE M1- M7 ARE MIRRORS AND A1, A2, A4 ARE FOCUSING AND A3, A5 ARE RECOLLIMATION LENS. M2, M3, M6 ARE DICHROIC MIRRORS AND M2 M3 ARE HIGHLY REFLECTIVE AT SIGNAL FREQUENCY.	82
FIG. 4. 7: COMPARISON OF SLOPES WHEN DIFFERENT CONFIGURATIONS WERE CONSIDERED: OPG (SQUARE), OPA WITH BAND PASS FILTER (CIRCLE) AND OPA WITHOUT BAND PASS FILTER (TRIANGLE) DATA POINTS WERE OBTAINED FOR CRYSTAL A.	83
FIG. 4. 8: SPECTRA OBTAINED IN DIFFERENT OPG AND OPA CONFIGURATIONS. OPG WITH AND WITHOUT BAND PASS FILTER (A), OPA WITH AND WITHOUT BAND PASS FILTER PLUS THE SPECTRUM OF PPMLN2 WITHOUT SEED SIGNAL FROM PPMLN1 (B).	84
FIG. 4. 9: SPATIAL PROFILES (A) PUMP, (B) SEED WITHOUT FILTER, (C) SEED WITH FILTER, (D) OPA WITHOUT FILTER, (E) OPA WITH FILTER, (F) PPMLN2 (OPG AND OPA SIGNALS WERE MEASURED AT A DISTANCE OF 400 MM AWAY FROM THE CRYSTAL).	85
FIG. 4. 10: COMPARISON OF THE SLOPES FOR OPG (SQUARE) AND AMPLIFICATION DUE TO CONTINUUM GENERATION (CIRCLE).	86
FIG. 4. 11: SCHEMATIC OF OPTICAL PARAMETRIC CHIRPED PULSE AMPLIFICATION (OPCPA).	87

CHAPTER V

Fig. 5. 1: SCHEMATIC OF THE EXPERIMENTAL SETUP: BE= BEAM EXPANDER, EL= EPITHELIAL LAYER, S= STROMA , DM= DESCEMET’S MEMBRANE, E= ENDOTHELIUM, D= DISTANCE BETWEEN LASER SPOT AND ENDOTHELIUM CELLS. M1-M3 ARE MIRRORS.	90
Fig. 5. 2: CONTROL CORNEA WITHOUT ANY INCISION/S OBSERVED BY THE MICROSCOPE (NIKON AZ-100) (A) USING THE THREE DIFFERENT MAGNIFICATIONS X2, X4 AND X8 (FIRST, SECOND, AND THIRD ROWS). GREEN (LIVING CELLS) (B), RED (DEAD CELLS) (C), BLUE (NUCLEI OF ALL THE ENDOTHELIAL CELLS)(D). NUCLEI VISIBILITY WITH RESPECT TO DIFFERENT MAGNIFICATION(E). SCALE BAR=1500µM, WHERE THE BLACK PART IN THE FLUORESCENCE IMAGE SHOWS ABSENCE OF ENDOTHELIAL CELLS.	92
Fig. 5. 3: TREATED CORNEA WITH LASER PULSES THAT MAKES A LAMELLAR INCISION OF 1000x1000µM ² INSIDE THE VOLUME OF CORNEA. FLUORESCENCE IMAGE OBSERVED BY THE MICROSCOPE (NIKON AZ-100) (A), GREEN (LIVING CELLS) (B), RED (DEAD CELLS) (C), BLUE (NUCLEI OF ALL THE ENDOTHELIAL CELLS)(D). NUCLEI VISIBILITY WITH RESPECT TO DIFFERENT MAGNIFICATION (E). SCALE BAR=1500µM, WHERE THE BLACK PART IN THE FLUORESCENCE IMAGE SHOWS ABSENCE OF ENDOTHELIAL CELLS. ...	94
Fig. 5. 4: SCHEMATIC OF THE EXPERIMENTAL SETUP: BE= BEAM EXPANDER, EL= EPITHELIAL LAYER, S= STROMA , DM= DESCEMET’S MEMBRANE, E= ENDOTHELIUM, D= DISTANCE BETWEEN LASER SPOT AND ENDOTHELIUM CELLS. M1-M3 ARE MIRRORS.	95
Fig. 5. 5: CONTROL CORNEA WITHOUT INCISION/S. THE CONTROL CORNEAS CLEARLY SHOW A UNIFORM GREEN AREA COVERED WITH LIVE CELLS WITH VERY FEW DEAD CELLS AT THE PERIPHERY WHICH ARE MAINLY DUE TO THE TREATMENT/HOLDER OF THE CORNEA. SCALE BAR=1500µM	95
Fig. 5. 6: TREATED CORNEA WITH LASER PULSES THAT MAKES A LAMELLAR INCISION OF 500x2000µM ² INSIDE THE VOLUME OF CORNEA (TOTAL FIVE IN NUMBER AS SHOWN IN FIGURE). FLUORESCENCE IMAGE OBSERVED BY THE MICROSCOPE (NIKON AZ-100) (A), GREEN (LIVING CELLS) (B), RED (DEAD CELLS) (C), BLUE (NUCLEI OF ALL THE ENDOTHELIAL CELLS)(D). NUCLEI VISIBILITY WITH RESPECT TO DIFFERENT MAGNIFICATION (E). SCALE BAR=1500µM, WHERE THE BLACK PART IN THE FLUORESCENCE IMAGE SHOWS ABSENCE OF ENDOTHELIAL CELLS.....	96
Fig. 5. 7: DIFFERENT STEPS IN IMAGE ANALYSIS: (A) THE INCISION AREA IS DIVIDED INTO 5 PARTS; (B) ONE IMAGE IS SELECTED FROM THE SET, (C) THE GRAY SCALE HISTOGRAM SHOWS TWO PEAKS, ONE FOR THE FLUORESCENCE OF THE LIVE CELLS AND THE OTHER FOR THE RESIDUAL LIGHT INTENSITY CORRESPONDING TO THE AREA WITHOUT LIVE CELLS; A POINT WHERE IT WAS POSSIBLE TO DISTINGUISH LIVE AREA FROM THE AREA WITHOUT SURVIVING CELLS WAS CHOSEN AS THRESHOLD, (D) THE AREA OCCUPIED BY LIVE CELLS IS SHOWN IN BLACK WHILE THE AREA DEVOID OF LIVE CELLS IS SHOWN IN WHITE. THE PERCENTAGE OF THE AREA OCCUPIED BY LIVE CELLS WITH RESPECT TO THE TOTAL AREA MAY THEN BE CALCULATED. UNDER THE PLAUSIBLE ASSUMPTION OF CONSTANT CELL DENSITY OVER THE ROI, THIS GIVES THE PERCENTAGE OF SURVIVING CELLS. THE PROCESS IS THEN REPEATED FOR THE REST OF THE ROI TO OBTAIN A MEAN VALUE AND THEIR STANDARD DEVIATION.	97
Fig. 5. 8: PERCENTAGE OF SURVIVING ENDOTHELIAL CELLS FOR INCISIONS PERFORMED AT PULSE ENERGIES OF 16.5µJ AT VARIABLE DISTANCES FROM THE ENDOTHELIUM (A), AVERAGE VALUES AND ESTIMATED SHOCK WAVE AMPLITUDE (B).	99
Fig. 5. 9: PERCENTAGE OF SURVIVING CELLS FOR INCISIONS PERFORMED AT A DISTANCE OF 50 µM FROM THE ENDOTHELIUM AT VARIABLE PULSE ENERGIES (A), AVERAGE VALUES AND ESTIMATED SHOCK WAVE AMPLITUDE (B).....	100
Fig. 5. 10: DECREASE OF RADIAN EXPOSURE VERSUS DEPTH.....	101
Fig. 5. 11: BY MAKING INCISIONS WITH DIFFERENT ENERGY VALUES WILL RESULT IN DIFFERENT INCISION LENGTH, MAKING A FIT TO THESE VALUES WILL RESULT IN PENETRATION DEPTH [CCR13].....	102
Fig. 5. 12: STRESS-WAVE AMPLITUDE AT A DISTANCE OF 6MM (IN MPA) FOR DIFFERENT PULSE DURATIONS AS A FUNCTION OF DIMENSIONLESS LASER PULSE ENERGY WHERE THE RED LINE REPRESENT THE LINEAR FIT FOR THE PULSE DURATION OF OUR LASER SOURCE [Vog05].....	102
Fig. 5. 13: DIFFERENT STEPS TO ESTIMATION SHOCK WAVE AMPLITUDE.	104

CHAPTER VI

Fig. 6. 1: PUMP-PROBE EXPERIMENTAL SETUPS, WITH AN INTEGRATED IN-LINE HOLOGRAPHIC MICROSCOPE FOR THE OBSERVATION OF THE TRANSIENT DYNAMICS IN THE FOCAL AREA (A) TRANSVERSE PUMP-PROBE GEOMETRY FOR THE COLLAGEN SOLUTION (B) TILTED 45° GEOMETRY IN A STRONGLY SCATTERING CORNEA SAMPLE.	107
Fig. 6. 2: NORMALIZED ABSORPTION SIGNAL IN THE EXCITATION AREA (A) SPATIOTEMPORAL EVOLUTION OF THE EXCITATION IN THE CORNEA (B) COMPARATIVE TEMPORAL EVOLUTION OF THE NORMALIZED ABSORPTION SIGNAL IN THE FOCAL AREA FOR CORNEA SAMPLE AND COLLAGEN SOLUTION.	109
Fig. 6. 3: COMPARATIVE POST EXCITATION TEMPORAL EVOLUTION OF THE NORMALIZED ABSORPTION SIGNAL IN THE FOCAL AREA FOR CORNEA SAMPLE AND COLLAGEN SOLUTION. THE ABSORPTION VALUES ARE NORMALIZED AT THE SECONDARY PEAK.....	110
Fig. 6. 4: SPATIAL DISTRIBUTION OF THE REFRACTIVE INDEX (REAL PART) AFTER EXCITATION OF COLLAGEN (TYPE 1 0.38% W) SOLUTION. PUMP PULSE : $0.3 \mu\text{J}$ (35 FS, 800 NM), DELAY ~ 0 PS	111
Fig. 6. 5: COMPARATIVE TEMPORAL DYNAMICS AFTER IR FS EXCITATION IN WATER, CORNEA AND COLLAGEN SOLUTION. (A) LINEAR SCALES (B) LOG-LOG SCALES.	112
Fig. 6. 6: DELAY OF THE APPEARANCE OF THE PEAK RELATED TO SOLVATED ELECTRONS FOR THE EXPERIMENTAL CONDITIONS OF REF. [DFA12] (FOR AXICON CASE THE $400 \mu\text{J}$ INPUT ENERGY IS COMPARABLE TO OUR EXPERIMENTAL CONDITIONS)	112
Fig. 6. 7: SIGNAL SCATTERED INTENSITY. SIMILARITIES TO OUR RESULTS: A MINOR (IN THIS EXPERIMENT) PEAK ~ 500 FS, NO OTHER SIGNIFICANT PEAK FROM 1-10 PS [Csc02].	113
Fig. 6. 8: THE ABSORPTION RESULTS ARE VERY SIMILAR TO OUR MEASUREMENTS IN WATER [SMI08].	113

List of Tables

CHAPTER I

TABLE 1.1: DIMENSIONS OF THE ADULT HUMAN EYEBALL [AKK07].	21
TABLE 1.2: REFRACTIVE INDEX OF DIFFERENT CORNEAL LAYERS [SPA95].	29
TABLE 1.3: A COMPARISON BETWEEN HUMAN AND PORCINE EYEBALL (DATA OBTAINED FROM [CFA08] [ISA11] [LJA08] [CME07] [CEW10][YZE01]).	34

CHAPTER II

TABLE 2.1: DIFFERENT PROFILES THAT CAN BE USE TO DESCRIBE ULTRASHORT PULSES AND THEIR CORRESPONDING K VALUES [CRU04].	40
TABLE 2.2: DIFFERENT IONS CAPABLE OF PRODUCING ULTRASHORT PULSES CLOSE TO $1\ \mu\text{M}$. (*DIRECT DIODE-PUMPING OF Ti:SA LASERS WAS REALISED ONLY RECENTLY AND NEEDS CONSIDERABLE FURTHER IMPROVEMENT [PWR11] [CGD12]).	46
TABLE 2.3: CONVERSION OF DIFFERENT jk TO l .	48
TABLE 2.4: PROPERTIES OF LiNbO_3 CRYSTAL [BFJ08].	50

Chapter III

TABLE 1.1: DIMENSIONS OF THE ADULT HUMAN EYEBALL [AKK07].	21
TABLE 1.2: REFRACTIVE INDEX OF DIFFERENT CORNEAL LAYERS [SPA95].	29
TABLE 1.3: A COMPARISON BETWEEN HUMAN AND PORCINE EYEBALL (DATA OBTAINED FROM [CFA08] [ISA11] [LJA08] [CME07] [CEW10][YZE01]).	34
TABLE 3.1: BREAKDOWN TEMPERATURE T_{cr} FOR DIFFERENT PULSE DURATIONS [NOB10].	66

CHAPTER IV

TABLE 4.1: GRATINGS THAT ARE PRESENT ON CRYSTAL A AND B.	75
TABLE 4.2: CONVERSION EFFICIENCIES, THE VALUE OF SIGNAL AND IDLER GENERATED BY EACH GRATING AND TRANSPARENCY OF HIGH PASS FILTER FOR EACH SIGNAL AND IDLER VALUES.	77
TABLE 4.3: CHARACTERISTICS OF THE GENERATED SIGNAL FROM OPG AND OPA.	86

CHAPTER V

TABLE 5.1: ESTIMATED SHOCKWAVE AMPLITUDES FOR THE CASE OF CONSTANT ENERGY ($16.5\ \mu\text{J}$) AND VARIABLE DISTANCE.	104
TABLE 5.2: ESTIMATED SHOCKWAVE AMPLITUDE FOR THE CASE OF VARIABLE ENERGY AND CONSTANT DISTANCE OF $50\ \mu\text{M}$ FROM ENDOTHELIUM CELLS.	105

Introduction

The eye is the sense organ of the body that allows us to see the world around us. Like other organs of the human body, the eye can encounter various diseases and injuries, some of which may be treated by surgery. Surgical techniques have been evolved with time. In today's era, the use of ultrashort laser pulses (time duration less than 10^{-12} sec) is becoming common for the surgery of the anterior segment of the eye [Pla10] [Hks09]. When ultrashort laser pulses are focused into the tissue they create free electrons through non-linear ionisation processes which result in the formation of a strongly localised plasma. The threshold in radiant exposure necessary to create this plasma is of the order of $1-3 \text{ J/cm}^2$ [Nob10][Vog05]. The plasma communicates energy to the tissue, which results in optical breakdown, the creation of a shock wave and the subsequent formation of a bubble. The gas forming the bubble is reabsorbed by the tissue leaving a narrow incision. By placing these incisions next to each other it is possible to induce surgical cuts in three dimensions. The main difference between the use of ultrashort pulses and lasers emitting longer pulses or cw radiation for surgery is the confinement of unwanted thermal effects which in the case of ultrashort laser do not affect the neighbouring tissue [Vog05].

The first ultrashort laser systems for eye surgery were realised in the early years 2000, when they were first used to create corneal flaps as part of the LASIK¹ procedure for refractive surgery. Several systems are now available of which some also offer routines for corneal grafting. In parallel, systems have been developed for cataract surgery; studies have also addressed the use of ultrashort pulse lasers for glaucoma surgery and the treatment of presbyopia.

In recent years, the group *Optique Photonique Santé* at the *Laboratoire d'Optique Appliquée* has worked on several studies concerning the optimisation of the performance of surgical lasers. The group has studied the tissue optics of the cornea in order to minimise light scattering effects compromising the laser beam quality. The group has identified a window of relative optical transparency centred at 1650 nm and has developed appropriate laser sources. The present thesis continues and completes several of these earlier studies.

¹ Laser *In Situ* Keratomileusis

Scientific objectives

Three main subjects have been covered in this thesis.

- In the first project we have developed, optimised and fully characterised a compact laser system based on nonlinear wavelength conversion that is able to produce laser pulses at wavelengths in the short wavelength infra red range. In particular, this system can produce laser pulses at 1650 nm which previously had been identified as the optimum wavelength for corneal surgery; pulses at 1300 nm may be used to optimise the laser performance in the crystalline lens. This system can also be used to study the incision quality for different wavelengths.
- In the second project we have studied the effect of ultrashort pulses on the viability of endothelial cells as a function of pulse energy and the distance of the incisions to the cells. For this project two different sets of experiment were conducted at constant energy and constant depth. In this experiment for high pulse energies ($\sim 17\mu\text{J}$) and short distances to the endothelial cells we have observed cell death. The exact mechanism of cell death still needs to be identified with certainty. We have confronted our results to estimated values of the amplitude of the shock waves which are the likely cause for cell death.
- In the third project we have studied the dynamics of the interaction of femtosecond laser pulses with water, a collagen type I solution and cornea. This study has been performed at and in collaboration with the Institute of Electron Structure & Laser and with the implication of another PhD student of the group. The aim of this study was to explore the plasma creation dynamics of the focal region after the interaction with the ultrashort laser pulse. Particular attention was addressed to the identification of potential differences between the behaviour of water, often used as a “model” medium for tissue, a model collagen solution, and actual corneal tissue. It was found that the interaction dynamics of water are very different from that of cornea whereas the dynamics observed in the collagen solution were very similar to those in cornea. In light of our findings we suggest to use collagen type I solution as a model solution to study the dynamics inside the cornea instead of water.

Thesis plan

The thesis consists of six chapters.

The first chapter gives an introduction to the anatomy of the cornea and its optical properties. The properties and functions of the different layers of cornea are briefly described in this chapter. At the end of the chapter we have described different surgical routines for which ultrashort laser pulses can be used.

In the second chapter we give an introduction to the theory of ultrashort pulses and discuss the main principles of their practical generation. We then give an introduction into non-linear optics and non-linear parametric processes.

In the third chapter we first describe the interaction of ultrashort laser pulses with tissue. The main phenomena discussed are plasma creation, the formation of bubbles and the associated creation of shock waves.

The fourth chapter explains in detail the characteristic of the optical parametric generator and amplifier based on periodically poled lithium niobate crystals which has been developed and characterised in this thesis.

In the fifth chapter we present our study of the effect of ultrashort pulse lasers on the viability of endothelial cells.

In the sixth chapter we present the results of our study of the interaction dynamics of ultrashort laser pulses inside water, collagen and cornea.

At the end of the thesis we provide a conclusion of thesis and outlines possible future developments or studies in the field.

Chapter I

Anatomy and optical properties of the cornea

The main elements of the human eye, from front to back, are: the cornea, the aqueous humour, the iris, the crystalline lens, the vitreous humour and the retina. All these are held together by a white body call sclera. The eye has an ablate spheroid shape. The cornea and the crystalline lens focus the incoming light onto the retina. The cornea contributes about two-thirds to the total optical of the eye, the rest being contributed by the crystalline lens. The retina contains light sensitive rods and cones which transform incoming photons into nerve signals which are sent to the brain through the optical nerve.

The anatomy of cornea and its optical properties of the cornea such as refractive index, birefringence, transmission, and scattering are presented in detail in this chapter. We also discuss the anatomical differences of between human porcine eyes, the latter having been used as a model for the former during the present thesis. We then present different surgical routines of the anterior segment of the eye.

1.1 The human eye

The human eye is a complex sense organ which allows us to see the world around us. Its development starts at around the 22nd day of gestation from the neural cells that extend from the brain. The eye takes almost nine months to fully develop; complete visual acuity is achieved at 4-6 months of age [Akk07]. The eye is covered by an eyelid and a tear film. The eyelid is a thin and foldable skin presenting eyelashes. The function of the eyelid is to protect the eye from the environment whereas the lacrimal gland produces and renews the tear film; the tear duct evacuates excess amount of tear. In some conditions such as “dry eye” the tear duct needs to be closed in order to maintain humidification. Behind the eyelid the eye has an ablate spheroid shape. The typical dimensions of the eyeball are as follows [Akk07].

Anteroposterior diameter	24 mm
Horizontal diameter	23.5 mm
Vertical diameter	23 mm
Circumference	75 mm
Volume	6.5 ml
Weight	7 g

Table 1.1: *Dimensions of the adult human eyeball [Akk07].*

Each eye takes one-fifth of a second to look from extreme left to right. The eye is moved by extraocular muscles. Figure 1.1 shows two of these muscles. The eyeball consists of three different coats which are fibrous, vascular and nervous. The fibrous coat protects the eye from the environment. 1/6 of the fibrous coat corresponds to the transparent cornea whereas the remaining opaque part is called sclera, which is the white part of the eye. The expression ‘sclera’ has a Greek root meaning ‘hard’ [Rba06]. The sclera is thicker at the back of the eye with an average thickness of around 1 to 1.35 mm; its thickness gradually diminishes towards the front until it becomes 0.4 to 0.6 mm at the equator [Djj06]. The cornea (root word meaning ‘like an animal horn’) is the transparent anterior part of the fibrous coat, it is connected to the sclera through the limbus. The healthy cornea has an average thickness of 550 μm and is curved slightly outward. The transparency of the cornea is very important for vision as light passes through this tissue. The cornea is one of the tissues which were studied extensively in this work; it will be described in more detail in the following [Rba06].

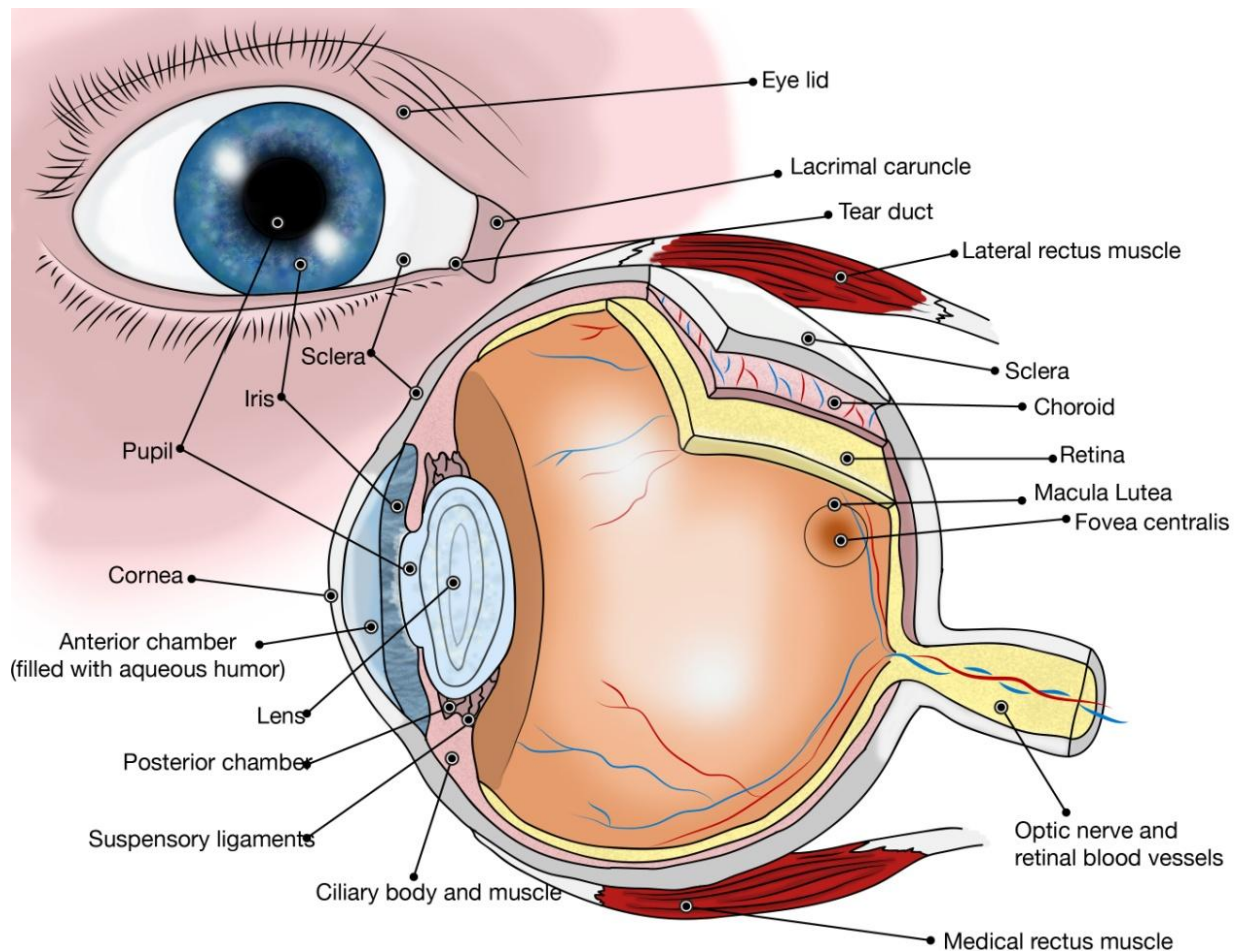


Fig. 1. 1: *Cross sectional and en face view of the human eye [Mus].*

The vascular coat provides nutrition to the eyeball. It consists of three parts which are iris, ciliary body and choroid. The choroid is a spongy and pigmented structure with a thickness of around 0.2 mm. It consists of blood vessels, the primary function of which is to provide nourishment to the photoreceptors that convert light into neural signals. Due to its high pigmentation, the choroid also absorbs the light that is not absorbed by the retina, thus reducing backscattering and subsequent multiple reflections of the light. From the posterior to the anterior side the choroid starts to curl and becomes parallel to the cornea. This structure is called ciliary body. The ciliary body produces aqueous humour – which is the main source of nutrients and oxygen to the cornea and lens – and evacuates excess liquid. The production of aqueous humour and its drainage needs to be balanced. In case of overproduction or reduced drainage, the pressure starts to build inside the aqueous humour. In case of extreme pressure this can affect vision by compromising the function of the retina, a condition commonly known as glaucoma. This ciliary body is connected to the iris (from the Greek word for ‘rain-

bow'). The iris is located behind the cornea and can have different colours such as brown, gray, blue (in fig.1.1) and so forth. The black region at the centre of the iris is called pupil. The iris is attached to the dilator muscle that controls the diameter of the pupil and controls the amount of light which reaches the posterior parts of the eye that can be detected by the photoreceptors. Located behind the iris, the crystalline lens is one of the two focusing optical elements of the eye. The crystalline lens is a biconvex transparent lens enclosed within the lens capsule, which itself is attached to the ciliary muscle by the ciliary zonules. The capsule is transparent and permeable and provides nutriment to the lens through the aqueous humour. The ciliary muscle controls the shape of the crystalline lens and works against its elasticity. Changing the shape of the crystalline lens by constraining or relaxing the ciliary muscle permits to modulate the optical power of the lens and thus allows us to focus the image of near and far objects onto the retina. This process is called accommodation (see Appendix 1 for a detailed discussion of the lens and its transparency). The vitreous humour constitutes about two-thirds of the total volume of the eye. This chamber is filled with a gel like substance called vitreous. The vitreous is enclosed within a thin membrane that is anchored in the wall of the eyeball. Unlike the aqueous humour, the vitreous humour is not regularly renewed and may consequently lightly degenerate over time by the deposition of tissular debris. This debris can affect the light propagation through the vitreous and may cause artefacts resulting in small black spots in the visual field. Due to gravity these debris usually settle in the lower part of the eyeball. Big pieces of debris which hamper vision more strongly may be broken up into small pieces with the help of a laser. At the posterior extremity of the eyeball, the retina constitutes the final layer of the visual system. It contains three different layers that include layers for neurons, rods, and cones. The retina converts the light waves into neural signals that send the signal to the brain through the optic nerve. In case of damage to the optic nerve the eye is no longer capable to form images. [Rba06]

In the following sections we will present the structure of the cornea and its optical properties in detail.

1.2 The anatomy of the cornea

The cornea is the first transparent layer of the eye and contributes about two thirds (2/3) to total optical power of the eye. Its formation starts around 9 weeks of gestation by mesenchyme (a fibrous layer) and ectoderm cells [Akk07]. It is connected to the sclera through the limbus and protects the eye against the environment. Human cornea consists of six layers,

namely the epithelium, Bowman's layer, the stroma, Dua's layer, Descemet's membrane and the endothelium (Fig. 1.2A). It typically has a diameter of around 11.5 mm in the horizontal direction and 10.5 mm in the vertical direction (Fig. 1.2B) [Cew10]. For a clear healthy cornea the thickness varies from 550 μ m at the centre and 700 μ m at the periphery.

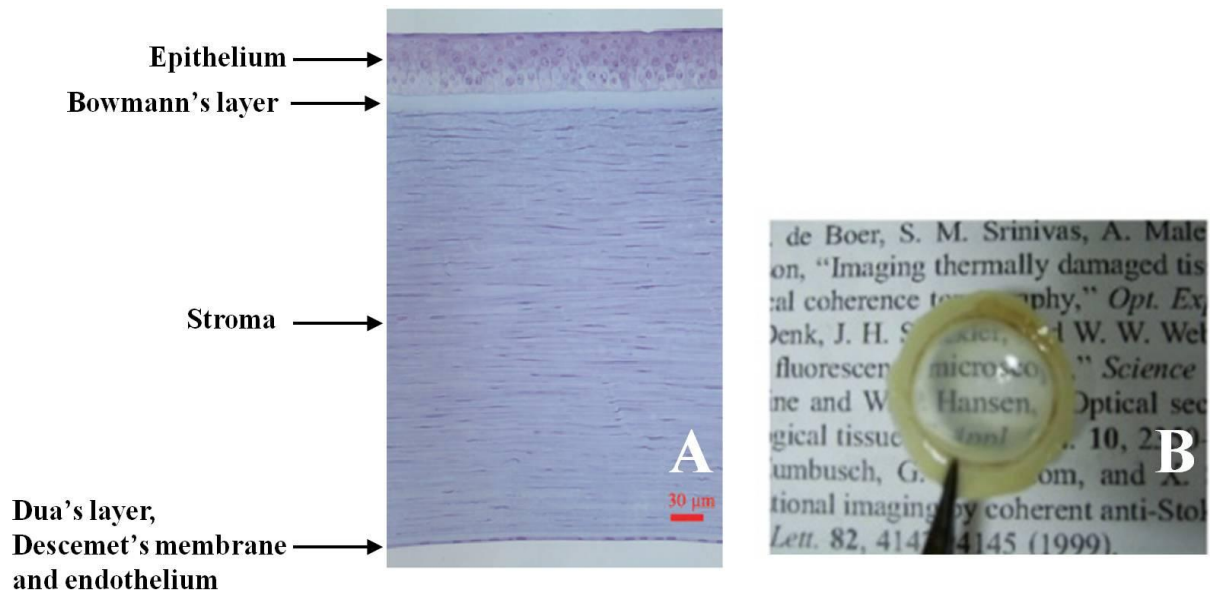


Fig. 1. 2: (A) *Histology of human cornea (scale bar = 30 μ m)* (B) *human cornea.* (Michèle Savoldelli, Hôpital Hôtel Dieu de Paris) [Pla10].

1.2.1 Epithelium

The epithelium consists of five to six cell layers and has a thickness of about 50 μ m. The primary function of this layer is to protect the eye from the exterior environment and to provide nutrition through the tear film which is then transported to the rest of the cornea by passive diffusion. The epithelium has the ability to regenerate itself by the proliferation of the epithelial cells. Since this layer is in direct contact to the atmosphere, any irregularity or damage will result in reduced visual acuity [Wsv06].

1.2.2 Bowman's layer

The following layer is Bowman's layer which is connected to the epithelium at the basement membrane. In the adult eye, Bowman's layer has a typical thickness of 8 to 12 μ m [MjH71] and consists of collagen fibrils (type I and III). Bowman's layer is present in pri-

mates, humans and other animals like birds, however in some animals like pigs it is absent. At the posterior side, Bowman's layer forms a contiguous with the stroma; consequently, Bowman's layer cannot be stripped easily from the stroma like Descemet's membrane [Mks06] [Lja08] (see below).

1.2.3 Stroma

The corneal stroma is the thickest layer of the cornea with an average central thickness of about 450 μm [Mks06]. The corneal stroma contains small numbers of cells known as keratocytes which are scattered inside the volume of the stroma. They are formed during the development of the cornea and remain in it as a modified fibrocytes (Fig. 1.3) [Dgd06]. The rest of the stromal volume is composed of extracellular matrix (ECM) [Vog03].

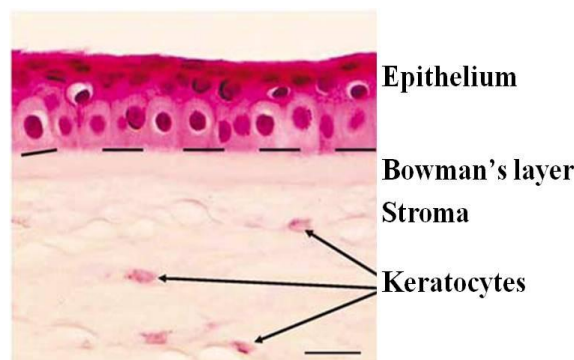


Fig. 1. 3: Presence of keratocyte inside thr stroma scale bar 10 μm (Modified from [Ssa06]).

The extracellular matrix (ECM) is mostly composed of water, collagen, elastin, glycosaminoglycans, glycoproteins, and proteins. For the case of corneal stroma it is composed of water (78%), while the dry weight of human corneal stroma was found to consist of collagen (68%), keratocytes (10%), proteoglycans (9%), and salts, glycoproteins, or other substances [Dmm84]. Collagen, which is the largest by weight, is a hydrophilic protein and composed of three alpha chains. Theses alpha chains are held together in a right handed triple helical structure and form the basic entity of the tropocollagen (TC) molecule shown in Fig 1.4A.

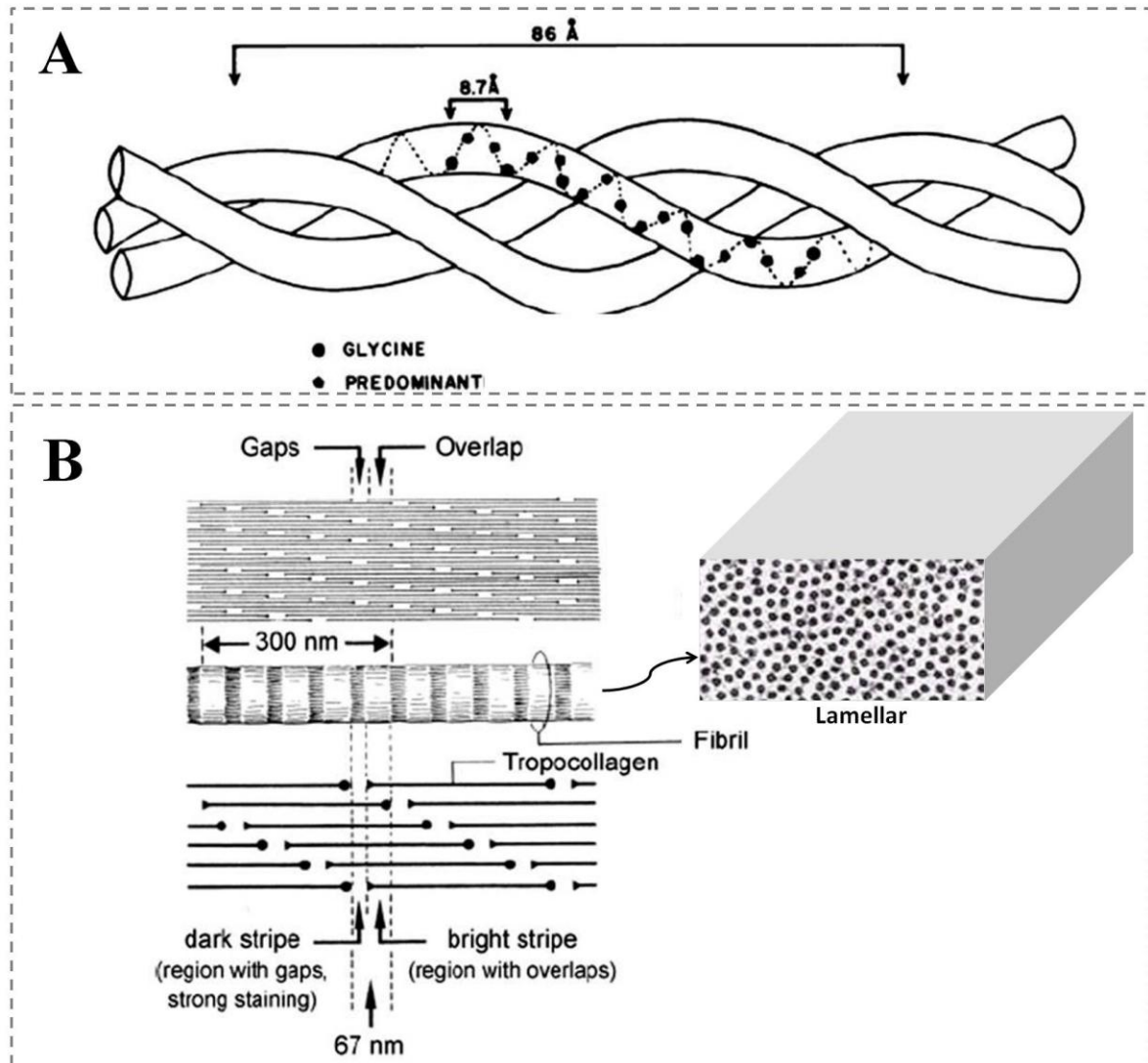


Fig. 1. 4: Representation of the tropocollagen (TC) molecule (A), Different architectural levels of the collagen structure of the sclera (B) (Modified from [Vog03]).

Six TC molecules are linked by covalent cross-links around a common centre to form a microfibril. Within the fibril, these molecules are staggered approximately by one quarter of their length, which give rise to a periodical structure with regions of overlap and regions of gaps. These fibrils are immersed in a background substance which mainly consists of proteins and glycoproteins. In the next level of the stromal architecture, these collagen fibrils then form lamellar sheets having a usual thickness of 1-2 μ m (Fig. 1.4B) [Vog03]. They run uninterrupted in nasal-temporal and inferior-superior directions, making different angles with adjacent lamellae whose values lie between 0 and 90° (Fig.1.5) [Cbo05].

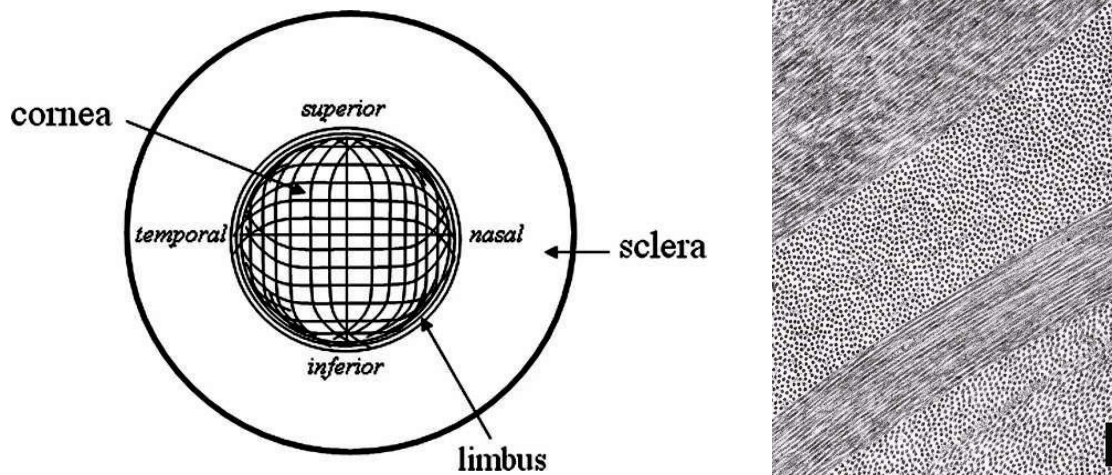


Fig. 1. 5: *Lamellar orientation inside corneal stroma (A) [Cbo05], Cross section of cornea which represent orientation of corneal lamellar (B) (Scale Bar 1 μ m) [Car].*

1.2.4 Dua's layer

Dua's layer is a layer which has been discovered only recently by Harminder Dua, in 2013. Its thickness is about 15 μ m; it contains type VI collagen [Hsd13] [Hsd14]. Its function is currently under investigation.

1.2.5 Descemet's membrane

Descemet's membrane is the second last layer of the system sandwiched between Dua's layer and the endothelium. It consist of several layers whose combined thickness in adults is usually 8 to 10 μ m; it is mostly composed of collagen of type (VI, VIII). It can be stripped off from the stroma relatively easily during a surgical routine [Mks06].

1.2.6 Endothelium

The posterior layer of the cornea is formed by a monolayer of cells with a relatively regular polygonal mosaic structure. The cells have an average diameter of about 20 μ m, a thickness of about 5 μ m and each covers an area of about 250 μ m² [Mjh71] [Hfe00]. Depending upon the age [Rwy85] and location on the endothelium, the density of these cells can vary [Dgd06], however, in the centre of a typical healthy adult human cornea their density is about ~ 2500-3500 cells/mm² [Pip11] and about 10% more in the peripheral regions [Jam03]. Their

intercellular space contains apical tight junctions and lateral gap junctions. These junctions permit the diffusion and active pumping of small molecules through them (Fig.1.6) [Dgd06].

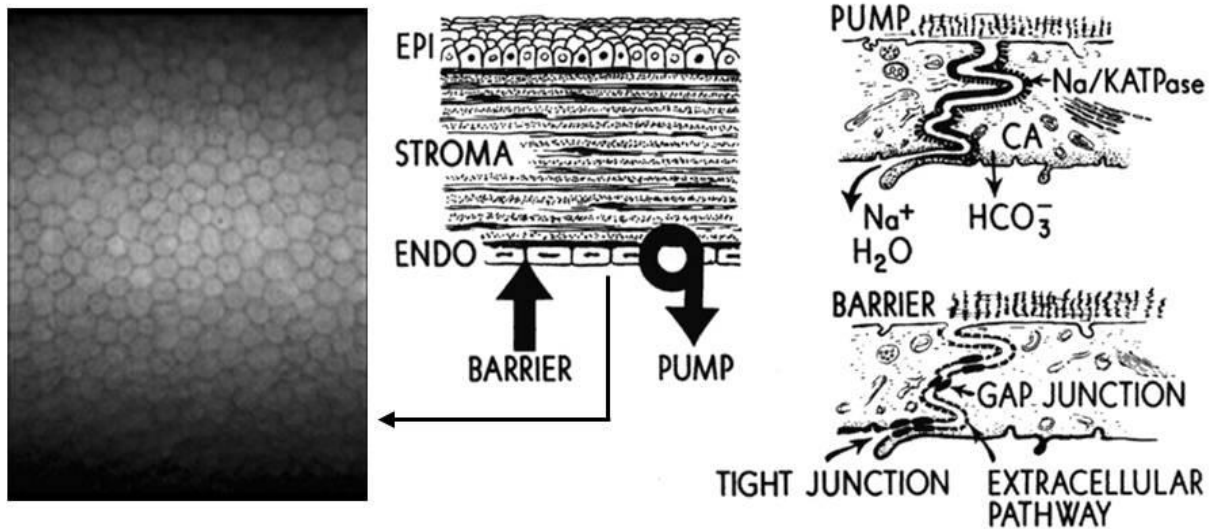


Fig. 1. 6: Endothelial cells and their pump and leak mechanism [Nid] [Gow82].

By means of these transport processes, the endothelial cells keep the hydration of the cornea at a constant level (78%) [NcJ03][Dmm72]. Endothelial cells do not proliferate in humans. However, in case of the death of individual cells, neighbouring cells expand and cover the void area. In case of endothelial dysfunction and the loss of the liquid transport properties of the endothelium [Aly04], the corneal hydration increases and the cornea develops an oedema. The average distance between the collagen fibrils in the stroma then becomes higher than normal and the corneal stroma loses its regular nanostructure. Corneal oedema is associated with a loss of transparency (see below).

1.3 Optical properties of cornea

1.3.1. Refractive index

As has been described above, most of the corneal volume is occupied by the stroma which mainly contains background substance and collagen fibrils. The refractive index of cornea (n_c) may be calculated as

$$n_c = n_{cf} \cdot f_{cf} + n_{gs} \cdot f_{gs} \quad , \quad (\text{Eq. 1. 1})$$

where n_{cf} is the refractive index of the fibrils and n_{gs} is the refractive index of the background substance. f_{cf} and f_{gs} are the volume fraction of both components ($f_{cf} + f_{gs} = 1$)

[Ylk04]. As the refractive index depends upon the volume of ground substance and its refractive index, change in hydration will result in a change in the refractive index of the cornea. (The associated structural changes making it also less transparent will be discussed below). The refractive index can be measured with the help of a refractometer. The local refractive indices of different layers and their corresponding values are given in the following table.

Layer	Refractive index
Epithelium	1.401
stromal anterior	1.380
posterior surface	1.373

Table 1. 2: *Refractive index of different corneal layers [Spa95].*

1.3.2. Birefringence

The corneal birefringence has been known since the early 19th century and has been studied extensively since [Dbr15] [Ljb91] [Ckh06]. This property is closely linked to the stromal architecture which is organised in lamellae of collagen fibrils (see above). Each lamella acts as a birefringent layer with its slow axis along the collagen fibril direction [Mgd99]. As already described, lamellas run along from nasal-temporal and inferior-superior directions. Therefore, to a first approximation the overall contribution of orthogonal lamellas will cancel the contribution of each other [Rhn98]. X- ray studies show that 60% percent of lamellas are orientated within 45° sectors of inferior-superior and nasal-temporal preferred directions whereas 40% are oriented in oblique sectors that will result in a net birefringence [Ada97] [Rhn98] [Ckh06]. As the birefringence is associated with the orientation of collagen inside stroma, birefringence measurements used to detect perturbations in the volume of the stroma. For example, by using polarisation-sensitive optical coherence tomography (PS-OCT) it is possible to detect keratoconus [Egö07].

1.3.3. Transmission and scattering

On the nanometric level, the corneal stroma is composed of collagen fibrils with a refractive index higher than the surrounding medium [Pla10]. In 1957 David Maurice calculated the scattering cross section of an individual fibril. He concluded that the total scattering cross section of the cornea would result in an opaque tissue, when summing up the contributions of all collagen fibrils while assuming that their distribution is random. He concluded that the distribution of the collagen fibrils must exhibit a certain regularity or even,

as Maurice postulated, a crystal-like periodicity. In this case, interference is destructive in all directions except the forward direction, which explains corneal transparency. The absence of transparency in a pathological cornea may then be explained by the loss in structural regularity (Fig 1.7).

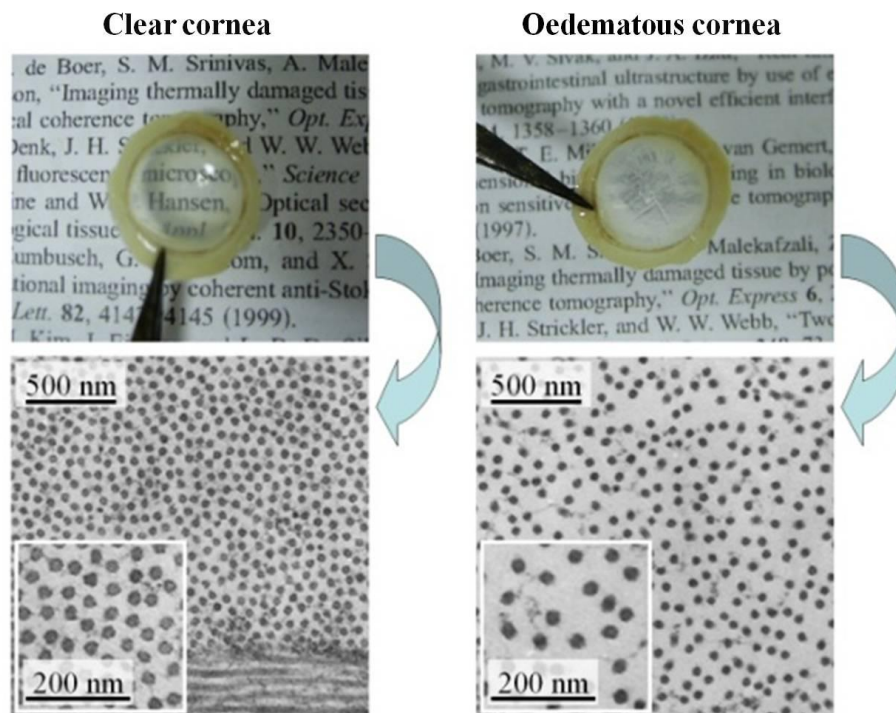


Fig. 1. 7: *Difference between clear and oedematous cornea [Pla10].*

This argument was later challenged by various researchers because the electron micrographs did not reveal a crystalline structure similar to the one postulated by Maurice. However, subsequent work showed that crystalline periodicity is not necessary to assure transparency; it is possible to prove that corneal transparency may be explained by a local short range order [Gbb71] [Rwh69]. Goldman and Benedek present the example of a shark Bowman's membrane which shows a somewhat disordered fibril structure but yet is transparent. They further proposed that in addition to local order between the fibrils the distance between the fibrils should not exceed the wavelength of light [Jng67].

The above arguments concern scattering processes which occur at nanometric length scales. The keratocytes inside the stroma are of micrometric dimensions and give rise to a distinct scattering process, which has to be considered separately (Fig.1.3). When the cornea becomes highly oedematous an additional term due to formation of the so-called "lakes" contributes to the scattering by micrometric structures. Lakes are regions devoid of collagen fi-

brils which form preferentially at the intersections of collagen lamellae; they have micrometric thicknesses and lateral dimensions which may reach several 10 micrometres (Fig.1.8). It has been shown recently that previous history of corneal wounds is also associated with light scattering. Corneal wounds may have an impact for up to four years after the corneal accident [Rlm07].

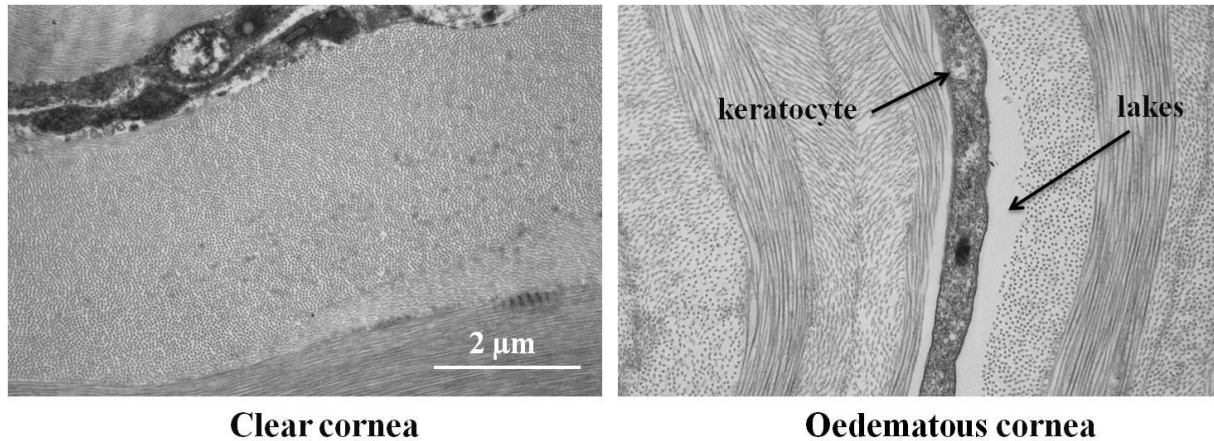


Fig. 1. 8: A comparison of clear and oedematous cornea. Keratocytes and lakes are visible in the oedematous cornea (Michèle Savoldelli, Hôpital-Hôtel Dieu de Paris).

Experimentally, the transmission and scattering inside the cornea can be studied in different ways [Nta07] [Jwa04] [Svp07] [Ddb08]. An example of a measuring approach is described below and will be discussed extensively in the later chapters. An initial study based on this approach was performed by Boettner and Wolter [Eab62]. They studied the corneal transmission by comparing data obtained from two different setups providing transmission spectra corresponding to “direct” and “total” transmission. Recently, D. Peyrot *et al.* from our own group used a refined approach based on the former work of Boettner and Wolter to measure the transmission and scattering properties of cornea presenting different degrees of oedema [Dap10]. The two experimental setups used in the study are shown in figure 1.9.

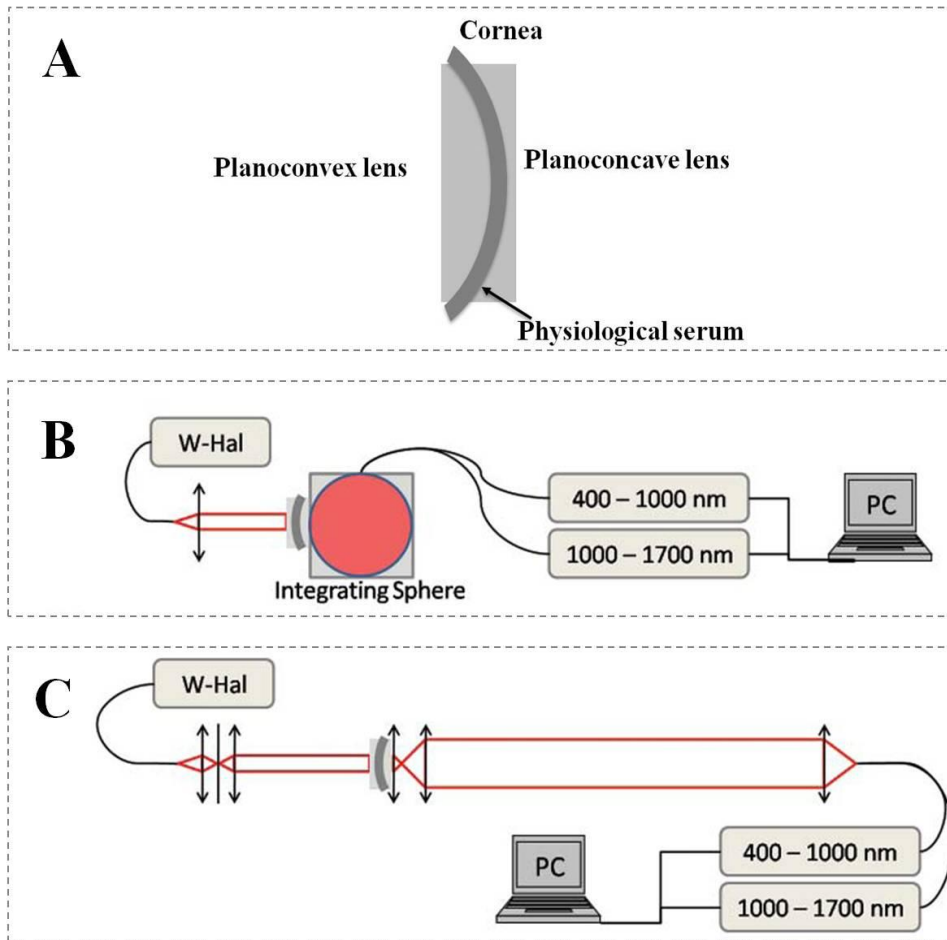


Fig. 1. 9: *Experimental set-up to measure the (A) Cornea sandwiched between two lens pairs, (B) total transmission (TT), (C) direct transmission (TD) of tissular samples. (W-Hal=Halogen light source) [Dap10].*

For these experiments they sandwiched the cornea (from which the epithelium was stripped) between a pair of lenses whose radii were adapted to the natural curvature of the corneal surfaces. One planoconvex and one planoconcave lens were thus used in order to minimise surface scattering. A small amount of physiological serum was inserted between the cornea and the lens surfaces in order to match the refractive indices (Fig.1.9A). Residual reflections from both surfaces amounted to only 4%, which may be attributed to Fresnel reflection from the lens surfaces. The first experimental set-up is sensitive to the total transmission (T_T) in which the spectrometer measure the transmission of the cornea from 400-1700nm (Fig.1.9B) integrated over all angles in the forward scattering direction. The second set-up measures the spectra of the cornea in “direct” transmission (T_D), that is, it is only sensitive to photons which have experienced a negligible amount of scattering and which remain in a solid angle of 10^{-7} sr around the optical axis. The fraction (Ξ) of the photons that have experi-

enced light scattering with trajectories outside of this solid angle can be calculated by subtracting direct transmission (T_D) from total transmission (T_T) (Fig.1.9). A typical result obtained on a transparent cornea is presented in figure 1.10. The result shows that the percentage of scattered photons is high for short wavelengths, continuously decreases toward the red spectral range and becomes minimal in the near infrared (no meaningful measures are possible in the wavelength range around 1400 nm because of the strong light absorption due to the water absorption band which affects this wavelength range). In conclusion, the use of near infrared wavelengths will minimize the scattering effects inside the cornea and will give superior results if used for medical applications.

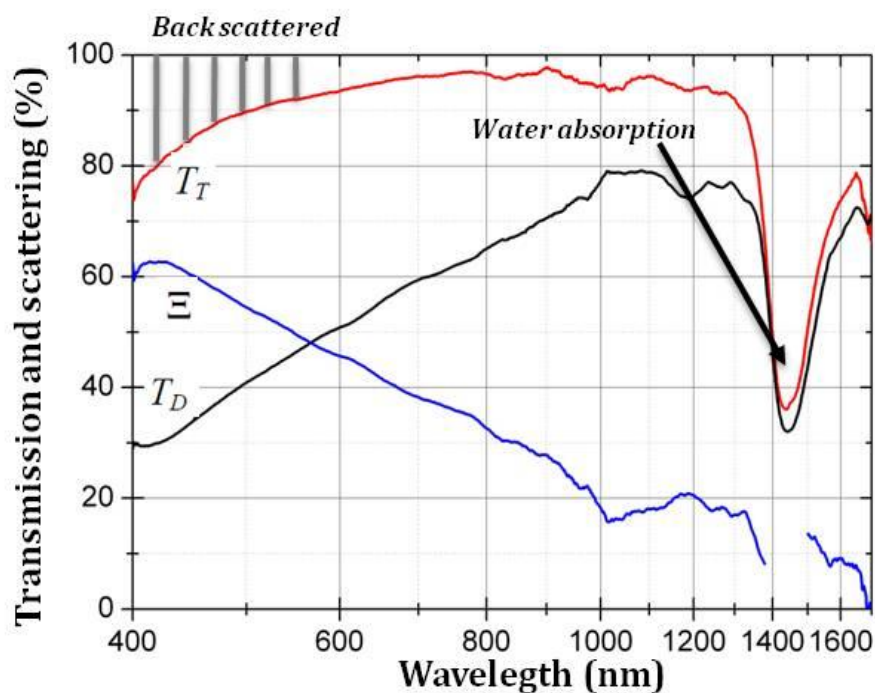


Fig. 1. 10: Total, direct and scattering of a 450 μm thick cornea.

By repeating the same process for corneas presenting different thicknesses it is possible to estimate the amount of scattered light at different wavelengths for different degrees of oedema (Fig.1.11). Different degrees of oedema were produced by using a saline solution to increase the thickness of cornea (increased oedema) or by using a deturgescence process to decrease the thickness of cornea. The results that have been obtained are shown in figure 1.11. At any single wavelength, the amount of scattering is high for thick, highly oedematous corneas; it decreases with thickness and presents a minimum at the natural thickness of the cornea. By further decreasing the thickness, light scattering increases again. Electron micro-

graphs of corneas in such a state suggest that at this point, the repulsive potential between some collagen fibrils breaks down resulting in local clusters, which result in an increased overall scattering cross section (Fig.1.11).

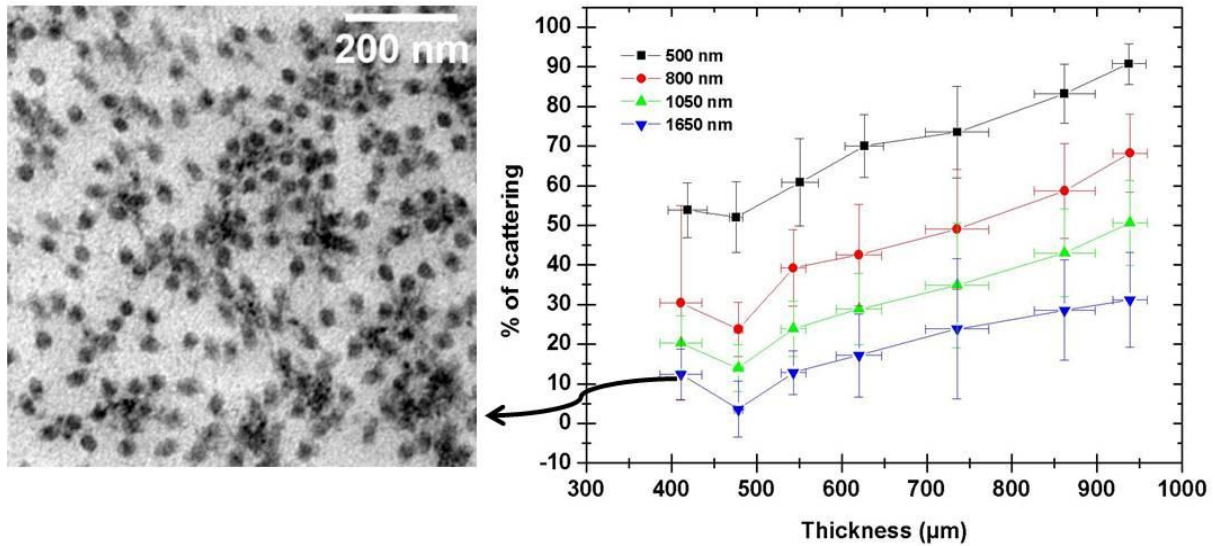


Fig. 1. 11: Percent of scattering for different wavelengths at different thicknesses [Dap10].

1.4 Anatomical differences between human and porcine corneas

For the experiments performed for this thesis we have mostly used porcine cornea. Porcine corneas are not as difficult to obtain as human corneas which makes them a suitable model tissue for experimental work. However, special attention should be given in order to use them as model because one property in porcine cornea can be very different from human cornea. A comparison of porcine cornea with human cornea is presented as follows.

	Human cornea	Porcine cornea
Corneal thickness (mm)	550	800 to 1000
Bowman's layer (Present/Absent)	Present	Absent
Endothelial cell density (cells/mm ²)	~3000	~4300
Horizontal diameter (mm)	11.5	14.9
Vertical diameter (mm)	10.5	12.4
Tensile strength (MPa)	3.8	3.7

Table 1. 3: A comparison between human and porcine eyeball (Data obtained from [Cfa08] [Isa11] [Lja08] [Cme07] [Cew10][Yze01]).

1.5 Surgical routines for the anterior segment of the eye assisted by ultrashort laser pulses

The development of compact diode-pumped ultrashort pulse lasers in the 1990 [Cho97] made it conceivable to use these lasers in industrial and clinical applications. The mechanism of the incision made by femtosecond laser will be discussed in detail in the following two chapters. In short they create a small bubble inside the volume of the tissue; and placing these bubbles next to each other with slight overlap permits to induce incisions in three dimensions in the volume of the tissue (Fig. 1.12).

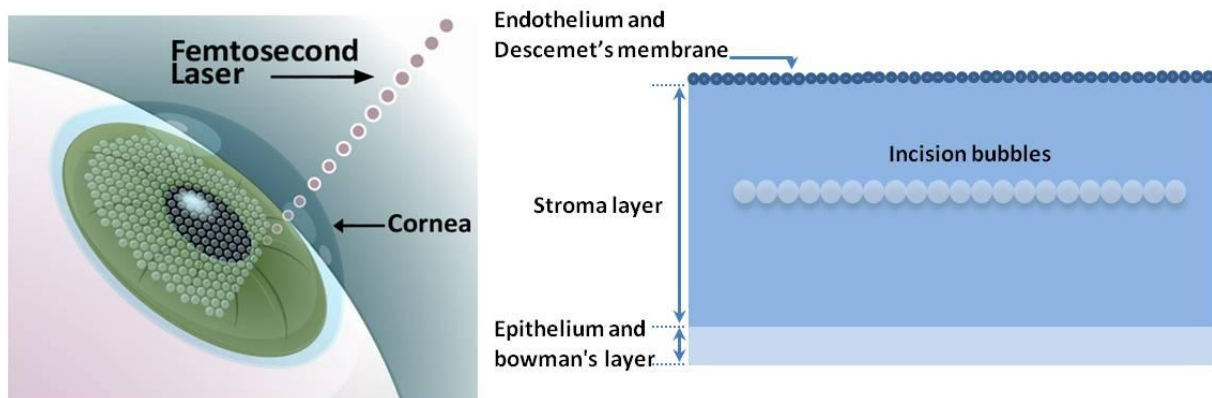


Fig. 1. 12: *Femtosecond laser producing incision inside cornea [Sto].*

Femtosecond lasers for ophthalmology were first commercially introduced in the early years 2000 by the company IntraLase® (now owned by Abbott Medical Optics®). Initially, ultrashort laser systems were used to produce flaps for the laser-assisted in situ keratomileusis (LASIK) procedure, where they replace the microkeratome (manual blade) previously used to produce the corneal flap. Nowadays, they are routinely use for the surgery of the anterior segment of the eye. Different surgical routines that can be performed by femtosecond laser systems are summarized in the following tree diagram (Fig. 1.13). Different laser systems are now available commercially whose specification can be found in literature [Pla10], in text that followed we will briefly describe routines stated in the tree diagram.

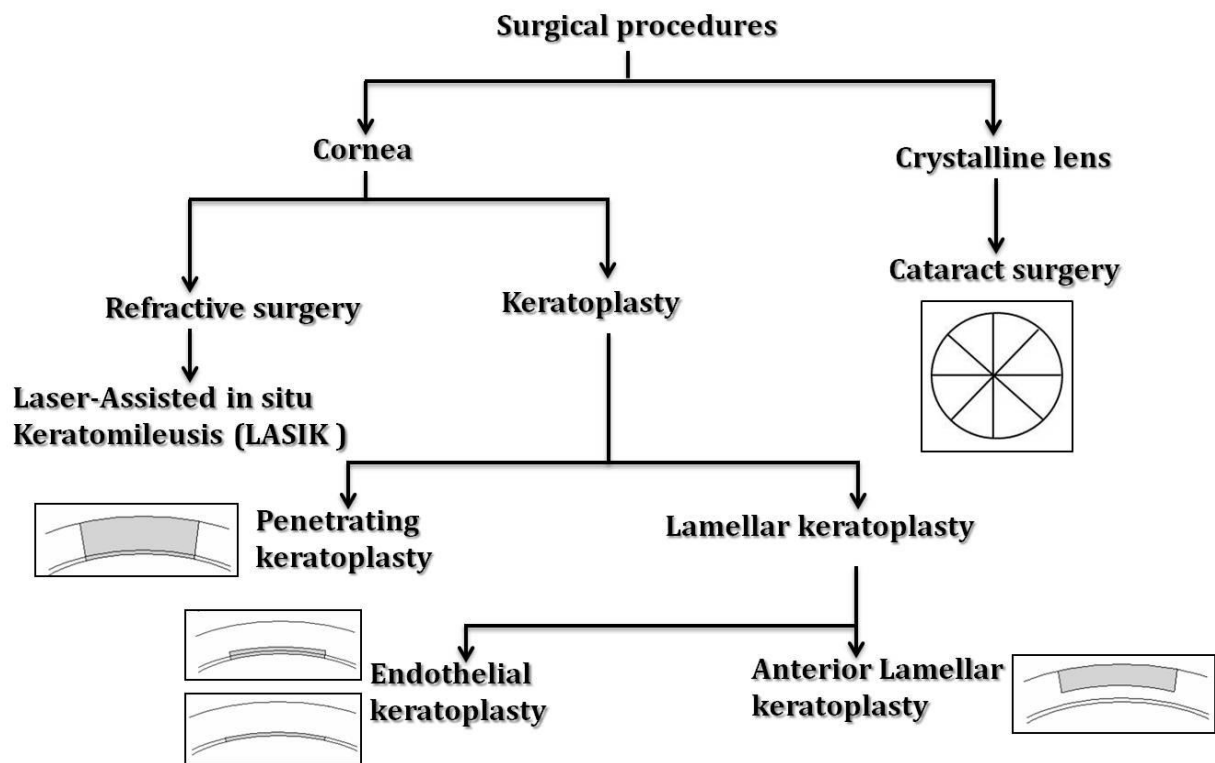


Fig. 1. 13: Different surgical procedures for which femtosecond lasers can be use [Pla10].

For LASIK the femtosecond systems are mainly use for creating flaps for the patient undergoing refractive correction. The flap is then lifted and stromal tissue is removed. These femtosecond systems can also be used for keratoplasty (corneal grafting), which may address the entire thickness of the pathological cornea (penetrating keratoplasty) or its anterior or posterior part (lamellar keratoplasty). Keratoplasty replacing only the endothelium and possibly a relatively thin adjacent layer is called endothelial keroplasty. Femtosecond systems can also be used for cataract surgery. In cataract surgery, femtosecond lasers are mainly use for capsulotomy (creating an incision in the lens capsule) and for fragmenting the crystalline lens. Different systems that can provide femtosecond pulses for LASIK, keratoplasty or cataract surgery are shown in Fig. 1.14. Other application of femtosecond for ophthalmology especially for glaucoma is still under investigation [Pla10].

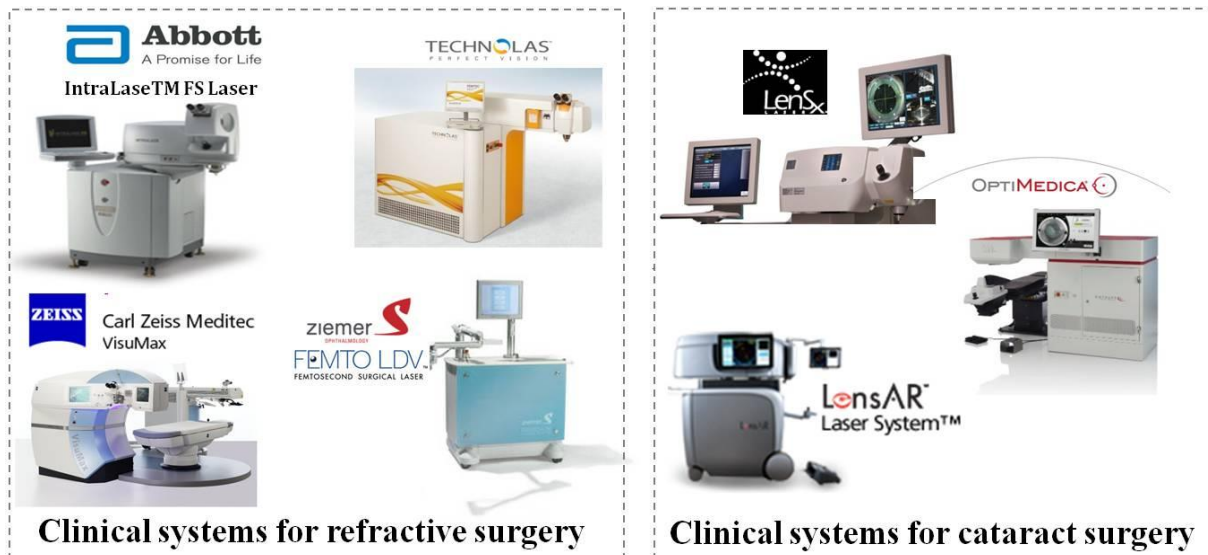


Fig. 1. 14: Femtosecond systems that can be used for the anterior segment of the eye.

1.6 Conclusion

- In this chapter we have presented the anatomy of the eye and described in detail the structure of the cornea and its optical properties such as refractive index, birefringence, transmission, and scattering.
- The cornea is made up of six different layers which are epithelium, Bowman’s layer, the stroma, Dua’s layer, Descemet’s membrane and the endothelium. The local short range order of the collagen fibrils inside the corneal stroma is important for corneal transparency, the value of which should be smaller than the wavelength of light. The fluid in between the micro fibril is regulated by endothelial cells.
- The refractive index of different layers of cornea is approximately equal to 1.37.
- The cornea is transparent in the entire visible spectral range and less transparent in the near infrared. The scattering decrease in near infra red regime with its minimum at 1650 nm.
- During the present thesis, porcine cornea has been used as a model for certain properties of human cornea, however it has to be taken into account that differences exist concerning certain structural and biomechanical properties.
- There are different surgical routines for the anterior segment of the eye for which femtosecond laser can be used. The laser-tissue interaction mechanism will be described in detail in the following chapters.

Chapter II

Ultrashort pulse lasers and optical parametric conversion

Ultrashort laser pulses are high peak intensity pulses with durations below a picosecond ($<10^{-12}$ sec). These pulses can be used for material processing, applications in research and for surgery. In contrast to laser pulses with longer pulse durations whose interaction with matter mostly involves phase transitions, ultrafast laser pulses interact via non-linear ionisation processes which limits permanent modifications to the focal region. Ultrashort pulses can be created in a laser cavity by using an active medium with a broad gain spectrum, locking the phases of different longitudinal modes inside the cavity and managing the dispersion within the cavity. Typical oscillators emit nanojoule pulses. For application requiring more energetic pulses, pulses may be amplified using Chirped Pulse Amplification (CPA) which was originally proposed by Strickland and Mourou.

If the wavelength of the laser pulses needs to be modified, non-linear optical effects in appropriate crystals may be used. The two main approaches for nonlinear wavelength conversion are optical parametric generation and amplification. These processes are capable of creating photon pairs whose combined energy is equivalent to the pump photon. These newly create photons or laser pulses can be used for applications such as spectroscopy and surgery.

In the present chapter we present the principles and mechanisms used for the generation and amplification of ultrashort pulses. We also present different approaches for nonlinear wavelength conversion based on parametric processes and present the principles of optical parametric generation and amplification in detail.

2.1 Ultrashort laser pulses: theory

By their common definition, ultrashort laser pulses are high intensity pulses with durations below a picosecond ($<10^{-12}$ sec). The short pulse duration corresponds to a broad spectrum in the frequency domain. This point can be illustrated by expressing the pulse as a Gaussian pulse. The Fourier transform of a Gaussian pulse is again a Gaussian function, the width of which is inversely proportional to the pulse duration. The Fourier transform relation between time and frequency domains can be written according to equation 2.1(i - ii) [Cru04].

$$\begin{cases} E(t) = \frac{1}{2\pi} \int_{-\infty}^{\infty} E(\omega) e^{-i\omega t} d\omega , & (i) \\ E(\omega) = \int_{-\infty}^{\infty} E(t) e^{i\omega t} dt , & (ii) \end{cases} \quad (\text{Eq. 2.1})$$

where $E(t)$ and $E(\omega)$ represent the evolution of the electric field with time and frequency.

$$\begin{cases} \Delta t = \sqrt{\frac{\int_{-\infty}^{\infty} t^2 |E(t)|^2 dt}{\int_{-\infty}^{\infty} |E(t)|^2 dt}} , & (i) \\ \Delta \omega = \sqrt{\frac{\int_{-\infty}^{\infty} \omega^2 |E(\omega)|^2 d\omega}{\int_{-\infty}^{\infty} |E(\omega)|^2 d\omega}} , & (ii) \end{cases} \quad (\text{Eq. 2.2})$$

If the duration and spectral width are calculating according to the statistical relation 2.2 (i - ii), the duration and spectral width will be related to each other according to equation 2.3 [Cru04].

$$\Delta t \Delta \omega \geq \frac{1}{2} , \quad (\text{Eq. 2.3})$$

This equation is similar to quantum mechanical time energy relation and physically it means that in order to create a laser pulse with a pulse duration of Δt (say at Full Width at Half Maximum) the spectral bandwidth needs to be sufficiently broad to satisfy the above equation. In case of equality the pulse is called as Fourier-transform-limited pulse. Usually, quantities at Full Width at Half Maximum (FWHM) are defined as the measuring parameters, the relation between the time and frequency bandwidth can be written as:

$$\Delta\nu \Delta t \geq K, \quad (\text{Eq. 2.4})$$

where $\Delta\nu$ is the frequency band width ($\omega = 2\pi\nu$) and Δt is the time duration of the pulse and K is a constant parameter the value of which depends upon the pulse shape. Different values of K are summarized in table 2.1.

Function	K
Gaussian	0.441
Hyperbolic secant	0.315
Lorentz	0.142

Table 2. 1: *Different profiles that can be use to describe ultrashort pulses and their corresponding K values [Cru04].*

2.2 Mode locking

The mechanism and techniques used to generate ultrashort laser pulses are described for instance in [Cru04] [Mcs04] [Ukr03] [Pla10]. The part of the laser system that creates ultrashort laser pulses is called oscillator. All systems share the following three elements: an active gain material where stimulated emission can be generated, a pump source and a set of mirrors to provide optical feedback (usually known as cavity mirrors). Typically, the oscillator also contains refractive or diffractive elements to compensate for dispersion. Dispersion arises because of group velocity dispersion (GVD) that accumulates during the beam propagation through different optical materials. GVD refers to the fact that the refractive index of a material is frequency dependent, lead to a broadening of the pulses. Refractive or diffractive elements can be introduced in the oscillator to compensate for this dispersion. Gratings can provide greater dispersion in comparison to prisms but also typically induce greater losses which limit their use to powerful lasers. A combined grating and prism is called “grism” and may be used to optimizing the dispersion compensation.

The mechanism to generate ultrashort pulses may be described as follows: The gain material has a finite spectral bandwidth $\Delta\nu$. The laser cavity is resonant for distinct longitudinal modes which are associated with discrete frequencies ν_m . All of these modes have two main characteristics: the distribution of the corresponding electromagnetic wave needs to satisfy the boundary conditions at the cavity walls; consequently, their frequencies are separated from each other by $\delta\nu$ represented as: $\delta\nu = \frac{1}{T_{CRT}} = \frac{c}{2L}$, where T_{CRT} is the cavity round trip time, c is the speed of light and L is the length of the cavity (Fig.2.1A).

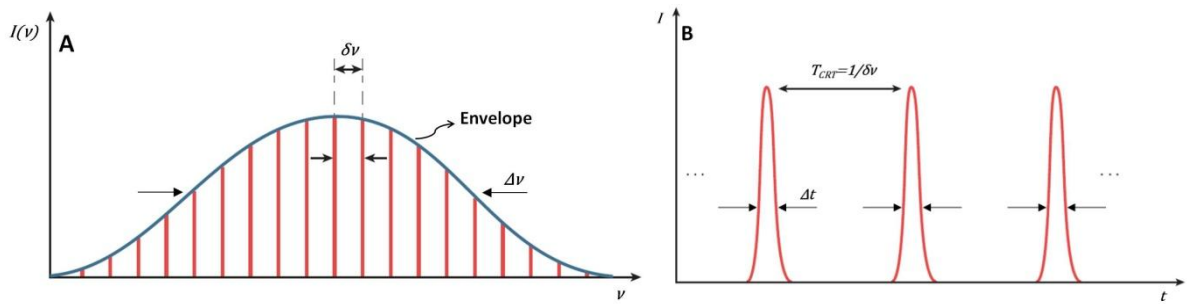


Fig. 2. 1: Modes inside the cavity covered by the laser gain medium (A), temporal profile of the pulse when the laser is mode locked (B) (Modified from [Ukr03]).

If no nonlinear element is present in the cavity, these modes oscillate independently of each other and at any point the laser output of such a laser will be a superposition of all the modes. This superposition results in a signal which is fluctuating in time. In order to obtain ultrashort pulses, the phase of the modes needs to be locked in order to establish a constant phase relationship.

2.2.1 Active mode locking

In active mode locking, an amplitude or phase modulator is placed inside the laser cavity. The opening and closing (or partial closing) of the modulator provides a modulation frequency. If the shutter remains open for a very short duration for which the pulse makes a round trip inside the cavity then mode locking will be favoured and all pulses not synchronised with the shutter will be strongly attenuated. This kind of modulation can be obtained by acousto-optical or electro-optical modulation (AOM or EOM).

2.2.2 Passive mode locking

In passive mode locking a saturable absorber may be placed inside the laser cavity that absorbs low intensity pulses while transmitting (or reflecting) high intensity pulses. A similar passive approach for mode locking is based upon the Kerr self focusing effect (also known as self mode locking). A Kerr lens (see also Appendix 2) medium possesses a refractive index which is intensity dependent. This can be written as:

$$n = n_0 + n_2 I, \quad (\text{Eq. 2.5})$$

where n is the total refractive index of the material, n_o is the linear refractive index, n_2 is the non-linear refractive index, and I is the intensity. If we consider a Gaussian beam, the value of the refractive index increases from periphery of the beam towards the centre. In Kerr lens mode locking the active material therefore can act as a lens. If the oscillator is resonant with the Kerr lens, longitudinal modes will get locked in phase in order to favour ultrashort pulse generation [Des91] [Aaa94].

It is also possible to place additional material inside the oscillator in order to generate the Kerr effect; however, this is usually avoided for reasons of simplicity. The schematic of a Ti:sapphire oscillator based on Kerr lens mode locking (KLM) without any additional Kerr lens medium is shown below in figure 2.2.

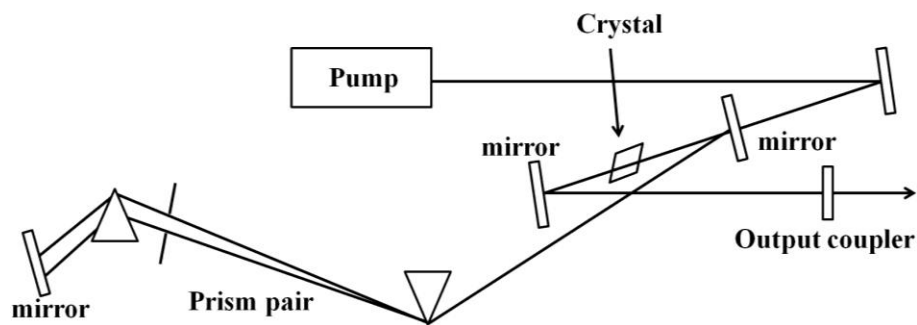


Fig.2. 2: *Ti:sapphire oscillator based on Kerr lens mode locking (Modified from [Dge06]).*

2.3 Architectures of ultrashort pulse laser systems

The threshold radiant exposure for corneal tissue is in the order of 1-2 J/cm² [Gol08]. Depending on the beam delivery and focusing optics, this typically requires pulse energies from fractions to multiples of a μ J. Typical oscillators working at tens of MHz typically can only provide pulse energies up to 5–20 nJ [Pla10]. In order to obtain higher pulse energies, the oscillator dimensions have to be modified or amplification schemes need to be used.

2.3.1 Long oscillator

In this technique the pulse energy is increased by increasing the length of the oscillator cavity and thereby simultaneously reducing the repetition rate [Shc99]. This results in an increase in pulse energy by a factor about equivalent to the reduction in repetition rate. Long oscillators are compact and relatively economical, however surgical laser systems based on these need to use relatively high numerical aperture (N.A.) focusing optics (Fig. 2.3).

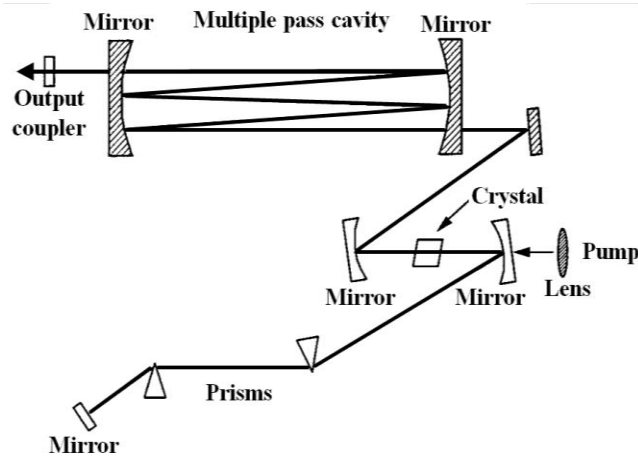


Fig.2. 3: Schematic of multiple-pass cavity (Modified from [Shc99]).

2.3.2 Chirped pulse amplification

The concept of Chirped Pulse Amplification (CPA) was originally proposed by Strickland and Mourou [Str85]. Pulses generated by an oscillator can be amplified by single or multiple passes through another active medium. In order to avoid parasitic non-linear effects and damage to the crystal due to the high peak power of the amplified pulse, the pulse is first stretched to decrease its peak power. The pulse then passes through the gain medium (single or multi-pass depending upon the architecture) and the amplified pulse is then compressed to achieve its actual pulse duration (Fig.2.4).

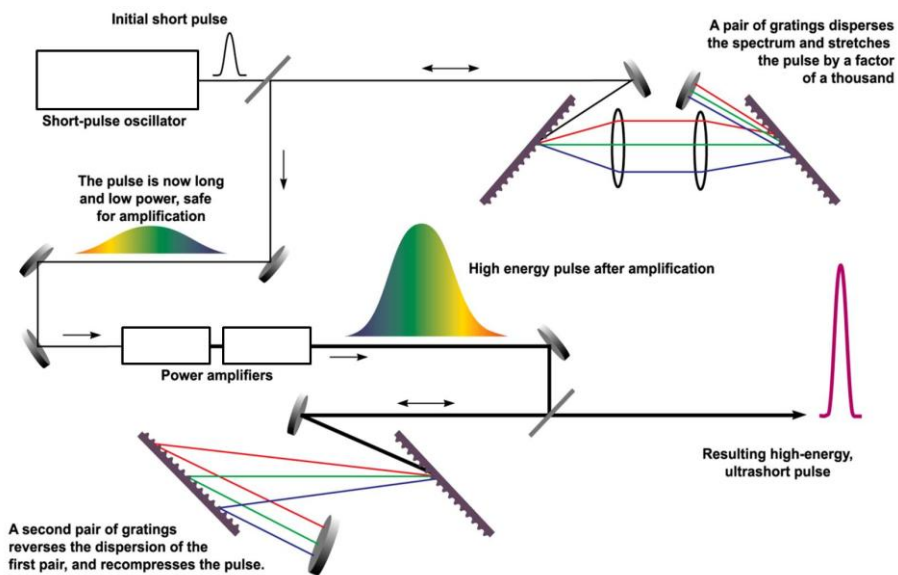


Fig.2. 4: Schematic diagram for chirped pulse amplification (Modified from [Lln95]).

In the following sections, two approaches based on this principle will be presented.

2.3.2.1 Regenerative amplifier

In regenerative amplification, a stretched output pulse from an oscillator is selected and injected into an amplification cavity, where it remains for several round-trips until it reaches a certain amount of energy. It is then coupled out of the cavity by an acousto-optical or electro-optical element, often a Pockels cell.

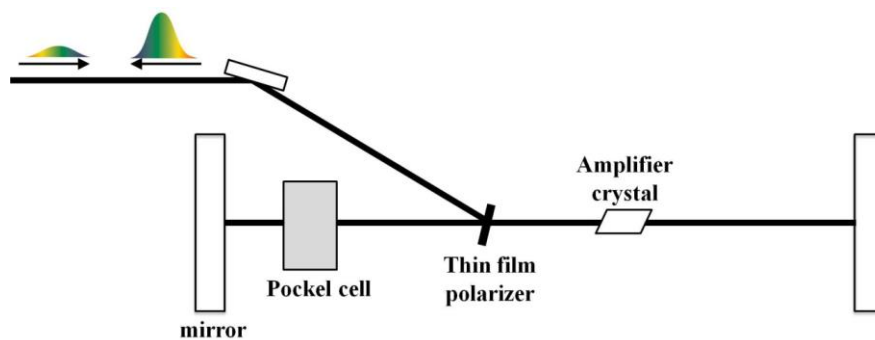


Fig.2. 5: *Chirped pulse amplification based on regenerative amplification.*

2.3.2.2 CPA based on optical fibres

The confinement of the oscillator modes in doped optical fibres provides an efficient amplification scheme in comparison to bulk crystals. The use of large mode area fibres (LMA) permits to reduce non-linear effects that may arise due to the propagation of the energetic pulses [Shö01]; double clad fibres permit to use laser diodes as pump sources. An example is shown in figure 2.6. The setup consists of an oscillator based on an ytterbium doped crystal; it is followed by an acousto-optical modulator permits the transmission of laser pulses with a repetition rate in the range of hundreds of kHz. The pulses are then stretched and fed into the diode pumped LMA that will amplify the laser pulses [Mha09] [Lku07] [Yza08]. The amplified output pulses are then compressed.

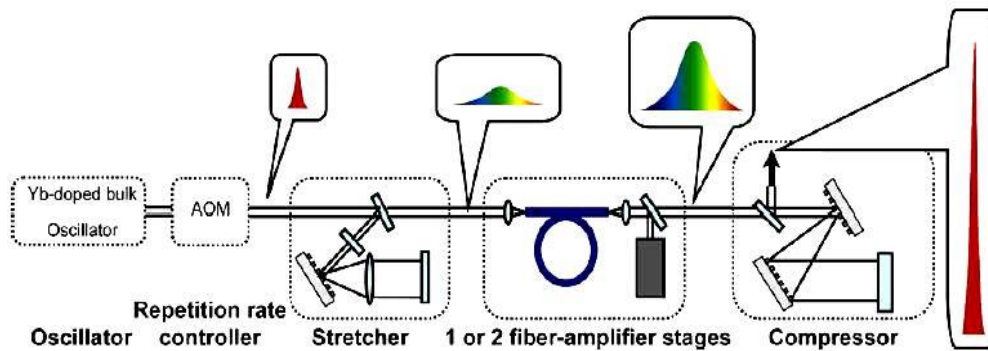


Fig.2. 6: Chirped pulse amplification based on LMA fibre [Pla10].

2.4 Gain media

Titanium-sapphire crystal is one of the most used laser medium since late 1990s. Amplified Ti:sapphire lasers can provide very high pulse energy and short pulse duration (<10 fs) at around 800 nm. These systems require pumping in the green part of electromagnetic spectra, which can be obtained by using argon ion lasers or frequency doubled lasers using neodymium- or ytterbium-doped gain media, which are impractical for compact clinical laser systems (Direct diode-pumping of Ti:Sa lasers was realised only recently and needs considerable further improvement [Pwr11] [Cgd12]). The pumping system can be made compact by using powerful diodes capable of pumping Ytterbium (Yb) and Neodymium (Nd) doped crystals. However, due to small gain band width of these materials they can produce pulse duration of hundred of femtosecond which is very high in comparison to Ti:sapphire. These systems can produce wavelength close to $1\mu\text{m}$ and by using these crystals makes the system compact. These elements can be use with different host materials. Different properties of these host materials are summarised in table 2.2.

Ion	Common host crystal/s	pump wavelegth/s (nm)	output wavelegths (nm)	Diode pumping
Ytterbium (Yb ³⁺)	Y ₃ Al ₅ O ₁₂ (YAG), YVO ₄ (yttrium vanadate), Glass (silicates and phosphates)	940	1020–1070	Yes
Neodymium (Nd ³⁺)	Y ₃ Al ₅ O ₁₂ (YAG), YVO ₄ (yttrium vanadate), YLiF ₄ (YLF), Glass (silicates and phosphates)	808 and 869	1064, 1047, 1053, 1342, 946	Yes
Titanium (Ti ³⁺)	sapphire	514 and 532	650–1100	No*

Table 2. 2: *Different ions capable of producing ultrashort pulses close to 1 μm. (*Direct diode-pumping of Ti:Sa lasers was realised only recently and needs considerable further improvement [Pwr11] [Cgd12]).*

2.5 Wavelength conversion by non-linear optics

2.5.1 Second order non-linear susceptibility

When an electromagnetic wave travels through a material it polarises the atoms and molecules of the medium. For moderate field strengths, the polarisation is proportional to the electric field, which can be expressed as:

$$P(t) = \epsilon_0 \chi E(t), \quad (\text{Eq. 2.6})$$

where $E(t)$ is the time-dependended field amplitude, P is the polarisation, ϵ_0 is the permittivity of free space, and χ is electric susceptibility.

If the amplitude of the electric field reaches orders of magnitude comparable to the inter-atomic electric field which are typically around 10^{11} V/m [Rwb08], the above equation will no longer be valid. In this is the regime, nonlinear concepts need to be used to describe the associated optical phenomena. In the case of strong electric fields like those that can be obtained with ultrafast lasers, the above equation can be extended in terms of power series [Bea07].

$$P(t) = \varepsilon_o (\chi^{(1)} E^1(t) + \chi^{(2)} E^2(t) + \chi^{(3)} E^3(t) + \dots) . \quad (\text{Eq. 2.7})$$

In equation 2.7, $\chi^{(2)}$ and $\chi^{(3)}$ represent the second and third order non-linear susceptibilities of the material under consideration. Some physical phenomena associated with $\chi^{(2)}$ and $\chi^{(3)}$ are:

$\chi^{(2)}$: Second harmonic generation, sum and difference frequency generation, parametric generation and amplification.

$\chi^{(3)}$: Four wave mixing, Kerr effect, multi-photon absorption and Brillouin-scattering.

In the framework of the present thesis, however, we will limit our considerations to the second order non-linear optical susceptibility. Detailed discussions of third order effects can be found in references [Yrs92] [Bea07] [Rwb08]. If the electric field contain two oscillating electric fields at ω_1 and ω_2 . The electric field can be written as a combination of the two fields.

$$E(t) = E_{(1)} \cos(\omega_1 t) + E_{(2)} \cos(\omega_2 t) . \quad (\text{Eq. 2.8})$$

By plugging equation 2.8 into equation 2.7 we obtain:

$$P(t) = \varepsilon_o \chi^{(2)} \left(\frac{E_1}{2} [\cos(2\omega_1 t)] + \frac{E_2}{2} [\cos(2\omega_2 t)] + \frac{E_1}{2} + \frac{E_2}{2} + E_1 E_2 [\cos(\omega_1 + \omega_2)t + \cos(\omega_1 - \omega_2)t] \right) . \quad (\text{Eq. 2.9})$$

The first two terms contain the doubled original frequencies, while the last two terms contain the sum and the difference of the two initial frequencies. The two middle terms describe the DC component which is usually referred to as electro-optical rectification. In mathematical analysis of the different optical parametric processes that will be presented in this thesis $\chi_{ijk}^{(2)}$ will be replaced by another new susceptibility tensor defined by d_{ijk} [Rwb08], where ‘ i ’ can have values 1,2, and 3 which correspond to the x , y and z axes and ‘ jk ’ can have values 1,2,3,4,5, and 6 which correspond to combinations of different axes xx , $xy = yx$, $xz = zx$, yy , $yz = zy$ and zz . As an example, d_{31} represents the pump wave polarisation along the z axis and the polarisation of the generated wave along the x axis whereas d_{33} represents the polarisation of both pump and generated beam along the z axis [Rwb08]. This process will help to reduce the 27 elements of $\chi_{ijk}^{(2)}$ down to 18.

$$d_{ijk} = \frac{1}{2} \chi_{ijk}^{(2)} . \quad (\text{Eq. 2.10})$$

jk can be converted to l according to the following table:

jk	11	22	33	23,32	31,13	12,21
l	1	2	3	4	5	6

Table 2. 3: conversion of different jk to l .

$$d_{il} = \begin{bmatrix} d_{11} & d_{12} & d_{13} & d_{14} & d_{15} & d_{16} \\ d_{21} & d_{22} & d_{23} & d_{24} & d_{25} & d_{26} \\ d_{31} & d_{32} & d_{33} & d_{34} & d_{35} & d_{36} \end{bmatrix} \quad (\text{Eq. 2. 11})$$

2.5.2 Coupled wave equations

Optical parametric processes can be analysed by using coupled wave equations. These equations can be solved for a particular second order non-linear process such as OPG and OPA in order to calculate the amplitudes of the fields and their gain. These equations can be obtained by using Maxwell's equation for a non-conducting dielectric medium with no free charges [Ash06] [Bea07]:

$$\nabla^2 E = \mu \epsilon_0 \frac{\delta^2 E}{\delta^2 t} + \mu \frac{\delta^2 P}{\delta^2 t}, \quad (\text{Eq. 2.12})$$

where E is the electric field, μ is the permeability, t is time, ϵ_0 is the permittivity of free space and P polarisation. If we assume that the field propagates along the z -axis, we can calculate the electromagnetic field inside the non-linear media by replacing polarisation in the above equation with the polarisation of the medium without first and third order susceptibility

$$\frac{\delta^2 E}{\delta^2 z} = \mu \epsilon \frac{\delta^2 E}{\delta^2 t} + \mu \frac{\delta^2 (\epsilon_0 \chi^{(2)} E^2)}{\delta^2 t}, \quad (\text{Eq. 2.13})$$

where ϵ is the permittivity of the medium. The conservation of energy for a non-linear optical process in which three waves are interacting can be written as

$$\omega_3 = \omega_1 + \omega_2, \quad (\text{Eq. 2.14})$$

where ω_1 and ω_2 are optical frequencies whose sum is equivalent to the highest frequency ω_3 .

The electric field for each of the frequency can written as:

$$\begin{aligned} E_1(z, t) &= \frac{1}{2} [E_1(z) e^{i(k_1 z - \omega_1 t)} + E_1^*(z) e^{-i(k_1 z - \omega_1 t)}] \\ E_2(z, t) &= \frac{1}{2} [E_2(z) e^{i(k_2 z - \omega_2 t)} + E_2^*(z) e^{-i(k_2 z - \omega_2 t)}] \\ E_3(z, t) &= \frac{1}{2} [E_3(z) e^{i(k_3 z - \omega_3 t)} + E_3^*(z) e^{-i(k_3 z - \omega_3 t)}] \end{aligned} \quad (\text{Eq. 2.15})$$

By using equation 2.15 along with the Maxwell's equation (2.13) will give us (for calculation see [Bea07])

$$\begin{aligned}
\frac{\delta E_1(z)}{\delta z} &= -i(2\omega_1 \varepsilon_o) \left[\frac{\mu_o}{\varepsilon_1} \right]^{\frac{1}{2}} d_{eff} E_3(z) E_2^*(z) e^{i\Delta kz} \\
\frac{\delta E_2(z)}{\delta z} &= -i(2\omega_2 \varepsilon_o) \left[\frac{\mu_o}{\varepsilon_2} \right]^{\frac{1}{2}} d_{eff} E_3(z) E_1^*(z) e^{i\Delta kz} , \\
\frac{\delta E_3(z)}{\delta z} &= -i(2\omega_3 \varepsilon_o) \left[\frac{\mu_o}{\varepsilon_3} \right]^{\frac{1}{2}} d_{eff} E_1(z) E_2^*(z) e^{i\Delta kz}
\end{aligned} \tag{Eq. 2.16}$$

where ε_i is the permittivity inside the medium and Δk is the phase velocity mismatched (see section 2.6). The set of these three equations is called coupled wave equation. This set of equations can help to analyse different non-linear optical phenomena involving three waves inside a non-linear optical media with susceptibility $\chi^{(2)}$. By further developing the coupled wave equation it is possible to analyse experiments by using parameters such as gain at strong or weak depletion. In order to analyse in terms of amplitude the coupled wave equation can be represent in terms of the intensity. With some simplification, the Manley-Rowe relation may be derived [Bea07]. This equation describes the energy flow between the interacting waves. Physically, it means that the destruction of one photon at ω_3 inside the non-linear medium will generate two photon at two different frequencies whose sum is equivalent to the original frequency or *vice versa*.

$$\frac{\delta}{\delta z} \left(\frac{I_1}{\omega_1} \right) = \frac{\delta}{\delta z} \left(\frac{I_2}{\omega_2} \right) = - \frac{\delta}{\delta z} \left(\frac{I_3}{\omega_3} \right). \tag{Eq. 2.17}$$

2.5.3 Non-linear optical crystals

Many nonlinear optical crystal materials are available that can be used for wavelength conversion. These include lithium niobate (LiNbO₃), potassium titanyl phosphate (KTP), lithium tantalate (LiTaO₃), β -barium borate (BBO), Lithium Triborate (LBO), Potassium Dihydrogen Phosphate & Potassium Dideuterium Phosphate (KDP), Potassium titanyl arsenate (KTA), and Lithium Iodate (LiIO₃). Their choice depends upon their price, application, transmission, conversion efficiency, nonlinearity and damage threshold [Rrp]. Among them LiNbO₃, LiTaO₃, KTP, and KTA are ferroelectric non-linear crystals whose structure can be altered by using a technique known as periodic poling. Periodically poled crystals provide high conversion efficiency in comparison to their bulk counterparts and will be described in detail in section 2.6.2.

In this work we have used LiNbO₃. It consists of niobium, lithium, and oxygen atoms in a trigonal crystal lattice. It is a ferroelectric material which makes it suitable to use for periodic poling (section 2.6.2). It can be used for applications in its transparency range from 350-5200 nm. In comparison to other crystals it has a high value of the non-linear tensor element $d_{33} \approx 27\text{-}30(\text{pm/V})$. Different properties of LiNbO₃ are summarised in table 2.4 LiNbO₃ can also be doped with magnesium oxide (MgO). By doping it MgO it is possible to reduce its coercive value. This will help to apply fields lower in value for its fabrication than it will require for an un-doped LiNbO₃; this doping also provides resistance to photorefractive damage [Rrp]. The refractive index of LiNbO₃ can be calculated by using the Sellmeier equation. In this work we have considered the Sellmeier equation developed by D. H. Jundt [Dhj06].

Property	Value
Nature	Ferroelectric non-linear crystal
Melting point	~1250 °C
Coercive field	~20-24 kV/mm
values(pm/V)	$d_{22} = 2.7, d_{31} = 4.5, d_{33} \approx 27\text{-}30$

Table 2. 4: *Properties of LiNbO₃ crystal [Bfj08].*

2.6 Phase matching

In the previous paragraphs we have introduced the phase matching vector Δk that is present in all three coupled wave equations. Δk takes into account the difference of phase velocity between the three interacting waves propagating through a non-linear optical media and can be written as

$$\Delta k = k_3 - k_2 - k_1 = 0 \quad , \quad (\text{Eq. 2.18})$$

where k are the wave vectors of the three electromagnetic waves. As we will see below ideally the sum of the terms should be zero (perfect phase matching) in order to provide maximum efficiency (Fig. 2.7A). In such a case all the energy of the pumped photons will be transferred to the converted photons. However, this may not be achieved in reality. If the waves propagate beyond a certain distance (usually known as coherence length), they will no longer be in phase. This will result in energy being transferred back to the pump beam until the phase shift is sufficient to put the waves back in phase so that the pump photons start to provide energy to the signal wave again (Fig.2.7C) [Rwb08]. The reason for this mismatch can be understood by looking at the representation of the wave vector $k = \frac{2\pi n}{\lambda}$ which depends upon

the refractive index ‘ n ’, the value of which is different for different wavelengths. In real situations, Δk can be minimised by using either birefringent phase matching or quasi phase matching.

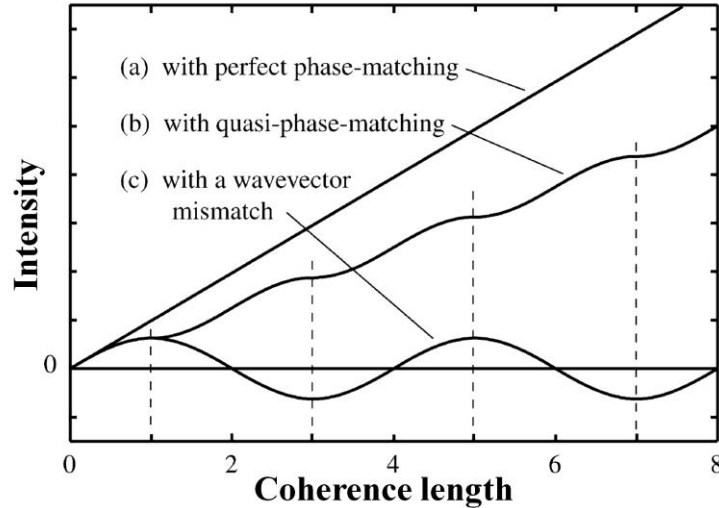


Fig.2. 7: Intensity of the converted optical intensity versus crystal length (a) phase matching, (b) quasi-phase matching schemes and (c) no phase matching.

2.6.1 Birefringent phase matching

In birefringent phase matching one uses the dependence of the refractive index on polarisation and on the axis of propagation. Waves that are polarised in parallel to the plane containing the optical axis experience a refractive index that depends upon the angle of propagation while the wave polarized perpendicular to the plane of the optical axis the refractive is independent of angle of propagation. In conclusion, if we chose correct polarisation and angle of propagation, for all three waves a situation can be achieve in which all the three waves will experience the same refractive index and results in phasematch parametric process (Fig.2.7A).

In real situations it is difficult to obtain birefringent phase matching. Another main problem is the ability to use the highest non-linear coefficient d_{il} .

2.6.2 Quasi phase matching

Quasi phase matching is another technique to achieve phase matching and has been used in this work. As described above, after travelling some distance ‘ L_C ’ inside the non-linear crystal, the signal accumulate a phase of π (pi) which results in energy being converted

back from the signal to to the pump. One way to overcome this problem is to reverse the phase after every coherence length. In this way, the amplitude of signal and idler instead of decreasing will increase further (Fig.2.7B). This method was first suggested in 1962 by J. A. Armstrong *et al.*; it is now known as periodic poling [Jaa62]. In this technique, by applying an electric field which is higher than the coercive field of the ferro-electric domains of the crystal, the domains can be periodically reverted with a certain period (Fig.2.8). This poling period (also known as grating period) can be calculated according to the formula

$$\Lambda = \frac{2\pi}{\Delta k}. \quad (\text{Eq. 2. 19})$$

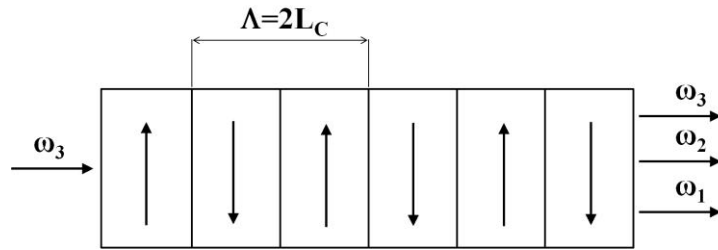


Fig.2. 8: *Periodic poling for quasi phase matching. In order to compensate the phase shift of π the ferro-electric domains should be flipped after every coherence length (L_C).*

The conversion efficiency is increased further by periodically poling along the direction of the highest value of the d_{il} tensor which for LiNbO_3 is d_{33} . By periodically reversing the direction of the ferroelectric domains the identity for phase velocity mismatched do not remain the same for the case of quasi phase matching and should be replace by a more general effective phase matching condition as follows:

$$\Delta k = k_P - k_S - k_I - k = 2\pi \left(\frac{n_P}{\lambda_P} - \frac{n_S}{\lambda_S} - \frac{n_I}{\lambda_I} - \frac{1}{\Lambda} \right). \quad (\text{Eq. 2.20})$$

In conclusion, by using periodically poled structures, different objectives can be met simultaneously:

1. It allows us to obtain optical conversion for those wavelengths for which it is impossible to achieve birefringent phase matching.
2. It allows using the largest element of non-linear tensor, which is for the case of periodic poled lithium niobate is $d_{33} \approx 27 \text{ pm/V}$.
3. Different gratings can be built on a single crystal that will help to generate different sets of down converted wavelengths.

The detailed characteristic of the periodic poled lithium niobate crystal used in this work is described in chapter 4.

2.7 Optical parametric processes

In this work we have realised set-ups based on two optical parametric processes which are Optical Parametric Generation (OPG) and Optical Parametric Amplification (OPA). These two processes are described below.

2.7.1 Optical parametric generation (OPG)

Optical parametric generation (OPG) is the inverse of sum frequency generation (SFG). In this process, a laser beam focused inside a non-linear material generates all possible wavelength combinations that satisfy energy ($\omega_P = \omega_S + \omega_I$) and momentum (phase velocity) ($\Delta k = k_P - k_S - k_I = 0$) conservation (Fig. 2.9);

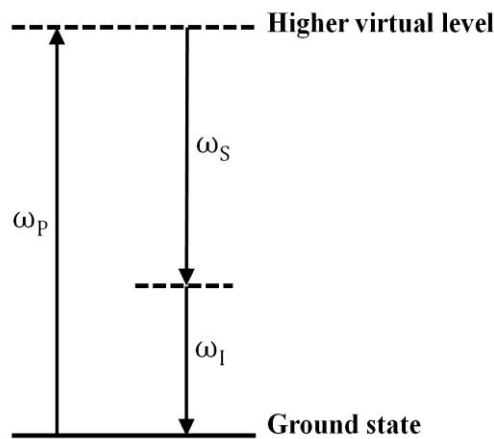


Fig.2. 9: Energy level scheme for optical parametric generation (OPG).

ω being is the angular frequency, k is momentum vector and P, S, I representing pump, signal and idler. An example of an experimental architecture for OPG is shown by figure 2.10. The laser beam provided by the laser system is focused inside the non-linear crystal in order to obtain the required energy density. The hereby created signal can be separated from the pump and the idler beams by a dichroic mirror. The pump and idler can later be separated by using an additional dichroic mirror. The OPG geometry has a simple architecture and is appropriate for applications that require relatively small pulse energies in the low microjoules range. The energy of the signal can be increased by increasing the pump energy or by increasing the length of the non-linear crystal (while respecting the damage threshold).

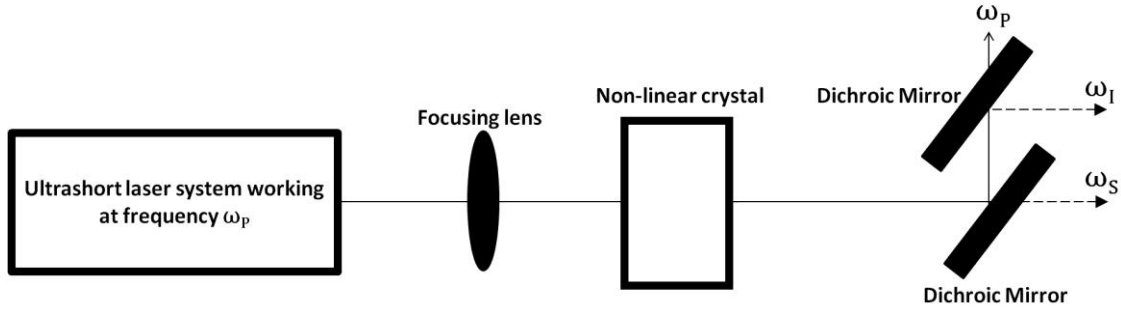


Fig. 2. 10: *Optical parametric generation.* $\omega_p, \omega_s,$ and ω_i are pump, signal and idler frequencies (see text for detail).

The complete mathematical description of optical parametric generation can be found for instance in [Rlb77] [Jaa62] [Mle13]. In short, if the coupled wave equation is solved in the limit of negligible pump depletion, the gain for a given length (L) of the non-linear crystal will be:

$$Gain(L) = \Gamma^2 \frac{\sinh^2\left(L \sqrt{\Gamma^2 - \left(\frac{\Delta k}{2}\right)^2}\right)}{\Gamma^2 - \left(\frac{\Delta k}{2}\right)^2}, \quad \Gamma^2 = \frac{2 \omega_s \omega_i}{\epsilon_o n_p n_s n_i c^3} d_{eff}^2 I_p. \quad (\text{Eq. 2.21})$$

Γ has the dimension of an inverse length and is represented by the above formula, where n is the refractive index, c is the speed of light in vacuum, I_p is the pump intensity and d_{eff} is the effective non-linear element of the non-linear tensor. In the limit of weak pump intensity $\Gamma \ll \frac{\Delta k}{2}$, the equation 2.21 becomes:

$$Gain(L)_{\Gamma \text{ small}} = \Gamma^2 L^2 \text{sinc}^2\left(\frac{\Delta k L}{2}\right), \quad (\text{Eq. 2.22})$$

This relation is governed by the sinc^2 function which means that in order to obtain high gain the product $\Delta k L$ should be as small as possible. Since L cannot be zero it requires that Δk be minimal. When working in this regime the gain increases with approximately the square of the length. On the other hand, for a very strong pump intensity ($\Gamma \gg \frac{\Delta k}{2}$) and a small value of Δk the gain grows exponentially.

$$Gain(L)_{\Gamma \text{ large}} \propto \exp(2 \Gamma L). \quad (\text{Eq. 2.23})$$

2.7.2 Optical parametric amplification (OPA)

In order to increase gain (energy) and coherence at a particular wavelength, different geometries of OPA can be used. As an example a two stage geometry is presented here where the pulses created by the first stage are amplified by a second stage (figure 2.11). With the help of a beam splitter, the laser pulses coming out from the femtosecond laser system can be divided into two parts. The beam shown as dotted line passes through the first non-linear crystal. The signal that is created by this crystal can be separated from the pump and idler with the help of a dichroic mirror. The signal is then focused along with the rest of the beam (solid line) into the second non-linear crystal. If the configuration of the second non-linear crystal permits the amplification of the signal wavelength and if the temporal and spatial alignments are appropriate, the output will be more coherent at the wavelength that was fed into the second crystal and more energy will be obtained [Tsu01] [Mma07] [Aga97] [Jkr13]. In order to increase the energy further, one or two more arms can be added to the existing geometry.

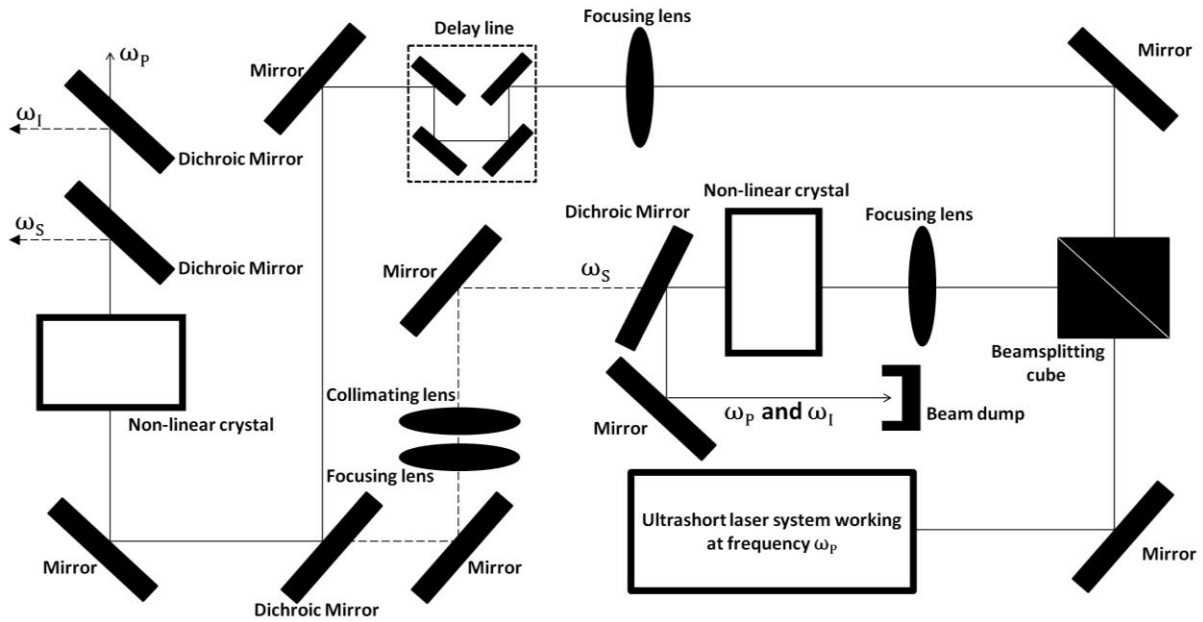


Fig. 2. 11: *Optical parametric amplification.* $\omega_p, \omega_s,$ and ω_l are pump, signal and idler frequencies (see text for detail).

The gain for the OPA can be written as:

$$Gain(L) = 1 + \Gamma^2 \frac{\sinh^2\left(L \sqrt{\Gamma^2 - \left(\frac{\Delta k}{2}\right)^2}\right)}{\Gamma^2 - \left(\frac{\Delta k}{2}\right)^2}, \quad \Gamma^2 = \frac{2 \omega_s \omega_l}{\epsilon_0 n_p n_s n_l c^3} d_{33}^2 I_p. \quad (\text{Eq. 2.24})$$

For $\Gamma \ll \frac{\Delta k}{2}$ equation 2.24 becomes:

$$Gain(L)_{\Gamma small} \approx \Gamma^2 L^2 \text{sinc}^2\left(\frac{\Delta k L}{2}\right). \quad (\text{Eq. 2.25})$$

2.8 Conclusion

- In this chapter we have presented the theory of ultrashort laser pulse generation and non-linear optical parametric wavelength conversion.
- Ultrashort laser pulses can be created by using mode locking. This locking mechanism can be either active or passive.
- Laser pulses can be amplified by using chirped pulse amplification.
- When ultrashort pulses are focused inside the non-linear crystal they give rise to different non-linear effects such as SHG, DFG, and SFG.
- LiNbO₃ crystal is one of the most frequently used non-linear crystals. The non-linear conversion efficiency of this crystal can be increased by using periodically poled structures in the direction of highest non-linear coefficient.
- OPG and OPA are two different non-linear effects that can be used to create two photons at different frequency whose sum is equivalent to the pump photon.

Chapter III

Interaction of ultrashort laser pulses with corneal tissue

Since the discovery of the laser in 1960, lasers have found widespread uses in industry, research, and medicine. Lasers can produce continuous wave emission as well as very short pulses down to the femtosecond time scale. When used in medicine, depending upon their time of interaction with the tissue, different physical phenomena dominate the laser-tissue interaction process.

We start this chapter with a short introduction of the different mechanisms that are characteristic for the interaction at different time scales. We then discuss in detail the interaction of ultrashort laser pulses with tissue and address different side effects such as shock wave generation and bubble formation.

3.1 Mechanisms of laser-tissue interaction

The interaction of the laser pulse with tissue depends upon wavelength, power and energy density and exposure time. Fig. 3.1 gives an overview of the principal interaction mechanisms and the associated laser power and the duration of the interaction. The straight lines indicate two different energy densities (1 and 1000 J/cm²). The circles in the diagram represent five different (not necessarily mutually exclusive) interaction regimes and their associated dominating interaction mechanisms [Ima06][Mhn93][Mmj11]. In the following we will discuss these mechanisms in more detail.

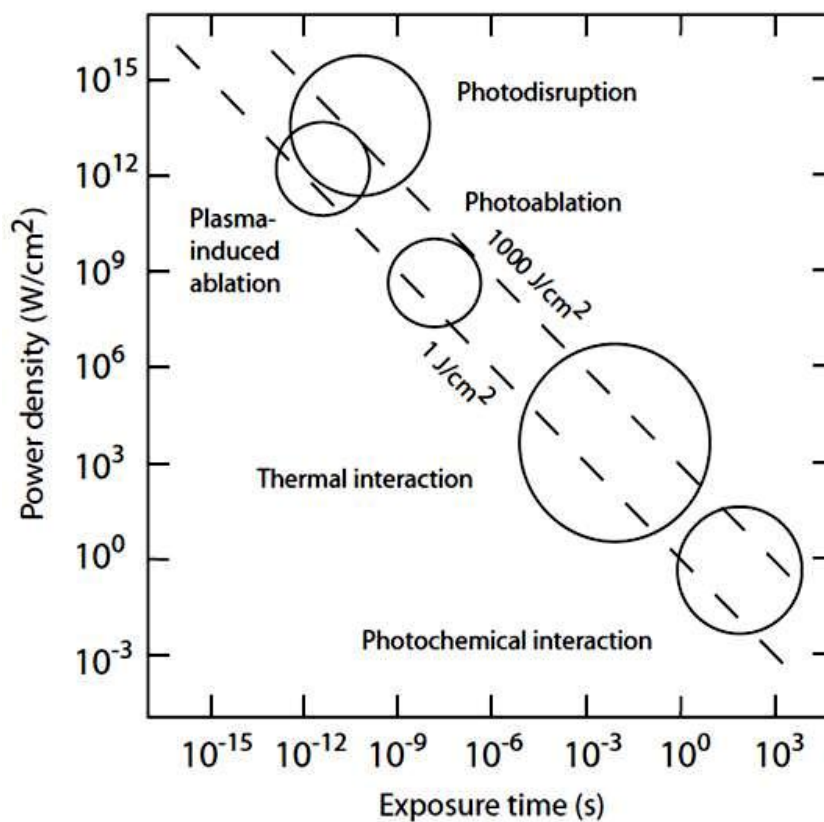


Fig.3. 1: Classification of different interaction regimes depending on power density and exposure time. The circles indicate the orders of magnitude of exposure time and power density typical for different types of interactions. Modified from [Mhn93].

3.1.1 Photochemical interaction

Photochemical interactions take place at very low energies with interaction durations that can range from several seconds to continuous interaction. In photochemical interaction, the laser light favours chemical reactions in macromolecules which have been introduced into

the organism, or in the tissue itself. This kind of interaction is the basis of photodynamic therapy (PDT) and biostimulation [Mhn93].

3.1.2 Photothermal interaction

As the name suggests, photothermal interaction gives rise to an increase in temperature. Typical power densities are higher than in the previous case; interaction durations range from microseconds to seconds. Thermal interaction can lead to phase transitions in matter such as coagulation, vapourisation, carbonisation, and melting [Mhn93].

3.1.3 Photoablation

If the power density is high enough it is possible to ablate the material without creating damage in the vicinity of the ablated tissue. First discovered by Srinivasan and Mayne-Banton, photoablation requires very high power densities (10^4 - 10^{10} W/cm²) which can be achieved by using pulsed lasers; it is typically performed using UV lasers. One of the main applications of photoablation in ophthalmology is in refractive surgery where it is used to reshape the cornea in order to modify the optical properties [Mhn93].

3.1.4 Plasma induced ablation and photodisruption

This type of interaction occurs at time scales from nanoseconds to femtoseconds. It is the main type of interaction that will be discussed in this thesis. It is characterised by the formation of plasma at the laser focus that results in the creation of optical breakdown leaving an incision inside the volume of the tissue. Plasma induced photodisruption is the process used for eye surgery assisted by ultrashort pulse lasers and will be discussed in detail below [Mhn93].

3.2 Non-linear optical breakdown in tissue

When describing laser-induced optical breakdown in tissue, the physical parameters of water are usually used. The ionisation energy of water is 6.5eV [Fwi76] [Dnn83] [Dgr79] [Cas91]. The wavelength that is usually used for clinical purposes (in ophthalmology) is close to 1micron; the corresponding photon energy of 1.17 eV is therefore not sufficient to ionise a water molecule. The free electrons necessary to induce optical breakdown are generated by nonlinear processes.

According to [Lvk65], for excitation assisted by ultrashort laser pulses the band gap energy (Δ) needs to be replaced by an effective band gap energy that takes into account the oscillation energy of the electron due to the electric field of the laser pulse which leads us to the following formula (Eq. 3.1).

$$\tilde{\Delta} = \Delta + \frac{e^2 F^2}{4m\omega^2}, \quad (\text{Eq. 3.1})$$

where ω and F are the frequency and amplitude of the electric field of the laser pulse and e and m are the charge and reduced mass of electron.

An electron can overcome the band gap by gaining energy either by photoionisation or by impact ionisation (Fig. 3.2). The two competing processes contribute to photoionisation are multiphoton ionisation and tunnelling, followed by avalanche ionisation.

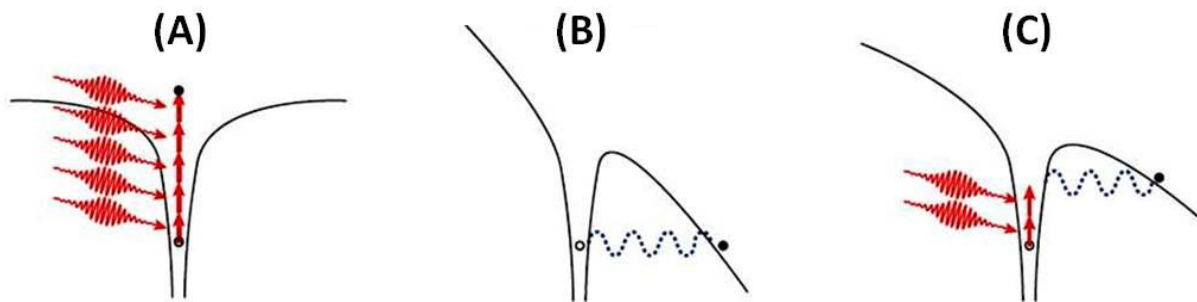


Fig.3. 2: Free electron generation (A) multiphoton ionisation; (B) tunneling ionisation; (C) combined multiphoton excitation and tunneling (see text). Modified from [Cbs01].

3.2.1 Multiphoton ionisation (MPI)

In contrast to situations where a single photon with enough energy is sufficient to overcome the band gap, in multiphoton ionisation an electron absorbs photons from the laser pulse until the total energy becomes equal or greater than the band gap energy. (Fig. 3.2A)

3.2.2 Tunneling

In tunnel ionisation the electric field of the laser pulse lowers the potential barrier of the atom which links the electron to the molecule. If the electric field is high enough, it is possible for the electron to tunnel through the barrier and become a free electron. (Fig.3.2B)

Once a free electron is available in the conduction band, it may gain further energy from the laser pulse through inverse bremsstrahlung. It then can elastically collide with a bound

electron, thereby permitting the latter to overcome the band gap. This results in two free electrons available in the conduction band. These two electrons may further absorb energy from the laser pulse and repeat the process, which leads to a rapid increase of free electrons (an “avalanche”) in the volume of the laser focus. (Fig. 3.3).

The respective contribution of multiphoton ionisation and ionisation by tunnelling followed by avalanche ionisation is usually described in terms of the Keldysh parameter given as (Eq. 3.2) [Lvk65]

$$\gamma = \omega \frac{\sqrt{m\Delta}}{eE} = \frac{\omega}{\omega_t}, \quad (\text{Eq. 3.2})$$

where $1/\omega_t$ is the tunneling time through the potential barrier which is inversely proportional to the amplitude of the electromagnetic field E . For values of $\gamma \leq 1$ (that correspond to low frequencies and large field strengths) the dominating process will be tunneling. On the other hand for values $\gamma \geq 1$ (that correspond to optical frequencies and moderate field strengths) the dominating process will be multiphoton ionisation. For an intermediate value of the Keldysh parameter, both processes contribute (Fig. 3.2C).

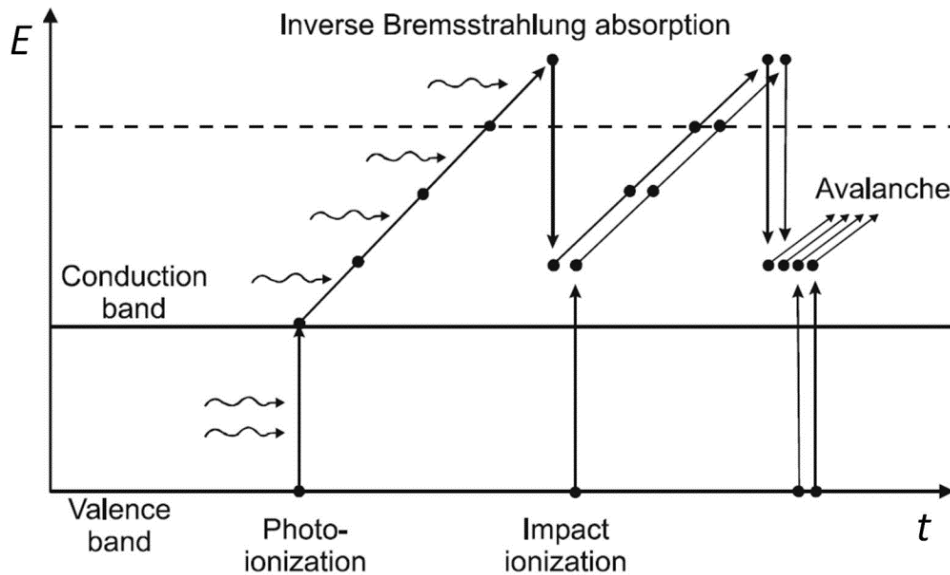


Fig.3. 3: Different physical processes that can lead to the generation of a free electron. An electron in the valence band can be elevated into the conduction band by multiphoton ionisation or tunnelling. Once in the conduction band, it can absorb photons through inverse bremsstrahlung. If energy is sufficient it is possible for the electron to extract another electron from the valence band collision. The resulting two electrons may repeat the process and thereby lead to the further generation of an “avalanche” of free electrons throughout the volume of the laser focus. (Modified from [Vog05]).

3.2.3 Rate equation

In a review presented by Vogel [Vog05], the time-dependence of the electron density ρ in the conduction band is presented. The following equation considers photoionisation (based on the Keldysh theory), cascade ionisation, diffusion and recombination losses:

$$\frac{d\rho}{dt} = \left(\frac{d\rho}{dt}\right)_{photo} + \eta_{casc} \rho - \eta_{diff} \rho - \eta_{rec} \rho^2. \quad (\text{Eq. 3.3})$$

The first term represents the rate of change in electron density due to photoionisation (multiphoton and/or tunneling ionisation), the second term represents cascade ionisation, and the last two terms represent losses due to diffusion or recombination. The cascade ionisation rate η_{casc} and the diffusion rate η_{diff} are proportional to the electron density, whereas the recombination rate η_{rec} is proportional to the square of the electron density as electrons and holes both will be involved in the interaction.

However, this model does not take into account heating due to processes like linear absorption, absorption by inverse bremsstrahlung, collision losses and absorption by free electrons. Additionally, in the case of either femtosecond illumination using multiple pulses, or nanosecond illumination, the temperature of the focal volume will be high enough to initiate thermal ionisation. A detailed calculation shows that for temperature above 5000K, thermal ionisation increases very rapidly with increasing temperature (Figure 3.4). In such a case the above rate equation will no longer be suitable to explain the rate of change of electron density inside the dielectric.

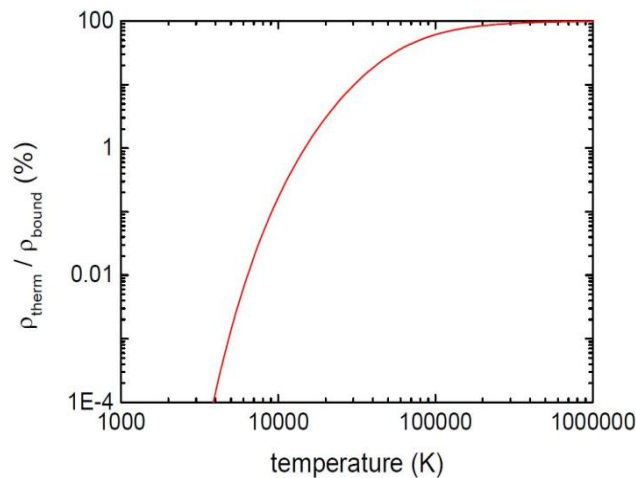


Fig.3. 4: Fraction of free electrons (in percent) as a function of temperature. ρ_{therm} and ρ_{bound} represent thermally generated electron density and bound electron density [Nob10].

In order to overcome this problem, Linz *et al.* [Nob10] have presented a rate equation that takes into account temperature rise and thermal ionisation and losses. They suggested that the rate equation be described in terms of normalised electron density R ($R = \rho/\rho_{\text{bound}}$) $R_{\text{therm}} = \rho_{\text{therm}}/\rho_{\text{bound}}$ instead of ρ in order to take into account the reduction of the number of electrons that will be available for thermal ionisation in the valance band by photoionisation and cascade ionisation. In addition to this, ‘ R ’ will also incorporate the reduction of the population of the ground state for very high values of irradiance.

Dividing the rate equation (Eq. 3.3) by ρ_{bound} will give us

$$\frac{dR}{dt} = \left(\frac{dR}{dt}\right)_{\text{photo}} + \eta_{\text{casc}} R - \eta_{\text{diff}} R - \eta_{\text{rec}} \rho_{\text{bound}} R^2 . \quad (\text{Eq. 3.4})$$

After considering the thermal ionisation and thermal losses, the final form may be written as:

$$\frac{dR}{dt} = \left(\frac{dR}{dt}\right)_{\text{photo}} + \left(\frac{dR}{dt}\right)_{\text{casc}} - \eta_{\text{diff}} (R - R_{\text{therm}}) - \alpha_{\text{rec}} (R - R_{\text{therm}})^2 + \left(\frac{\partial R}{\partial t}\right)_{\text{therm}} , \quad (\text{Eq. 3.5})$$

where $\left(\frac{dR}{dt}\right)_{\text{photo}}$ is equal to $\left(\frac{dR}{dt}\right)_{\text{MPI}} + \left(\frac{dR}{dt}\right)_{\text{tunnel}}$, $\left(\frac{dR}{dt}\right)_{\text{casc}}$ is the cascade/avalanche term, η_{diff} and α_{rec} are the diffusion and recombination rate constants that depend upon the $(R - R_{\text{therm}})$. Where $(R - R_{\text{therm}})$ represents reduction in the number of free electrons because of thermal ionisation, and the last term contains contributions from all temperature dependent terms that describe losses and thermal ionisation. The losses that have been considered here are: heat conduction, heating due to collisions during cascade ionisation, heating due to inverse bremsstrahlung followed by transfer of energy due to collision, heating by linear absorption, and heating due to recombination.

3.2.4 Breakdown criterion

The definition of ‘‘Optical breakdown’’ can be related to phenomena which can be observed experimentally: bubble or plasma formation. However, the breakdown threshold can also be defined in terms of a critical electron density (ρ_{cr}) for which the plasma becomes strongly reflective and absorbing. For wavelengths in the near UV, visible and near infrared spectral ranges this electron density is of the order of 10^{21}cm^{-3} . Mathematically, it can be written as [Vog05] [Nob10]

$$\rho_{\text{cr}} = \omega^2 \frac{m_c \epsilon_0}{e^2}, \quad (\text{Eq. 3.6})$$

where m_c and e are the mass and charge of the electron and ϵ_0 is the permittivity of free space. Figure 3.5 presents the values of irradiance and threshold that will be required to produce an electron density of 10^{21}cm^{-3} . By calculating these values for different wavelengths and pulse durations it was possible to identify two regions. Below around 10ps the energy density only weakly depends upon the wavelength. At this stage the pulse duration is small in comparison to recombination which will lead to a particular set of free electron and hence constant energy density at the focal volume [Vog05] [Nob10].

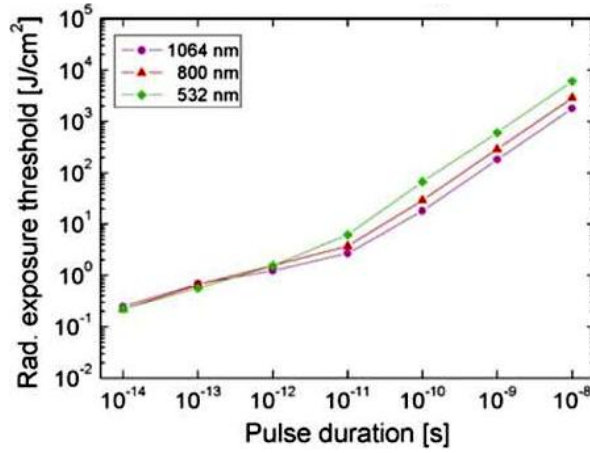


Fig.3. 5: Numerically calculated threshold radiant exposure for different pulse durations [Vog05].

However, this condition does not correspond to any parameter accessible to experimental observation such as bubble formation or plasma. Therefore, most modern studies use bubble formation inside the dielectric as breakdown criteria because it can be easily detected. [Nob10]

3.3 Mechanical effects associated with the non-linear optical breakdown

The pulse duration of a femtosecond laser pulse is very short compared to the time scale of acoustic relaxation (110 picoseconds for $N.A. = 1.3$ and $\lambda = 800 \text{ nm}$). This will result in a temperature rise inside the focal region and will result in maximum pressure rise due thermo-elastic stresses caused by temperature rise [Vog05] [Gpa99] [Gpa03] [Vog03]. Conservation of momentum requires that the stress wave emitted from a fixed volume contain compressive and tensile components. In water a cavitation bubble will form when the value of tensile

strength of water is reached. In pressure-temperature coordinates this corresponds to the temperature value that gives rise to tensile strain which is equal to the value of the kinetic spinodal of water [Vog05]. Table 1 presents the critical breakdown temperature T_{cr} for different pulse durations.

Pulse duration (τ_L)	Critical temperature (T_{cr}) in Kelvin
fs	441
50 ps < τ_L < 200 ps	500
ns	573

Table 3. 1: Breakdown temperature T_{cr} for different pulse durations [Nob10].

Linz and co-workers measured the wavelength dependence of the threshold for bubble formation using femtosecond laser pulses produced by an OPA system which were focused into water using an immersion microscope objective of $N.A.= 0.8$ (Fig. 3.6) [Nob10]. From figure 3.6 it can be seen that an energy density in the range of 1-3 J/cm² is required; the threshold appears to diminish with increasing wavelength (The typical bubble diameters are in the range of several hundred of nanometres [Vog08]). This can be compared with the values measured by Olivié *et al.* [Gol08] on the porcine corneal stroma and is given in Fig.3.7 which are of the same order of magnitude.

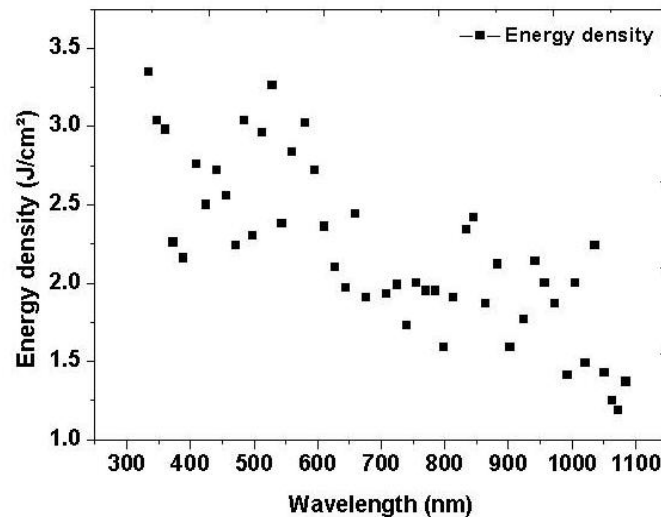


Fig.3. 6: Threshold energy density for bubble formation in water. (see text for detail, data from [Nob10]).

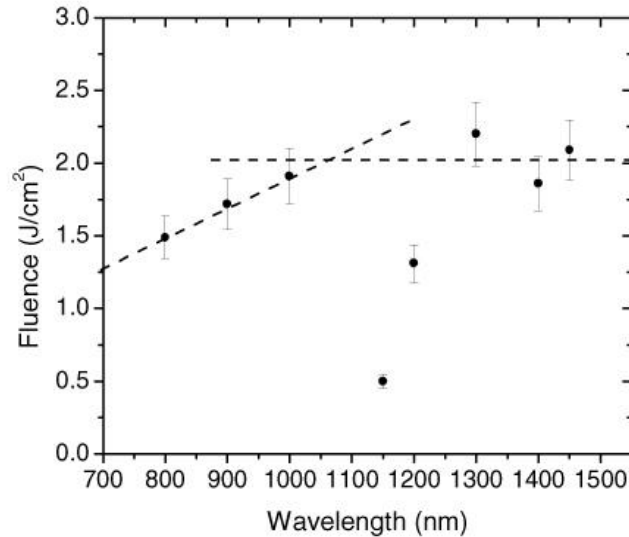


Fig.3. 7: Ablation threshold of porcine corneal stroma assisted by femtosecond laser pulses for different wavelengths [Gol08].

When optical breakdown is achieved, the compressive strain produces a stress wave that travels away from the focal area while the thermo-elastic stress inside the bubble drives the bubble expansion. Depending on the pressure amplitudes, two different techniques may be used to measure the shock wave amplitude:

- For pressure amplitudes above 100 MPa shock wave amplitude can be measured by using streak techniques.
- For pressure amplitudes below about 100 MPa this technique is not sufficiently accurate [Jno98] and fast hydrophones need to be used.

Vogel and co-workers measured the shock wave amplitude at a distance of 6mm away from the focus (in a direction perpendicular to the optic axis) for a wide range of pulse durations and for energies as high as 80 times the threshold values (Fig 5.12 in chapter 5).

The initial value of the stress wave can be estimated by extrapolating the result. Assuming that the amplitude of pressure follows a law with a general form $\text{Pressure} \propto 1/r^n$ (where n is a decay constant) will allow us to extrapolate our result. In literature, for 100 femtosecond pulses, decay constants between 1.13 and 1.12 have been reported [Vog05].

Because of the ellipsoidal shape of the laser focus and the created plasma, shock wave propagation is anisotropic. Numerical calculations shows that by considering the ellipsoidal shape 25% of the actual stress amplitude will travel in the direction perpendicular to the optical axis while approximately 5% of the total stress amplitude will travel in the direction of optical axis (Fig.3.8).

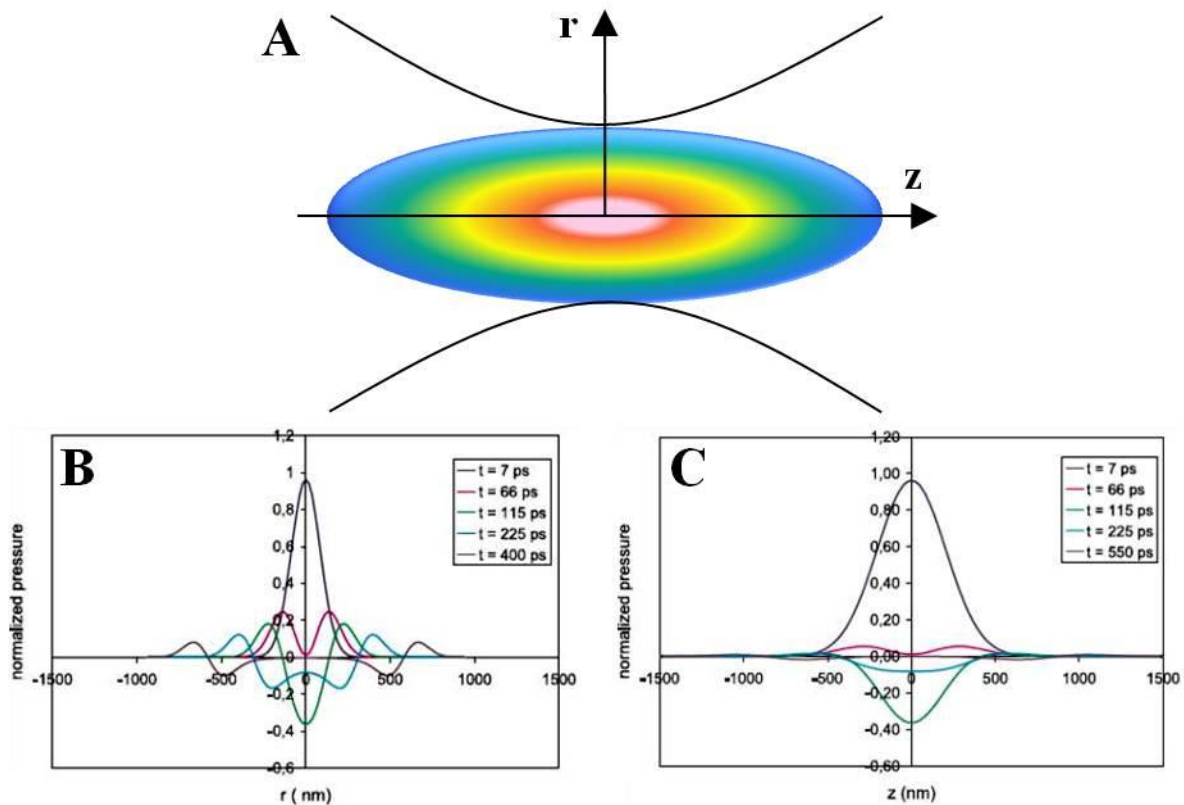


Fig.3. 8: Shock wave amplitude at different times in radial (r) and axial (z) directions where z represent optical axis, description of axial and radial direction use in the simulation(A), shock wave amplitude in radial direction (B), shock wave amplitude in axial direction (C) (modified from [Vog05]).

The later dynamics of the bubble after the emission of the shockwave depends on the size of the nucleus bubble (greater or equal to the focal volume). The volume of the nucleus is defined to be the region where the breakdown temperature (T_{CR}) is reached. For bubble size \ll focal volume, the bubble expands adiabatically until the average temperature of the bubble reaches the temperature of the liquid at the wall whereas for bubble sizes comparable to or larger than the focal volume the bubble expands more rapidly and the vapour pressure drops much faster than in the previous case. Simulation results that have been presented by Vogel *et al.* [Vog05] show that both cases will follow the same dynamics (Fig. 3.9). In their simulations, for the first case they have considered that it is a negative shock wave that drives the

bubble while in the other they have considered the vapour pressure of the contents inside the bubble. However, for laser energies much higher than threshold one also needs to take into account the rapture of the focal volume.

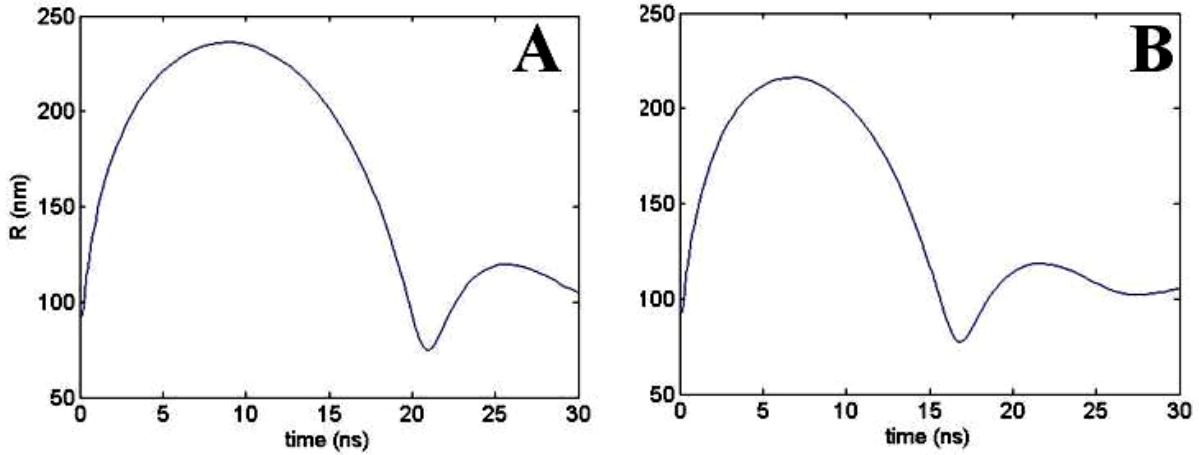


Fig.3. 9: *Bubble dynamics (A) bubble size \ll focal volume, (B) bubble size \geq focal volume.*

Finally, at each collapse the bubble will emit a shock wave that propagates away from the focal volume. Except for the shock wave that forms at the first collapse (amplitude almost equal to the first collapse), the amplitude of the shock wave will decrease periodically [Wla13].

3.4 Conclusion

- In this chapter we have presented the interaction of ultrashort laser pulses with corneal tissue.
- Ultrafast laser pulses can achieve optical breakdown inside the tissue through a combination of multiphoton ionisation and tunneling ionisation.
- The generated electrons are able to absorb photons through inverse bremsstrahlung. If the energy absorbed is higher than the band gap energy of electron it is possible for the electron to extract another electron from the valance band through elastic collision.
- The time evolution of their population within the focal volume can be described with the help of a rate equation. The rate equation presented in thesis incorporate two new terms: one describes loss of ionized electrons whereas the other describes electron ionisation due to temperature [Nob10].
- The optical breakdown inside the focal region will give rise to mechanical effects such as bubble formation and the generation of a shock wave.

-
- After optical breakdown, a shock wave propagates away from the focal region and a bubble forms which continues to expand until it has consumed the available stored energy. The amplitude of the shock wave can be in the range of MPa and decreases with the distance from the focal region: Pressure $\propto 1/r^n$ (where n is a decay constant with values between 1.13 and 1.12)
 - After maximal expansion, the bubble collapses and re-expands. The process continues until the stored energy has dissipated. At each collapse a shock wave is emitted the amplitude of which decreases with every collapse (except the amplitude of shock wave that form at the first collapse whose amplitude is almost equal to the generated shock wave due to optical breakdown).

Chapter IV

Optical parametric generator and amplifier based on a periodically poled magnesium doped lithium niobate crystal emitting microjoule femtosecond pulses in the short wave infrared²

4.1 Abstract

We present the use of periodically poled magnesium doped lithium niobate (PPMLN) crystals in the configuration of an Optical Parametric Generator (OPG) and an Optical Parametric Amplifier (OPA) pumped at a wavelength of 1.03 μm by a diode-pumped solid state laser emitting microjoule femtosecond pulses in the short wave infrared range (SWIR). The set-up notably provides an emission wavelength of 1650 nm. This wavelength had been previously identified as being optimal for femtosecond laser assisted corneal surgery in the case of pathological, light scattering tissue. The laser and wavelength conversion system is compact, rugged, and therefore potentially qualified for a use in clinical applications.

4.2 Introduction

Ultrashort pulse laser systems have been available in research laboratories since the 1980s. Nowadays, most laboratory systems are based on Titanium doped Sapphire crystals. Although their performance is unparalleled what pulse durations and energies are concerned, they need to be pumped in the visible range of the spectrum. This typically requires the use of gas lasers or frequency doubled solid state lasers, which makes the development of compact, portable systems impractical. Direct diode-pumping of Ti:Sa lasers was realised only recently and needs considerable further improvement [Pwr11][Cgd12].

² This chapter has been adapted from a manuscript which is currently in preparation for submission. Co-authors are Caroline Crotti, Florent Deloison, Jean-Pascal Caumes (NeTHIS), Fatima Alahyane, Antoine Courjaud (Amplitude Systèmes), Donald A. Peyrot, and Karsten Plamann. We would like to thank Marc Hanna, *Institut d'optique* Graduate School, Palaiseau, France for useful discussion and help with the experiments.

It was not until the first demonstration of diode pumped femtosecond lasers in the late 1980s and their subsequent further development during the 1990s that industrial or clinical applications of ultrashort pulse lasers could be envisaged [Eso01]. Typical systems use Neodym or Ytterbium doped crystals or fibres and have emission wavelengths just above 1 μm . Amplified systems can provide pulse energies in the μJ and mJ range with repetition rates up to several hundred kHz. Even though these laser systems are not able to provide extremely short pulses, they are convenient due to their compactness, robustness and their comparably moderate cost [Wsi12].

Ultrafast pulse lasers may be used in materials processing, product marking, for the writing of waveguides and optical gratings and for many other applications including laser surgery. Since the beginning of the last decade several clinical laser eye surgery systems have been commercialised which namely offer routines for refractive surgery, corneal grafting and cataract surgery [Pla10][Hks09][Drd12][Koz13]. Most of these systems are based on diode pumped ultrashort pulse lasers emitting pulses in the μJ range at wavelengths just above 1 μm and have enjoyed considerable economic success.

In previous studies we have shown that the performance of these laser systems can be unsatisfactory when working on pathological corneal tissue (for corneal grafting) or on sclera (for glaucoma surgery) [Pla10][Dap10][Ccr13], as light scattering processes then degrade the quality of the surgical laser beam. We were able to identify a spectral window of relative tissue transparency centred at 1.65 μm where light absorption is acceptably low and light scattering is almost eliminated [Pla10][Dap10] (Similar arguments apply for crystalline lens where a wavelength at about 1.3 μm may improve the surgical laser performance for cataract surgery, see Appendix 1).

Ultrashort pulse lasers with the required properties are not readily available for this wavelength range and therefore need to be developed. Laser emission at specific wavelengths may be obtained by fine-tuning emission spectra of existing laser materials or by the development of new materials. In a joint research project, our project partners Morin *et al.* have developed an erbium-doped fibre laser emitting 2 μJ pulses with a central wavelength of 1.6 μm at a repetition rate of 200 kHz [Fmo09].

However, these approaches remain limited in the choice of the output wavelength and in the accessible pulse energy. These limitations can be overcome by using conversion schemes

based on nonlinear optical crystals such as lithium niobate (LiNbO_3), potassium titanyl phosphate (KTP), β -barium borate (BBO) [Sck11] [Cmc98] [Zsu07] [Ypu07] [Mjo03] [Mra02] [Vpe09] [Mlb95]. These schemes are based on the principle of three-wave-mixing, where the pump beam is used to generate a signal beam at the desired wavelength. For reasons of energy and momentum conservation, an additional idler beam is created simultaneously at a frequency corresponding to the difference between the pump and signal frequencies. When using monolithic crystals, phase matching has to be ensured by using birefringent properties of the crystals and maintaining defined angles between the pump and signal waves. Such optical set-ups are somewhat complex and may require regular realignment. To overcome these problems, specially designed periodically poled crystals may be used in which the sign of the nonlinear susceptibility is reversed after every coherence length. This ensures quasi phase matching, which compensates for the differences in phase velocities [Dsh07][Rby97].

The first OPG that uses PPMLN was described in 1997 pumped by a frequency doubled Er-doped fibre mode-locked laser [Aga97]. The system was able to produce nanojoule pulses with pulse durations of 300fs; emission wavelengths were in the range between 1-3 μm and the repetition rate was 200kHz. T. Südmeyer *et al.* developed an OPG system based on a high repetition rate (35MHz) Yb:YAG laser; the system was capable of producing higher average power pulses in tens of nanojoule at around 1.5 μm [Tsü01]. In order to obtain higher pulse energies, the pulses generated by an OPG may be amplified in an OPA configuration. M. Marangoni *et al.* and J. Krauth *et al.* described the parametric process underlying the OPA architecture. The former used identical crystals for the generation and amplification of the pulses whereas the latter used a tapered fibre to create a super continuum that was then amplified in a crystal [Mma07][Jkr13].

In the present work we present OPG and OPA set-ups based on periodically poled magnesium-doped lithium-niobate crystals (PPMLN, Mg~5%), pumped by a diode-pump solid state laser (DPSSL) system emitting at a central wavelength of 1030nm. We first present two different OPG set-ups that use PPLMN crystals with different grating structures. One of these crystals is then incorporated in an OPA configuration, which permits us to obtain pulse energies in the microjoule range which to our knowledge is the maximum pulse energy so far obtained within this wavelength range with comparable systems. We have also investigated the capacity to control the emission spectrum by spectral filtering the OPG output signal before amplification. At the end we have also studied the effect of an unstable super continuum on

the overall performance and efficiency of the OPA and present results of surgical experiments that have been obtained on pathological human cornea.

4.3 Optical Parametric Generator (OPG)

4.3.1 Experimental Setup

The schematic of the experimental setup is shown in Figure 4.1. For the experiments presented here we used a commercial laser system consisting of an oscillator and a regenerative amplifier based on diode-pumped ytterbium-doped crystals (s-pulse HP, Amplitude Systèmes, Pessac, France). The system is capable of delivering pulse energies of up to 1mJ (1-2kHz) at 1030 nm with a spectral width of about 7nm having a TEM00 spatial profile with $M^2_x=1.9$, $M^2_y= 1.1$. The repetition rate is adjustable from 1 to 100 kHz with pulse durations of 730fs at 10 kHz. For all the experiments presented here we have selected a repetition rate of 10kHz, at which pulse energies of up to 400 μ J may be obtained.

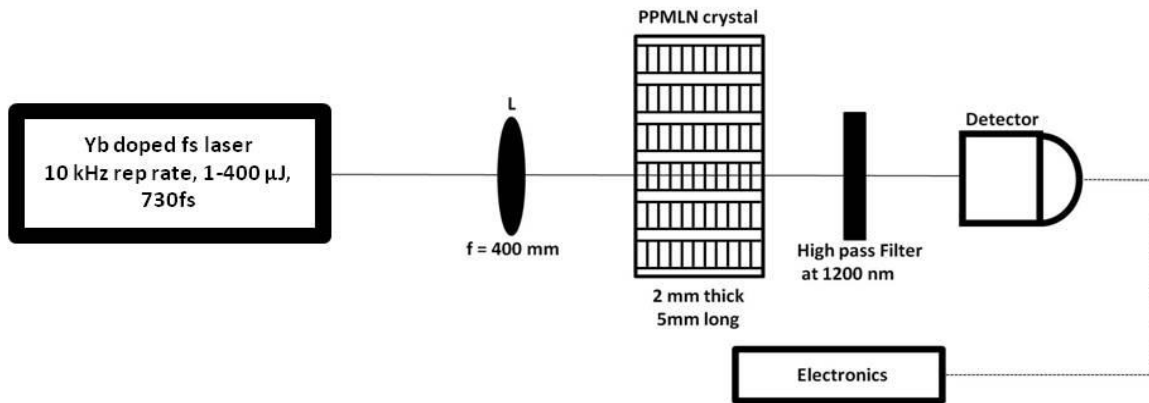


Fig. 4. 1: Schematic of the OPG set-up: The lens *L* focuses the pump beam inside the crystal. The generated signal passed through the high pass filter followed by the detector.

For the OPG set-up (Fig.4.1), two periodically poled magnesium doped lithium niobate crystals (PPMLN, Mg~5%) were used (HC-Photonics, Hsinchu, Taiwan). Each crystal contains six grating structures with different grating constants, for which the manufacturer values are shown in table 4.1.

Crystal	Grating 1	Grating 2	Grating 3	Grating 4	Grating 5	Grating 6
Crystal A	29.37 μ m	29.60 μ m	29.86 μ m	30.13 μ m	30.46 μ m	30.86 μ m
Crystal B	24.00 μ m	24.50 μ m	25.00 μ m	25.50 μ m	26.00 μ m	26.50 μ m

Table 4. 1: Gratings that are present on crystal A and B.

For each grating, the clear aperture is $2 \times 2 \text{ mm}^2$ for an overall crystal length of 5 mm ($\pm 0.2 \text{ mm}$) and a thickness of 2mm ($\pm 0.05\text{mm}$). The input and output facet were polished and coated with $R < 1\%$ (1500-1800nm) for crystal A and $R < 5\%$ (1200-1450nm) for crystal B. The crystals were mounted onto an electrical oven which permits the adjustment and the stabilisation of the crystal temperature in a range from 60°C to 160°C . The pump laser emits a collimated beam with a diameter of 2.9 mm at $1/e^2$. The beam was focused into the crystal by an chromatic doublet lens of 400mm (AC254-400-C-ML, Thorlabs, Newton, USA; L in the schematic) in order to obtain a nominal beam waist of $200\mu\text{m}$. The output beams were then spectrally filtered by a high pass filter at 1200nm (FEL1200, Thorlabs, Newton, USA) in order to remove the residual pump beam and light generated by second harmonic generation at 515 nm. According to the data provided by manufacturer the band pass filter has high transmission (above 50%) from 1200-2600 nm. The output beams were characterised using a power meter (PM100USB, Thorlabs, Newton, USA) or a spectrometer (AvaSpec-NIR256, Avantes, Apeldoorn, Netherlands).

4.3.2. Results and Discussion

Figure 4.2 shows the conversion efficiencies for crystal A and B. We have measured the combined pulse energies of signal and idler after the high pass filter. The linear fits to the obtained results allowed us to determine the threshold pump energies and the conversion efficiency. Thresholds lie in the low microjoule range for the two gratings on crystal A and B. Along with the measured data, we have also calculated and presented the energies of signal and idler by considering the transparency of the high pass filter. The transmission of the high pass filter was around 85% for the entire signal wavelengths produce by the four gratings that were used during this measurement, 39% for the idler produced by grating 30.46 and zero for other gratings. The corrected values that take into account the transmission of the high pass filter are also mentioned in the figure 4.2 (a-b). Table 4.2 summarized the conversion efficiency for measured and corrected values, signal and idler produce by each grating and transparency value of the high pass filter at given signal and idler wavelengths.(The transparency of the high pass filter from 200-5000nm is presented in Appendix 3).

	30.13 μm	30.46 μm	26.5 μm	26.0 μm
Measured efficiency (%)	17 (± 0.6)	17 (± 0.2)	15 (± 1.1)	17 (± 2.7)
Corrected efficiency (%)	29 (± 1)	25 (± 0.3)	22 (± 1)	25 (± 4)
Signal/idler values (nm)	1575/2975	1650/2740	1335/4505	1310/4815
Transparency of high pass filter at each signal and idler wavelength (%)	86/0	85/39	88/0	87/0

Table 4. 2: Conversion efficiencies, the value of signal and idler generated by each grating and transparency of high pass filter for each signal and idler values.

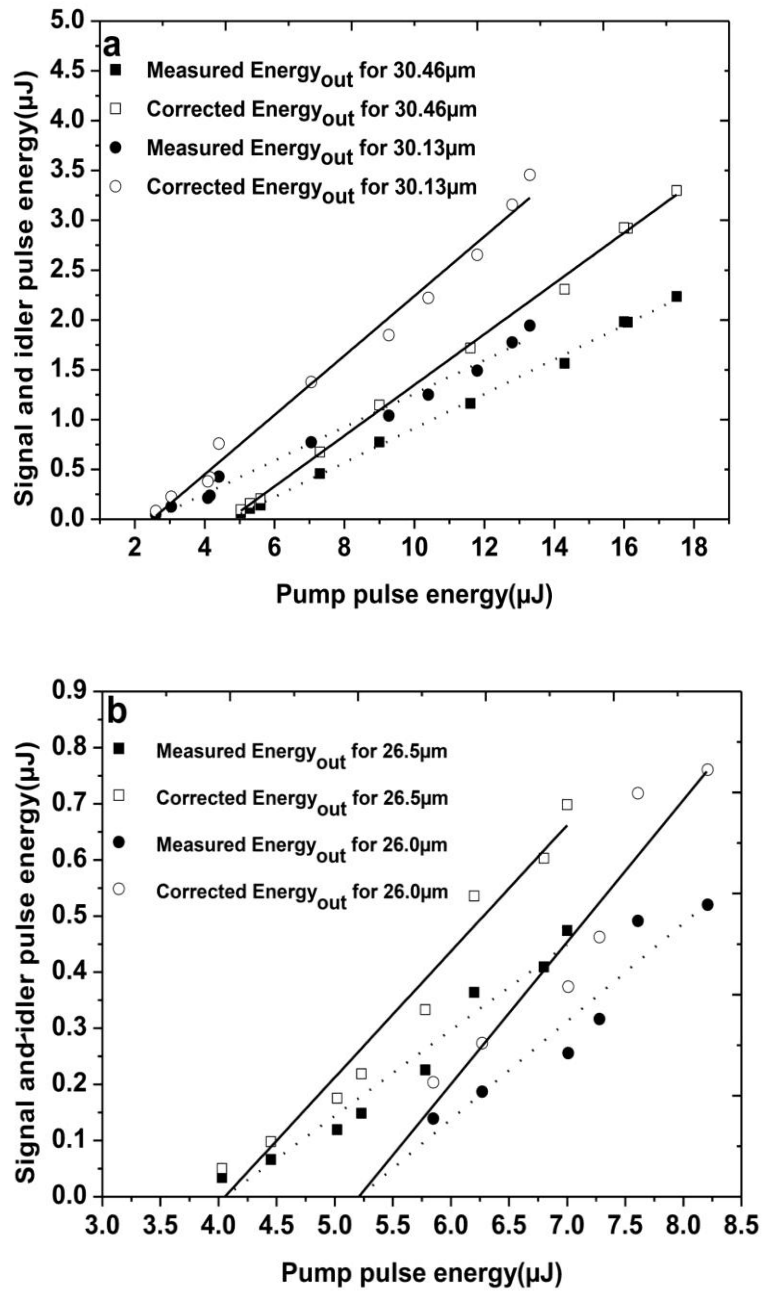


Fig. 4. 2: Signal and idler pulse energy versus input energy measured and corrected for two different gratings on each crystal: crystal A (a), crystal B (b).

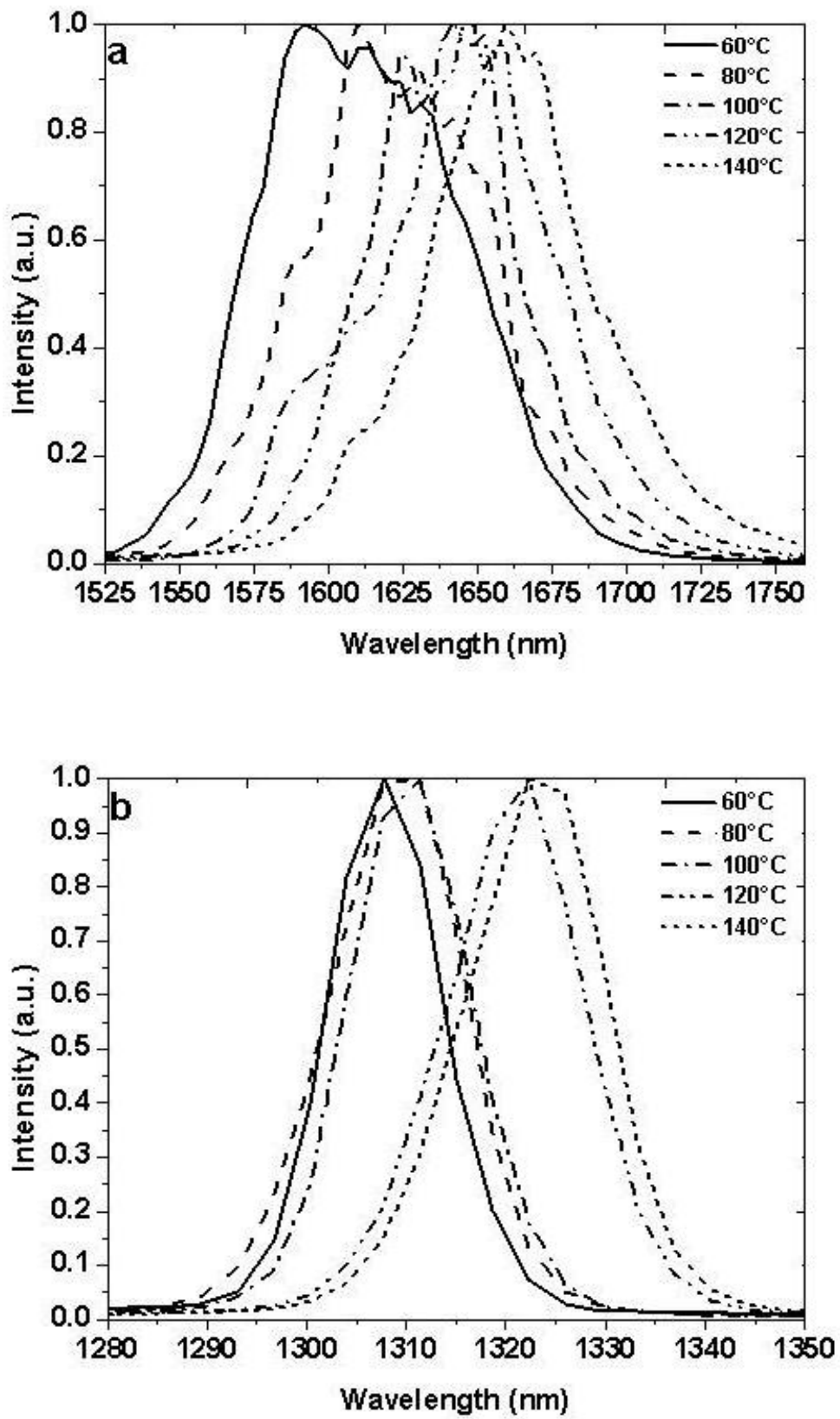


Fig. 4. 3 (a) - (b): OPG spectrum measured for constant grating at different temperature: 30.46 μm for crystal A (a) 26 μm for crystal B (b).

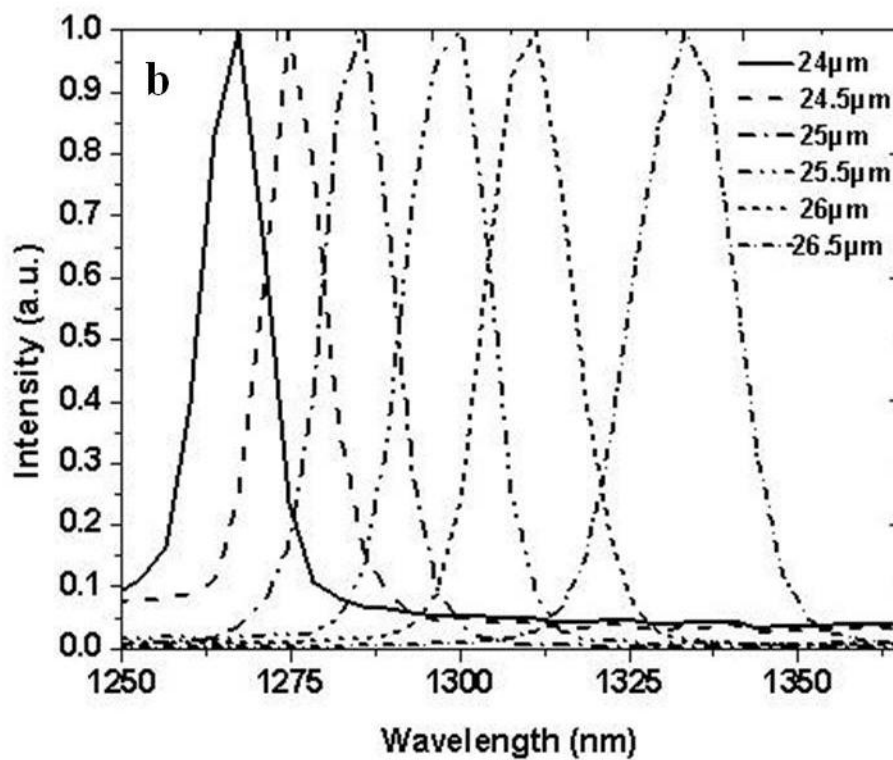
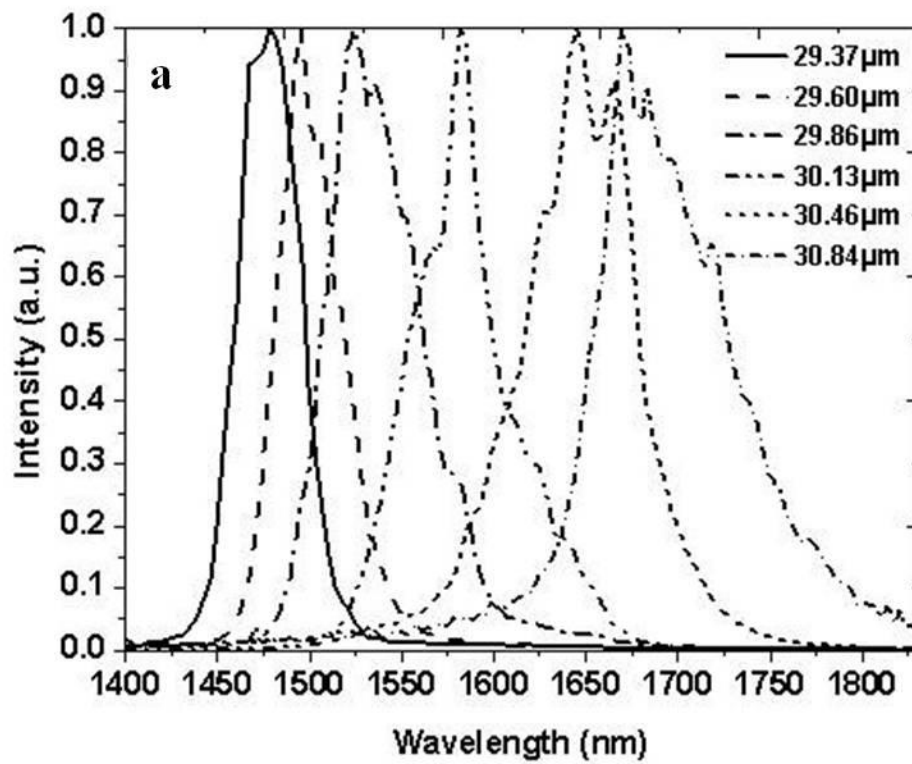


Fig. 4. 4 (a) - (b): OPG spectrum measured for different gratings at constant temperature of 100°C for crystal A (a) and B (b).

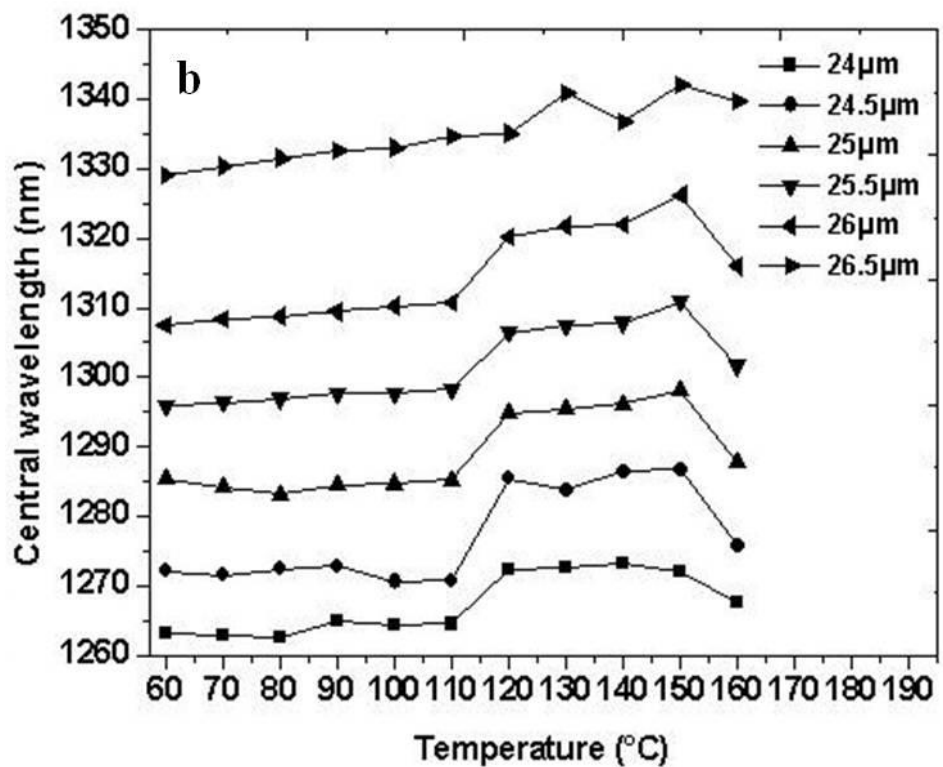
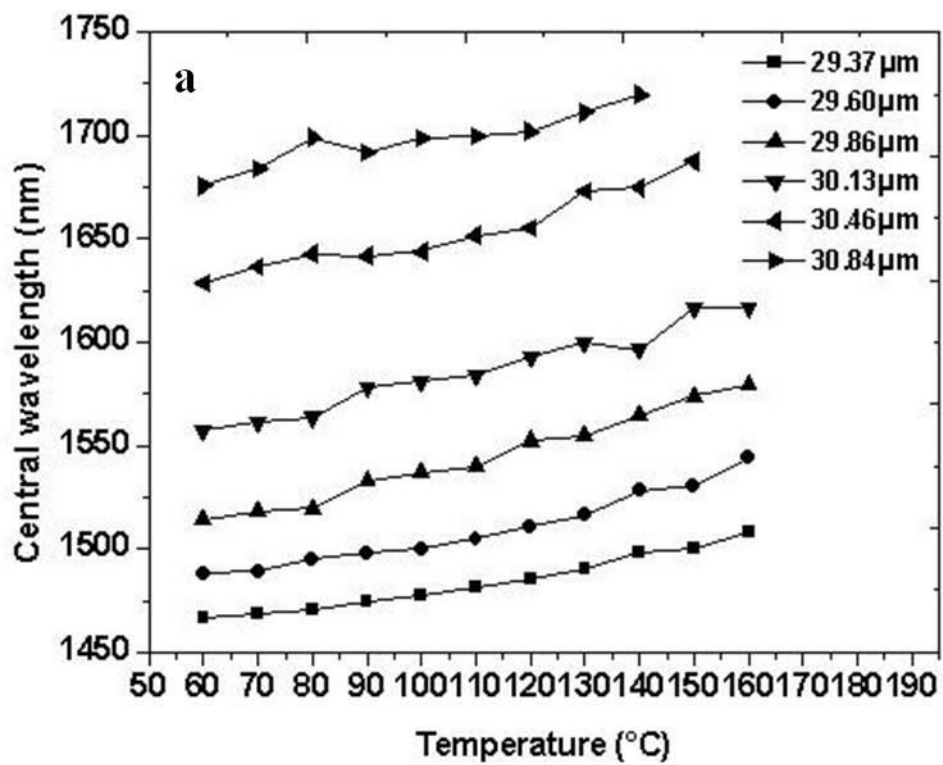


Fig. 4. 5 (a) - (b): Temperature tuning curves measured for different gratings: crystal A (29.37, 29.60, 29.86, 30.13, 30.46, 30.84 μm)(a) crystal B (24, 24.5, 25, 25.5, 26, 26.5 μm)(b).

Using an optical spectrometer we measured the signal spectrum for varying temperatures for constant grating period (30.46 μm for crystal A and 26 μm for crystal B) Fig.4.3 (a)-(b), and for different crystal grating periods at constant temperature (100°C for both crystals) Fig.4.4 (a)-(b). The results show that in comparison to crystal A, the output wavelengths obtained from crystal B do not depend much upon the temperature of the crystal or the grating. Finally, we complete the data set presented in Figure 4.3-4.4 for all the gratings at different temperatures. The central wavelength was obtained by finding the centroid of the measured spectra in order to avoid errors that might arise due to curve fitting some pre-defined function to the spectra Figure 4.5 (a)-(b). Figure 4.5 (b) shows an abrupt increase in wavelength at 110°C and a decrease at 150°C, this can be attributed to the fact that the corresponding idler (around 5000 nm) interacts with the absorption band of LiNbO₃. A likely explanation for the observed artefacts is that in this particular temperature range an additional thermal contribution by the absorption of idler creates additional non-linear effects resulting in the increase (110°C) and decrease (150°C) in wavelength.

4.4 Optical Parametric Amplification (OPA)

4.4.1 Experimental Setup

The experimental setup for the OPA is shown in Fig. 4.6. A part of the pump beam (typically 5 or 10%) is retrieved by a beam splitting cube in order to pump the crystal PPMLN1. The output beam of PPMLN1 passes through a high pass filter (FEL1200, Thorlabs, Newton, USA) in order to eliminate the pump beam and second harmonic. In the first stage the idler was removed from the signal beam path by using two dichroic mirrors $M2$ and $M3$. For some experiments a band pass filter (NB-1650-050, Spectrogon, Sweden) with a transmission of around 80% at 1650 nm was used which can be positioned between the amplification stages. (the purpose of this band pass filter is to control the spectral bandwidth, see below). The output signal of PPMLN1 and the remaining pump beam (carrying between 90 or 95% of the initial pump power) are then focused into the second crystal (PPMLN2). The delay line permits to superpose the signal and pump pulse temporally.

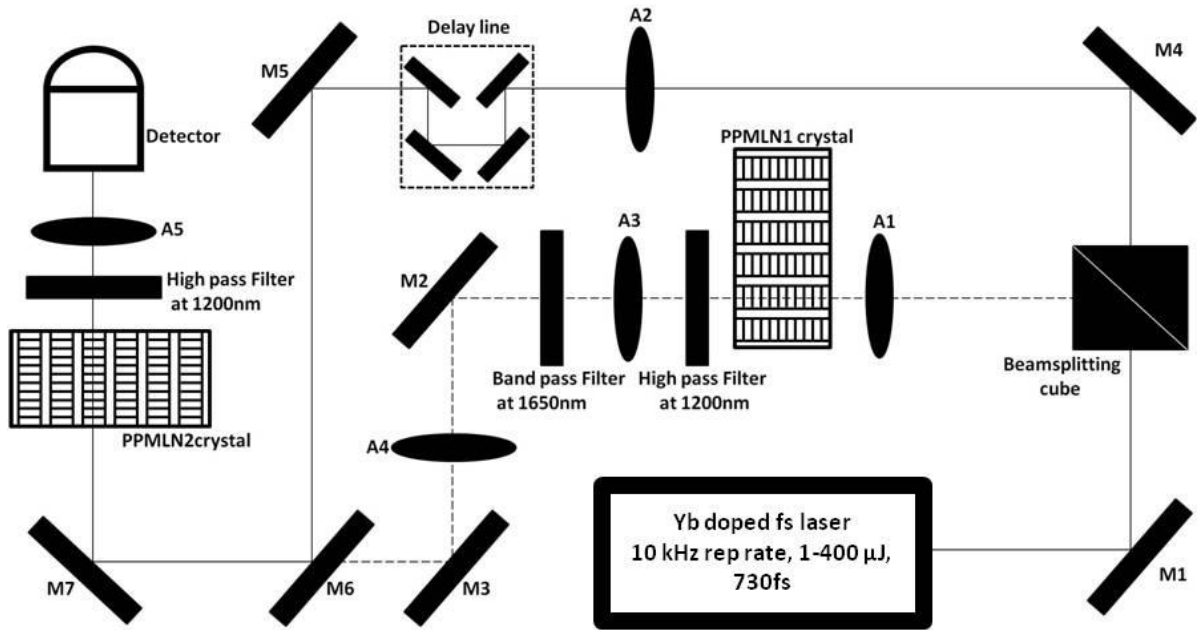


Fig. 4. 6: Schematic of the OPA set-up: Stage1 contains M1, beam splitting cube, A1, nonlinear crystal (PPMLN1), high pass filter, A3, bandpass filter, M2, A4 and M3. Stage2 contains M1, beam splitting cube, M4, A2, delay line, M5, M6, M7, nonlinear crystal (PPMLN2), where M1- M7 are mirrors and A1, A2, A4 are focusing and A3, A5 are recollimation lens. M2, M3, M6 are dichroic mirrors and M2 M3 are highly reflective at signal frequency.

4.4.2 Results and Discussion

In order to set up an OPA system, at least two crystals capable of generating an identical wavelength are needed. We have investigated the use of crystal A in an OPA configuration as it permits to generate the wavelength which is of particular interest for corneal surgery (1650nm). (For the generation of the wavelength of 1300 nm, potentially useful for the surgery of the crystalline lens, a system based on crystal B may be conceived). In order to study the wavelength conversion at this particular wavelength (1650 nm), the output of PPMLN1 was filtered using the aforementioned band pass filter centred at 1650 nm. For all cases we measured the total energy of both signal and idler. All three possible configurations are presented in figure 4.7. In the first configuration we use PPMLN2 as an OPG as presented above (squares). The second configuration corresponds to the OPA without spectral filtering; the signal that was produced by PPMLN1 was fed into the PPMLN2 which amplifies the signal of PPMLN1. The combined signal and idler energies were measured and found to increase by a factor of thirteen (presented as triangles). Spectral filtering after PPMLN1 using the band pass filter results in slightly lower conversion efficiency (configuration 3, circles). We deter-

mined slope efficiencies for our system which are low compared to those plotted in figure 4.2(a). The reason for this is the long focal length ($\geq 1000\text{mm}$) of the lens used for this experiment compared to the value of 400mm used for the experiments yielding the results presented in figure 4.2(a).

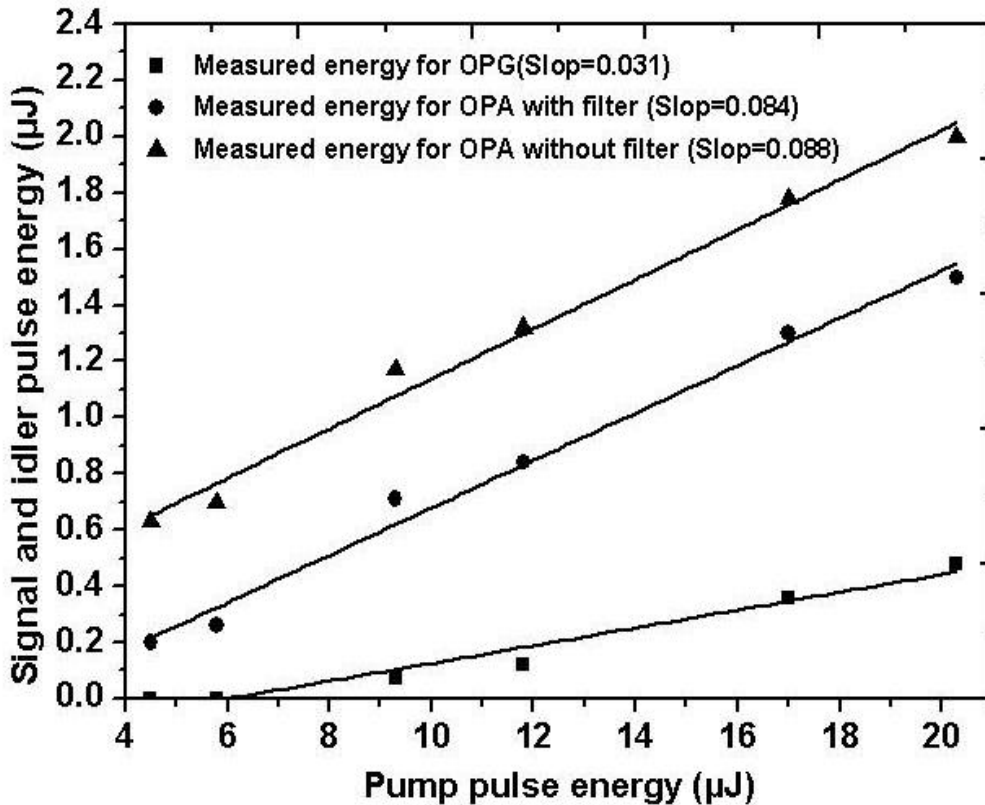


Fig. 4. 7: Comparison of slopes when different configurations were considered: OPG (square), OPA with band pass filter (circle) and OPA without band pass filter (triangle) data points were obtained for crystal A.

Fig. 4.8a shows the signal spectra obtained from the PPMLN1 crystal with and without the bandpass filter at 1650nm . In comparison to the OPG without the bandpass filter, the obtained spectrum is narrower as it corresponds to the transmission spectrum of the filter. The spectrum of PPMLN2 was then studied for three different configurations. In the first configuration we block the signal from the PPMLN1 which then produces the output spectrum shown in a solid line (figure 4.8b). We then focus the PPMLN1 signal without bandpass into the PPMLN2. For this configuration we observe amplification within spectral ranges outside of the spectral previously obtained from PPMLN1. The use of the bandpass filter after the PPMLN1 suppresses those side lobes.

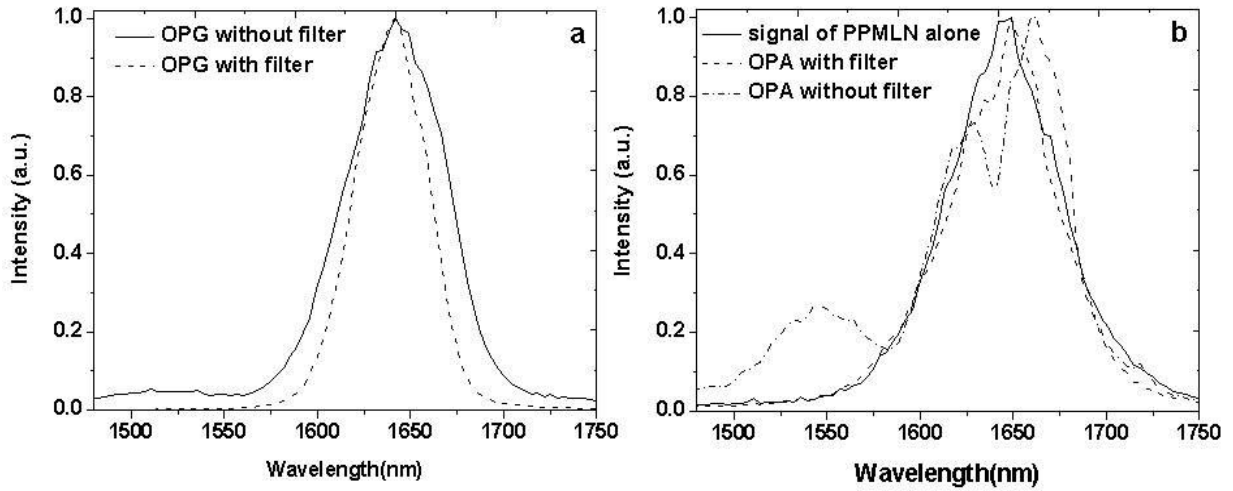


Fig. 4. 8: Spectra obtained in different OPG and OPA configurations. OPG with and without band pass filter (a), OPA with and without band pass filter plus the spectrum of PPMLN2 without seed signal from PPMLN1 (b).

M^2 values and spatial beam profiles were measured by using P8 BeamScope, DataRay, Bella Vista, United States and TeraCam, Mérignac, France (Fig. 4.9 and table 4.3). First we observe the spatial beam profiles of the beam for all cases (Fig.4.9). From this data we can say that the spatial profiles for all the beams are regular. The profile plotted in figure 8c has some apparent distortion at wings which may be attributed to average power levels which are below the sensitivity of the camera. The spatial profiles in both OPA configurations are not identical; the value of M^2 is different (table 4.3). The possible reason for this might be the additional amplification of different wavelengths when the entire spectrum of the PPMLN1 signal passes through the PPMLN2 crystal in comparison to the case when only a narrow part of the spectrum (limited by the band pass filter) is amplified.

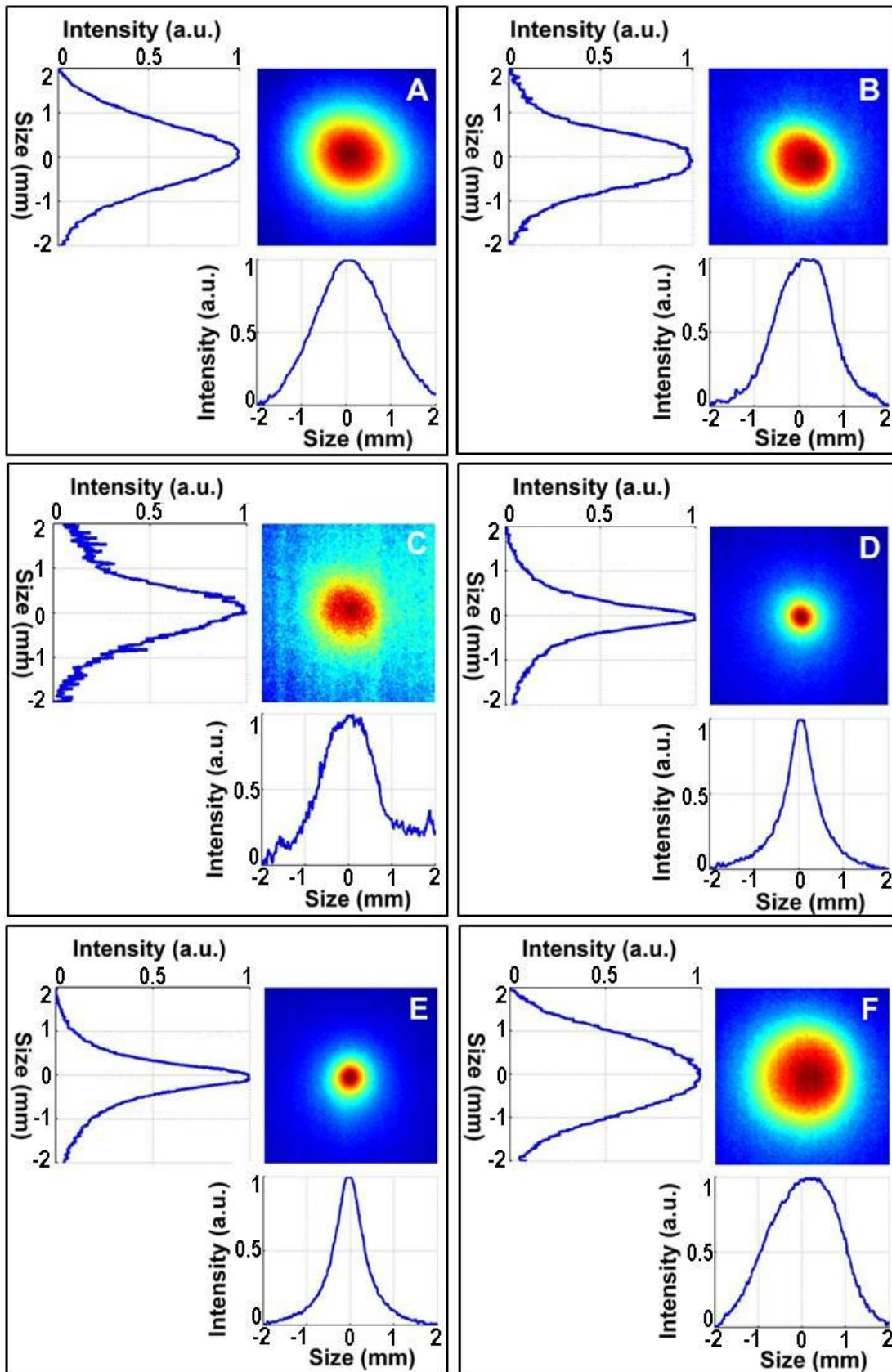


Fig. 4. 9: Spatial profiles (A) pump, (B) seed without filter, (C) seed with filter, (D) OPA without filter, (E) OPA with filter, (F) PPMLN2 (OPG and OPA signals were measured at a distance of 400 mm away from the crystal).

	PPMLN1	PPMLN1 with filter	OPA without filter	OPA with filter	PPMLN2	Pump
M^2_x	3.6	-	6.6	3.4	-	1.9
M^2_y	3.7	-	4.3	3.8	-	1.1
Gain	1.25%	0.12%	n.a.	n.a.	1.29%	n.a.
Amplifier Gain	n.a.	n.a.	8.92%	1.40%	n.a.	n.a.

Table 4. 3: Characteristics of the generated signal from OPG and OPA.

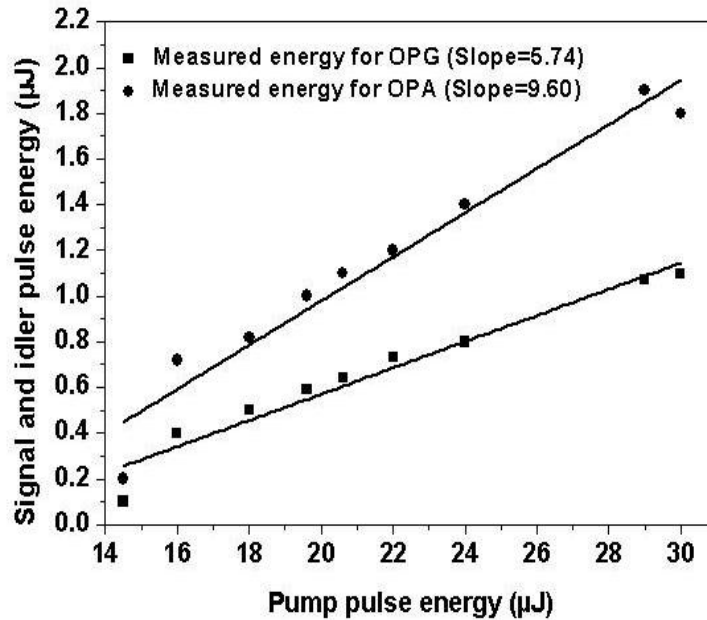


Fig. 4. 10: Comparison of the slopes for OPG (square) and amplification due to continuum generation (circle).

Recently, the use of tapered fibres has been demonstrated as the replacement of the first crystal [Jkr13]. In this configuration the broadband continuum created by the tapered fibre is feed into the amplifier crystal in order to obtain amplified signal. We performed a similar experiment and evaluated the performance and efficiency of the OPA system when PPMLN1 is replaced by a substrate of silicate glass (Fig. 4.10) in order to generate a broadband continuum. This study has been performed in two steps. First the conversion efficiency was evaluated by measuring the total output energy (signal + idler) without feeding any signal from the continuum; in this configuration the second crystal acted as an OPG. In the second part we focused the pump beam inside the silicate glass in order to generate a broadband continuum.

A bandpass filter was used to filter the signal before recombination with the pump beam inside PPMLN2. We measured the output energy (signal+idler) after the PPMLN2 crystal with the silicate glass; the results are presented as in Fig.4.10. In this configuration we observed amplification by a factor of about 2. However, the continuum was not sufficiently stable near the generation threshold and the generated signal was therefore fluctuating.

4.5 Conclusion

- We have presented results obtained from optical parametric generation and amplification based on periodically poled lithium niobate crystals.
- In optical parametric generation we obtained energy of the order of several microjoules which may at least be doubled for optical parametric amplification.
- The spectrum from OPA can be controlled by using a bandpass filter after the first stage. In our experiment it eliminates side lobes that were present before. However, a compromise needs to be made for power amplification.
- An OPA configuration with a continuum comparison generated in silicate glass in the first arm and amplified PPMLN crystal has also been studied, but was found to be unstable in its output.
- As a perspective, the achievable energy from an optical parametric amplifier can be increased further by using a stretcher and a compressor similar to chirped pulse amplification (CPA). This geometry is usually called as optical parametric chirped pulse amplification (OPCPA). By using this geometry the energy is increase by avoiding undesirable effects such as damage threshold of the crystal and group velocity dispersion (GVD) (Fig.4.11).

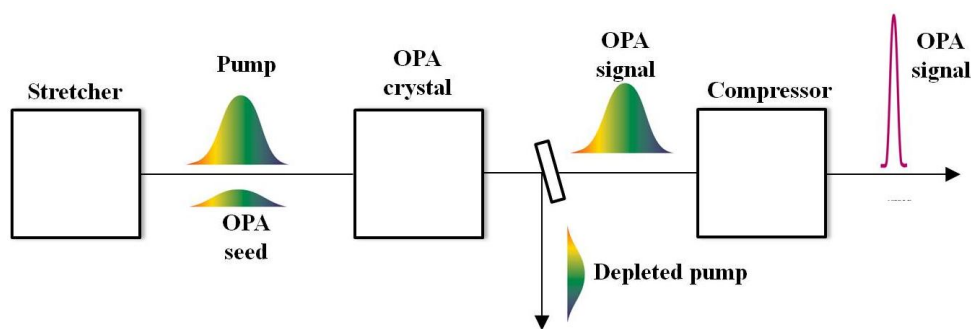


Fig. 4. 11: Schematic of Optical parametric chirped pulse amplification (OPCPA).

Chapter V

Cell viability in the endothelium of porcine cornea exposed to ultrashort laser pulses at 1030 nm.³

5.1 Abstract

We present a study on the viability of endothelial cells of the porcine cornea exposed to ultrashort laser pulses at a wavelength of 1030 nm. Two series of experiments were performed while varying pulse energy and distance of the impacts to the endothelium. For all combination of parameters we estimated the amplitude of the shock wave generated by the laser-tissue-interaction process which is likely to be the cause for cell deterioration and death. Our results may help to define safe conditions for the use of ultrashort pulse lasers for the preparation of endothelial grafts.

5.2 Introduction

The human corneal endothelium is a monolayer of cells located at the posterior surface of the cornea, whose thickness of about 5µm represents only about 1 % of the total corneal thickness. The endothelium's primary function is to regulate and stabilise the hydration of the cornea by continuously ensuring water and ion movements between the stroma and the aqueous humour in the anterior chamber. Maintaining a constant hydration level is crucial for the maintenance of corneal transparency. Human endothelial cells do not proliferate or regenerate in case of injury or cell death. The average endothelial cell density in healthy human cornea is about ~ 2500-3500 cells/mm² [Pip11]. In the case of the death of individual endothelial cells, other cells extend their surface and cover the surface of the lost cells. Endothelial dysfunction, such as Fuchs' endothelial dystrophy or endothelial failure secondary to pseudophakic bullous keratopathy [Aly04], can cause low visual acuity or blindness as endothelial pumping abilities are no longer sufficient to avoid stromal swelling, corneal oedema and loss of transparency. In

³ This chapter has been adapted from a manuscript which is currently in preparation for submission. Zacaria Essaïdi, Caroline Crotti, Fatima Alahyane, Karsten Plamann, Laura Kowalczuk and Marie-Claire Schanne-Klein contributed to the work. We thank Gilles Thuret, Philippe Gain and co-workers from the research unit *Biologie, Ingénierie et Imagerie de la Greffe de Cornée*, Saint-Étienne university, France, for help with the cell staining protocol.

many of these cases, the only solution is surgical, with total or partial corneal grafting (keratoplasty) using donor tissue. Different kinds of keratoplasty can be performed surgically: total penetrating keratoplasty (a full thickness corneal transplant) or partial grafts like anterior lamellar keratoplasty (transplantation of the anterior part of the stroma, only in cases where the patient's endothelium is still operational) or endothelial keratoplasty (transplantation only of Descemet's membrane and the endothelium). These partial surgical routines (that address only the anterior or posterior part of the cornea) are performed increasingly often because of their benefits with respect to visual acuity and graft rejection [All07] [Grm06]. Among these techniques, the most frequently used are Deep Anterior Lamellar Keratoplasty (DALK), Deep Lamellar Endothelial Keratoplasty (DLEK), Posterior Lamellar Keratoplasty (PLK), Descemet Stripping Endothelial Keratoplasty (DSEK or DSAEK) and Descemet's Membrane Endothelial Keratoplasty (DMEK) [Mpa13]. These grafting procedures can be performed either manually with a microkeratome or by using ultrashort pulse laser systems [Osa06]. These laser pulses interact with the tissue only within a strongly confined region and can perform precise cuts inside the volume of the tissue. Originally developed for LASIK procedures, femtosecond lasers are nowadays also used for corneal grafting and, more recently, for some steps in cataract surgery (incision, capsulorhexis, lens fragmentation) [Hks09][Pla10]. One of the main factors concerning the success of the procedure is the viability of the endothelial cells after the operation. Endothelial cell density changes after a corneal transplant have been widely studied [Wmb01], however, to the best of our knowledge, data concerning the correlation between cell loss and pulse energy or depth of incision is still lacking. In this paper, we report on experiments assessing the viability of the endothelial cells depending on two different variables (distance of the incision to the endothelium and pulse energy), with lamellar incisions (parallel to the corneal surface) on porcine corneas. The viability of the cells was assessed by using fluorescent markers and analysing the corneas under a fluorescence microscope.

5.3 Materials and Methods

The experiments presented here were performed on porcine corneas. Porcine eyes were obtained under permission from a local slaughterhouse. The eyes were retrieved from young pigs with an average age of about 6 months. The eyes were transported to our site within 4 hours and remained stored at 4°C. A commercial laser system emitting ultrashort pulses at a central wavelength of 1030 nm with a spectral bandwidth of about 7.8 nm having spatial pro-

file close to TEM_{00} and a pulse duration of about 730fs was used as a source (S-pulse HP, Amplitude Systèmes, Pessac, France, pulse durations measured by Pulse check, APE, Berlin, Germany). The repetition rate is adjustable from 1 to 100 kHz; a rate of 10 kHz was used for the experiments presented here (Fig.5.1).

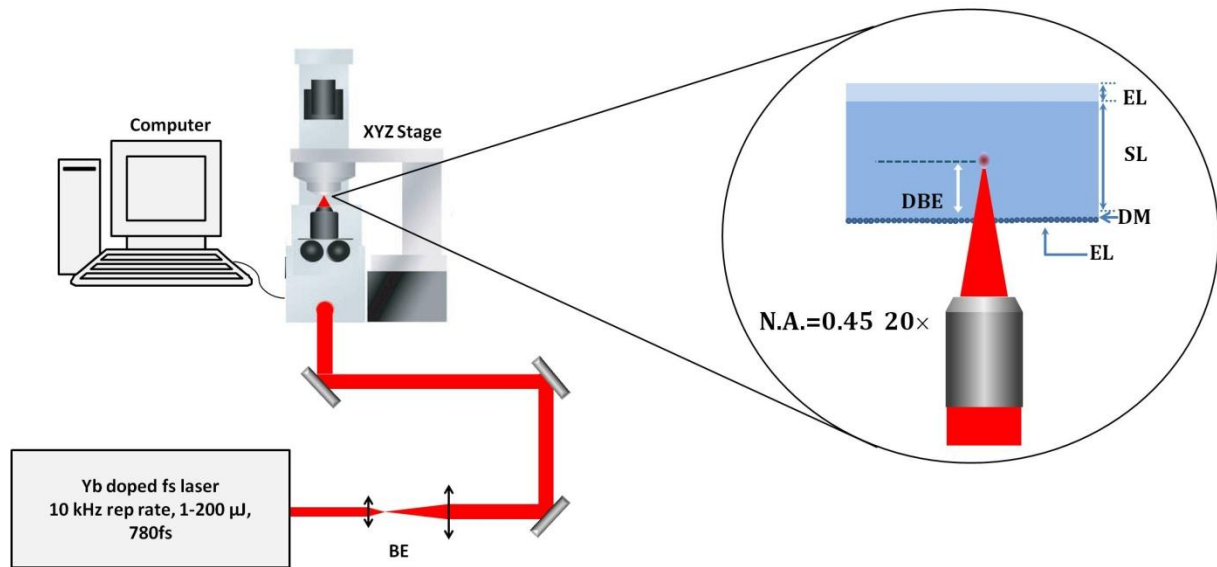


Fig. 5. 1: Schematic of the experimental setup: BE= beam expander, EL= epithelial layer, S= stroma , DM= Descemet's membrane, E= endothelium, D= distance between laser spot and endothelium cells. M1-M3 are mirrors.

After extracting the cornea from the porcine eye, the thickness of each cornea was recorded by using an ultrasound pachymeter (Tomey, Nagoya, Japan). For the experiments performed to validate the staining protocol, the cornea was sandwiched between the two glass slips (Menzel Gläser, Saarbrücken, Germany). The laser beam was focused into the porcine cornea from the posterior side by using a microscope objective with a numerical aperture of 0.45 (LCPLN-IR Olympus, Tokyo, Japan) which is optimised for the near infrared spectral range (Fig.5.1). The XYZ step motor module was controlled by a personal computer using the LabView programming language (National Instruments, Austin, USA). Routines were programmed as to produce planar (“lamellar”) cuts inside the volume of cornea with a spot-to-spot distance of 3 μm . In total, twenty corneas were treated. The Hoechst/ethidium homodimer/calcein-AM staining described in Piparelli *et al.* [Pip11] was used to evaluate cell viability. The corneas, placed endothelial side up in a sterile petri dish, were incubated for 45 minutes at +31 C with 125 μL ethidium homodimer-1 (4 μM) and calcein-AM (4 μM) in phosphate-buffered saline (PBS) (live/dead cells staining kit II, Promo Cell, Heidelberg, Germany). After incubation, the cornea was washed in the saline buffer for 3 min. The cor-

neas were then incubated for 15 minutes at +31 C with 125 μ L Hoechst 33342 solution (4 μ M) (Sigma-Aldrich, Saint Louis, United States). After gentle rinsing for 3 min, the corneas were flat mounted between the two glass slips (Menzel Gläser, Saarbrücken, Germany) and then observed under a fluorescence microscope (Nikon AZ-100, Tokyo, Japan). Live cells were observed using the detection of the hydrolyzed calcein emission in green. The peak excitation wavelength is 495 nm; it emits green fluorescent light with a peak of 520 nm. The nuclei of the dead cells were labelled with ethidium homodimer-1. The peak excitation wavelength is 528 nm; it emits red fluorescent light with a peak of 617 nm. Finally, all nuclei were stained with Hoechst 33342 which is a vital nucleic acid dye. It is excited by ultraviolet light at around 350 nm and emits blue/cyan fluorescent light with a peak of 461 nm [Pip11].

The image obtained on an untreated control cornea is shown in figure 5.2. Panel A shows fluorescence images at different magnifications. The green colour channel represents live cells, the red channel represents dead cells, and the blue channel represents the nuclei of all the cells which are alive, dead, and dying without metabolic activity. The regions devoid of endothelial cells appear as black in Panel A. Panel B-D show the separated green, red and blue channels. Going from lower to higher magnification, the green and red channels show that a small fraction of the cells within the folds of the endothelium have died. Panel D shows the nuclei of all cells and serves as a control measurement in order to avoid artifacts. As expected, the nuclei of the cells both in the red and green marked regions are marked blue. However it was found that that in the regions of the live cells marked green, the blue fluorescent intensity value of these cells is systematically about three times lower than the blue fluorescent signal of the dying and dead cells (Panel E).

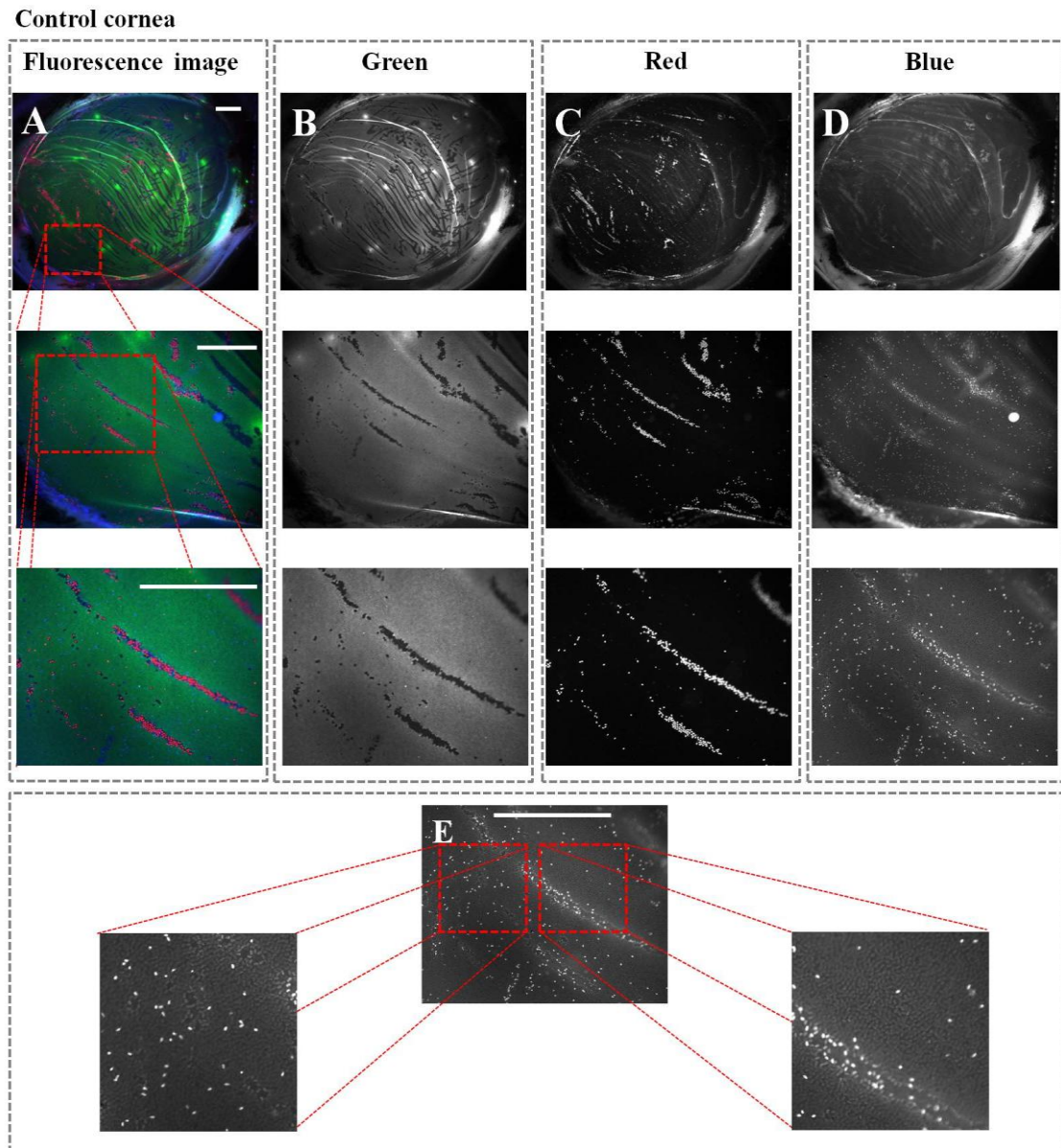


Fig. 5. 2: Control cornea without any incision/s observed by the microscope (Nikon AZ-100) (A) using the three different magnifications $x2$, $x4$ and $x8$ (first, second, and third rows). Green (living cells) (B), Red (dead cells) (C), Blue (nuclei of all the endothelial cells)(D). Nuclei visibility with respect to different magnification(E). Scale bar= $1500\mu\text{m}$, where the black part in the fluorescence image shows absence of endothelial cells.

Figure 5.3 represent a typical image obtained for a cornea in which two lamellar incisions of $1000 \times 1000 \mu\text{m}^2$ were made. In addition to the effects described above for the control cornea, the cell viability is visibly affected at the incision area.

Our observations concerning the experiments represented in figure 5.2 and 5.3 may be summarised as follows:

-
- The green, red and blue colour channels represent live cells, dead cells and the nuclei of all cells.
 - The black regions in the fluorescence images represent absence of endothelial cells.
 - The fluorescence intensity of the nuclei of dead or dying cells is systematically about three times higher than the live area in the control cornea and in the cornea which has undergone laser treatment.
 - The reasons for this are not known with certainty. However, it may be assumed that an increase in the Hoechst fluorescence intensity is linked with the cell damage due to reasons such as mechanical force, laser or extreme pH [Gilles Thuret and Zhiguo He, Saint-Étienne University, France, private communication]. The DNA of the cells undergoing necrosis is then more strongly exposed to the Hoechst fluorescence marking than the live cells and therefore exhibit increased fluorescence intensity [Per].
 - The small amount of dead cells in the folds of the untreated control cornea may be attributed to the flat mounting process between the two glass surfaces (Figure 5.2 Panel A). This can also affect the viability of the treated area which can decrease the validity of our results. As our experiments do not require a flat corneal surface over the entire cornea, we subsequently refrained from flat mounting the corneas and observed the endothelium directly

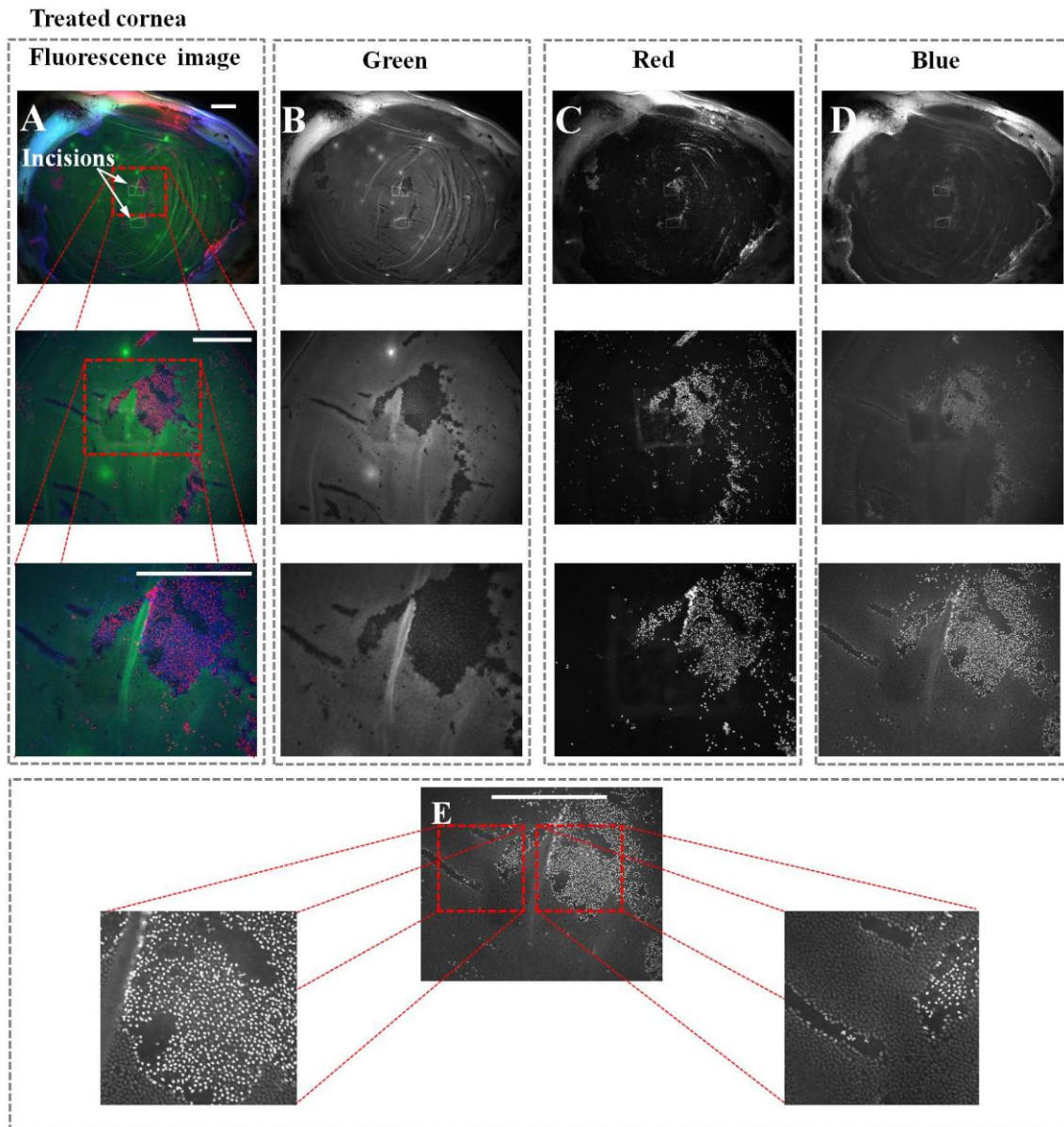


Fig. 5. 3: Treated cornea with laser pulses that makes a lamellar incision of $1000 \times 1000 \mu\text{m}^2$ inside the volume of cornea. Fluorescence image observed by the microscope (Nikon AZ-100) (A), Green (living cells) (B), Red (dead cells) (C), Blue (nuclei of all the endothelial cells)(D). Nuclei visibility with respect to different magnification (E). Scale bar= $1500 \mu\text{m}$, where the black part in the fluorescence image shows absence of endothelial cells.

For the surgical experiments, after extracting the cornea from the porcine eye it is placed on the home made artificial chamber that was filled with BSS (balanced salt solution). A standard microscope cover slip with a thickness of $170 \mu\text{m}$ (Menzel Gläser, Saarbrücken, Germany) was then placed on the surface of the cornea in order to obtain a flat surface. By using the same experimental setup, we focused the laser beam into the porcine cornea from the anterior side by using a microscope objective (LCPLN-IR Olympus, Tokyo, Japan) induc-

ing lamellar incisions of $500 \times 2000 \mu\text{m}^2$ (Fig.5.4). The corneas were divided into three groups. A control group of 2 corneas was left untreated by the laser, a second group of 13 corneas was treated with pulses of constant energy, and a third group of 11 corneas underwent the laser treatment at constant depth while varying the laser pulse energy. The corneas were stained and observed directly under a fluorescence microscope without flat mount. Figure 5.5 represents the images that were obtained for control cornea. In comparison to the control cornea that was obtained in figure 5.2 the fluorescence image obtained using this method is green everywhere with very few dead cells.

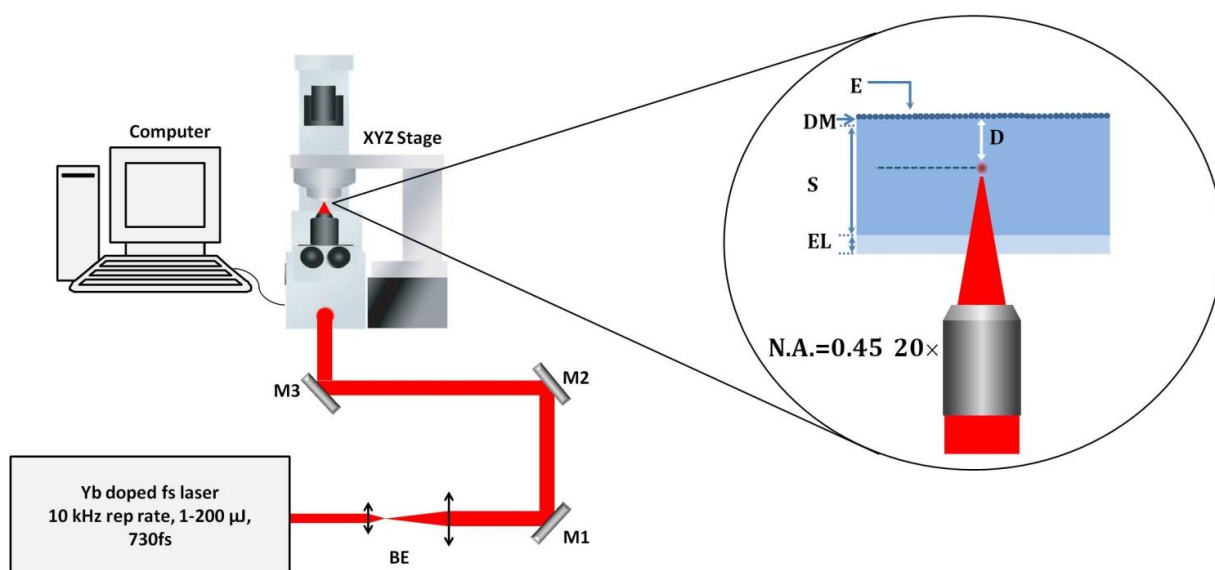


Fig. 5. 4: Schematic of the experimental setup: BE= beam expander, EL= epithelial layer, S= stroma , DM= Descemet's membrane, E= endothelium, D= distance between laser spot and endothelium cells. M1-M3 are mirrors.

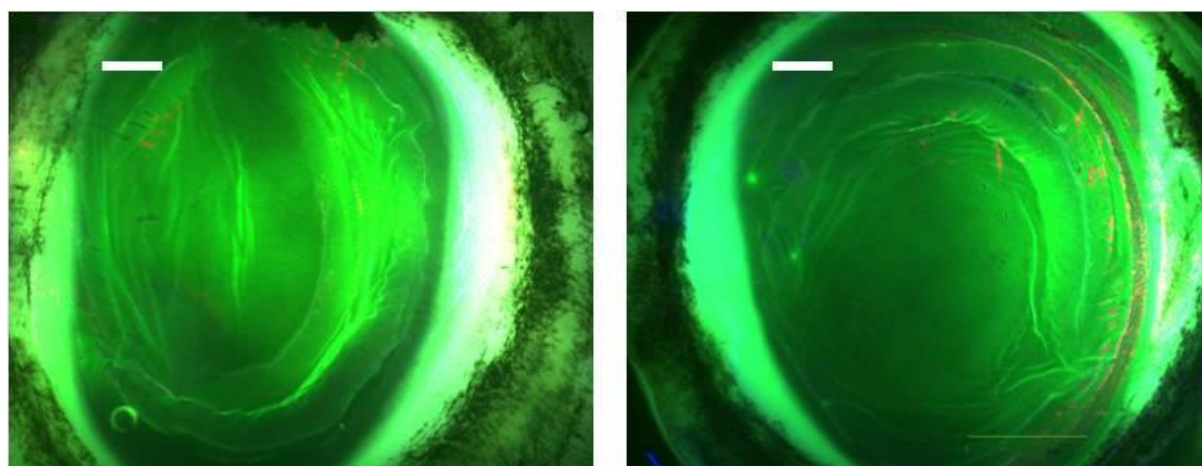


Fig. 5. 5: Control cornea without incision/s. The control corneas clearly show a uniform green area covered with live cells with very few dead cells at the periphery which are mainly due to the treatment/holder of the cornea. Scale bar= $1500\mu\text{m}$

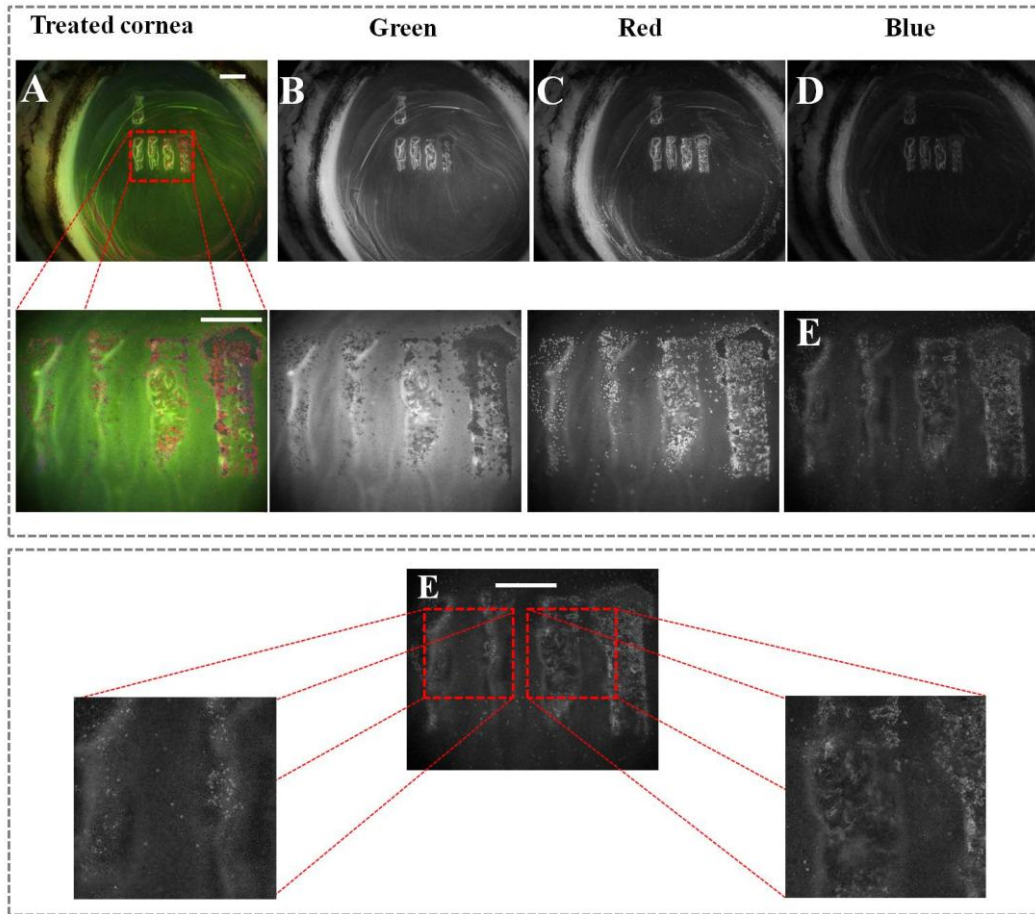


Fig. 5. 6: *Treated cornea with laser pulses that makes a lamellar incision of $500 \times 2000 \mu\text{m}^2$ inside the volume of cornea (total five in number as shown in figure). Fluorescence image observed by the microscope (Nikon AZ-100) (A), Green (living cells) (B), Red (dead cells) (C), Blue (nuclei of all the endothelial cells)(D). Nuclei visibility with respect to different magnification (E). Scale bar= $1500 \mu\text{m}$, where the black part in the fluorescence image shows absence of endothelial cells.*

Figure 5.6 shows the fluorescence image obtained for the treated cornea where panel A is the fluorescence image, panel B-D are the extracted green red and blue channels, and panel E represent the magnified image of the nuclei which show the same intensity difference already shown for figure 5.2-5.3. In comparison to figure 5.3 the image obtained for the treated cornea is green except at the incision area, which suggests that the omission of flat mounting has reduced artefactual cell death in endothelial folds. As the pictures are uniformly green, in the following, we will evaluate the percentage of surviving cells by quantifying the fraction of green pixels within the area of interest. The collected RGB images were processed and analysed using the software FijiImageJ [Jsc12]. The viability of the endothelial cells is related to the green channel, coded in a grey scale with a depth of 2^8 . Because of the slightly non-uniform intensity of the excitation light over the analysed surface, each incision area was split into several equivalent regions of interests (ROI), in order to permit normalisation and binari-

sation within ROI over which the excitation light intensity could be considered uniform within reasonable limits. The same number and sizes of ROI were chosen for all the incisions examined on any single cornea (Fig.5.7A). A typical image is shown in Figure 5.7B. This image consists of areas covered by live cells and areas covered by dying or dead cells (or devoid of cells in the case of very intense impacts). The histogram of pixel values for this picture show two distinct peaks (Fig.5.7C). ROI was then binarised using a manually chosen threshold between the peaks distinguishing live (white colour) and dead areas (black colour) (Fig.5.7D). The percentage of the pixels associated with a signal of the green channel is calculated through the available black area over the whole region of interest. By repeating the procedure for the remaining ROI gives us the mean live area and their standard deviation. The procedure proved to be robust and reproducible despite the subjectively chosen threshold.

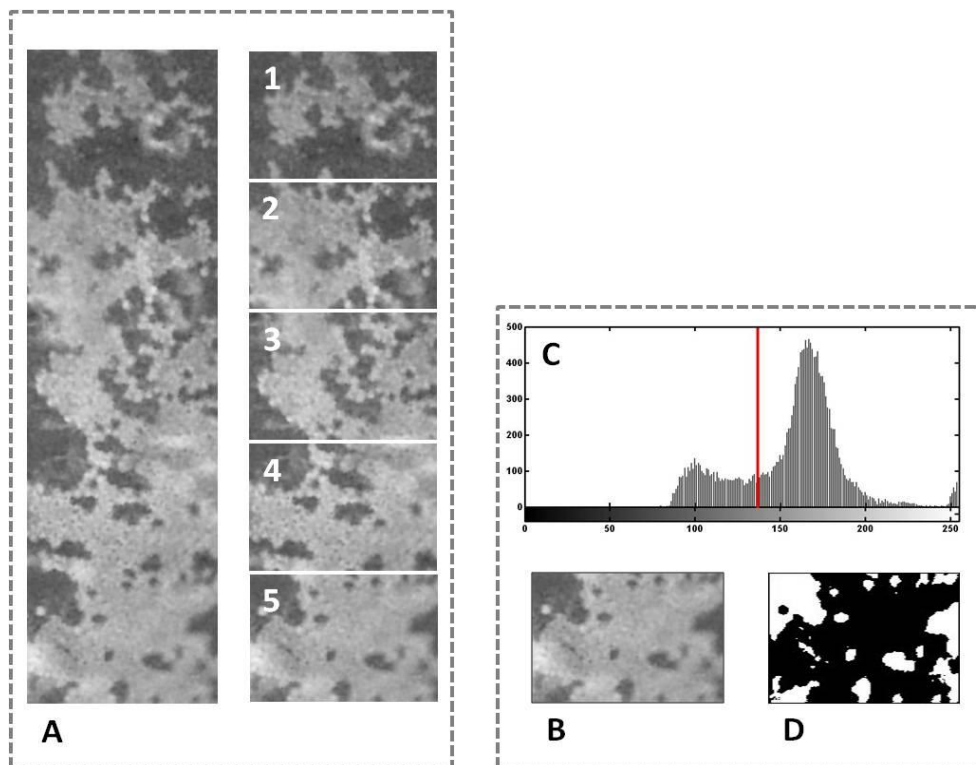


Fig. 5. 7: *Different steps in image analysis: (A) the incision area is divided into 5 parts; (B) one image is selected from the set, (C) the gray scale histogram shows two peaks, one for the fluorescence of the live cells and the other for the residual light intensity corresponding to the area without live cells; a point where it was possible to distinguish live area from the area without surviving cells was chosen as threshold, (D) the area occupied by live cells is shown in black while the area devoid of live cells is shown in white. The percentage of the area occupied by live cells with respect to the total area may then be calculated. Under the plausible assumption of constant cell density over the ROI, this gives the percentage of surviving cells. The process is then repeated for the rest of the ROI to obtain a mean value and their standard deviation.*

5.4 Results and Discussion

The results of our experiments are shown in Fig.5.8-5.9. Figure 5.8 was obtained by selecting a fixed value for the pulse energy (16.5 μJ) and increasing the distance between the focal spot and the endothelial cells. For a distance of 50 μm , the percentage of the surface occupied by live cells is very low. We also performed experiments for 100, 200, 300 and 400 μm ; with increasing distance the percentage of the surface occupied by live cells approached 100 %. For all distances we assume an error of 15 μm which we attribute mainly to slight variations of cover glass thickness and spot positioning due to tissular inhomogeneities. We then calculate the means of the points for each distance the corresponding graph is shown in figure 5.8B. We then performed a complementary set of experiments by inducing a lamellar incision at a fixed distance of 50 μm from the endothelium while subsequently decreasing the pulse energy from 17 to 2.15 μJ (Figure 5.9). At 17 μJ , no cells survived. The percentage of surviving cells increased with decreasing pulse energy and approached 100 percent for pulse energies of about 5 μJ and below. We also calculated the mean of the individual data points and the associated standard deviation which are shown in figure 5.9B (calculated in the same way as that of Fig. 5.8B). The data points within the transitional region between 5 and 16 μJ were omitted from this averaging process.

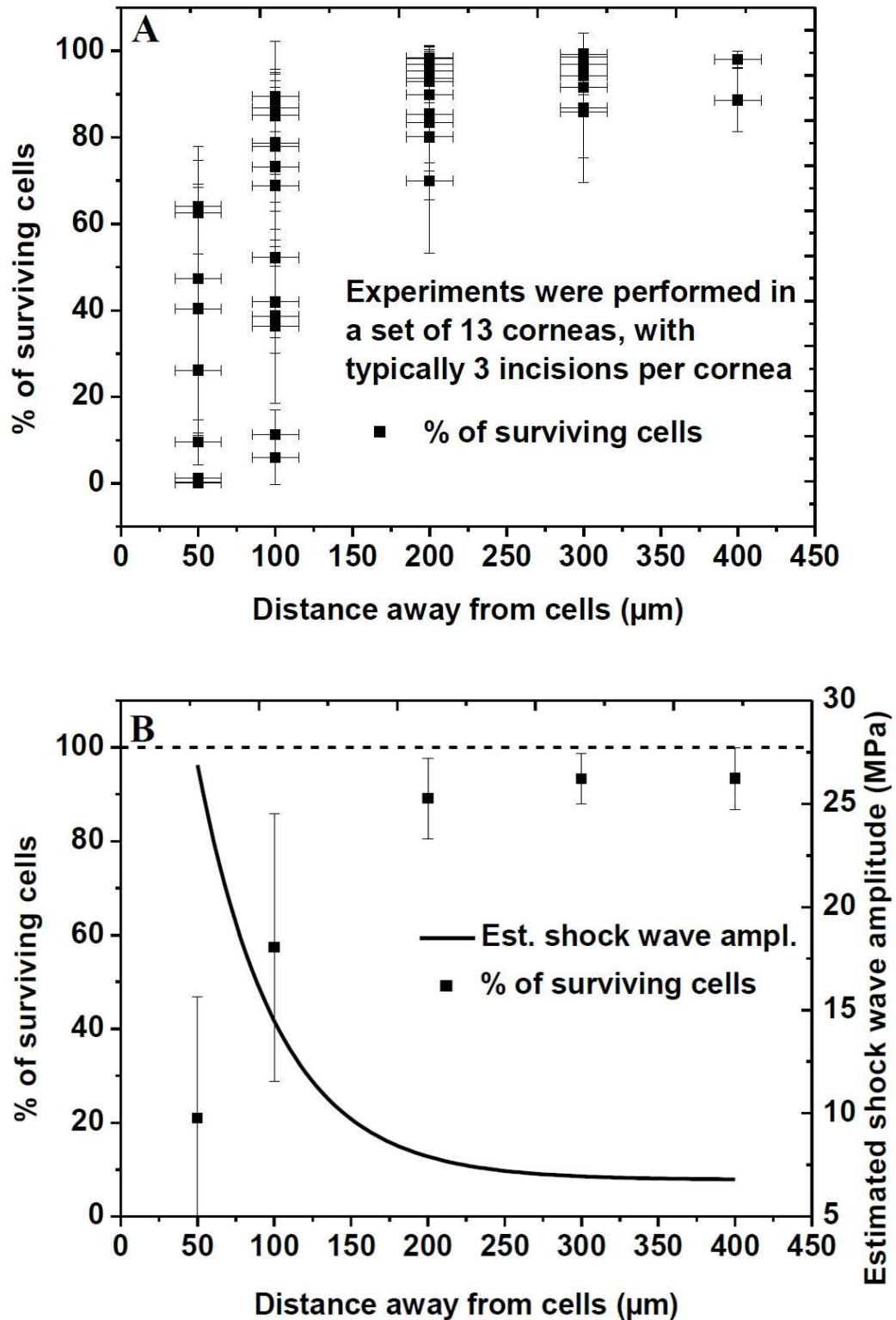


Fig. 5. 8: Percentage of surviving endothelial cells for incisions performed at pulse energies of $16.5\mu\text{J}$ at variable distances from the endothelium (A), average values and estimated shock wave amplitude (B).

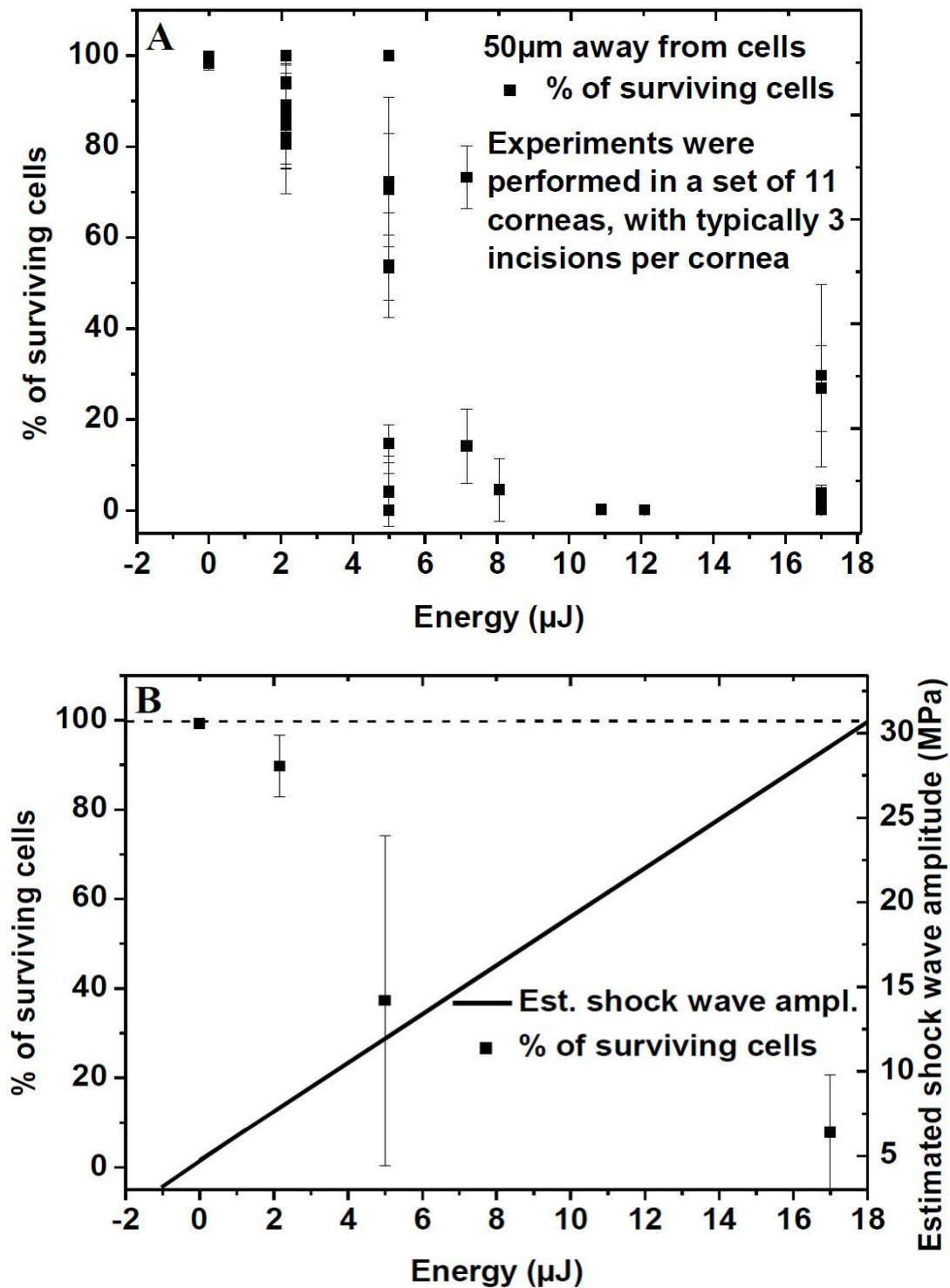


Fig. 5. 9: Percentage of surviving cells for incisions performed at a distance of 50 μ m from the endothelium at variable pulse energies (A), average values and estimated shock wave amplitude (B).

From both graphs it may be concluded that the surface fraction occupied by surviving cells increases with the distance of the impact from the endothelium (Fig. 5.8) and decreases with pulse energy (Fig. 5.9). In our experiment however the mechanism by which laser-tissue-

interaction process induces cell death is not known with certainty and may not be derived from these experiments, it is likely that the shock wave created by the interaction process causes cell death. The shock wave is a mechanical effect and is supported by earlier experiments using nanosecond laser pulses [Rau04] [Rau06] [Jon13] [Hel08] [Dik08], the results of which suggested that cell lysis may be attributed to shock wave generation and bubble formation. The amplitude of the shock wave amplitude can be estimated as follows:

- The radiant exposure at the focal spot decreases with increasing depth within the tissue due to the broadening of the spot by light scattering processes. The radiant exposure at the focus of the laser beam positioned in the volume of the cornea follows a Lambert Beer law (Fig. 5.10) [Ccr13].

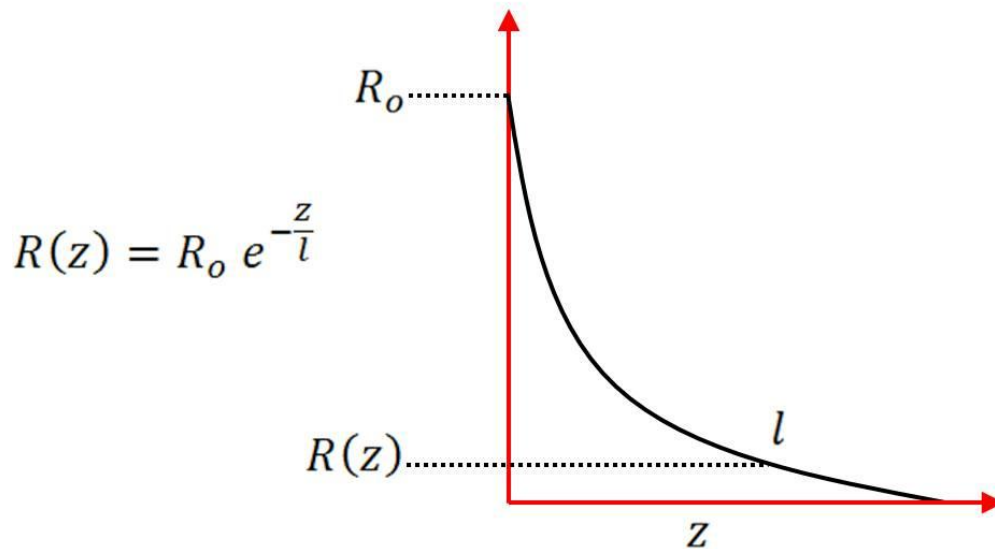


Fig. 5. 10: Decrease of radian exposure versus depth.

Here, $R(z)$ denotes the peak radiant exposure at a focal depth z in the tissue, R_0 is the radiant exposure created by the unaffected laser focus, and l is a characteristic penetration depth. By using the Lambert Beer law, C. Crotti *et al.* calculated the value of the penetration depth for a number of human donor corneas. Experimentally, this value was obtained by making incisions at different values of energy which resultant in different incisions depth. By making an exponential fit it was possible to determine the penetration depth [Ccr13]. (Fig.5.11)

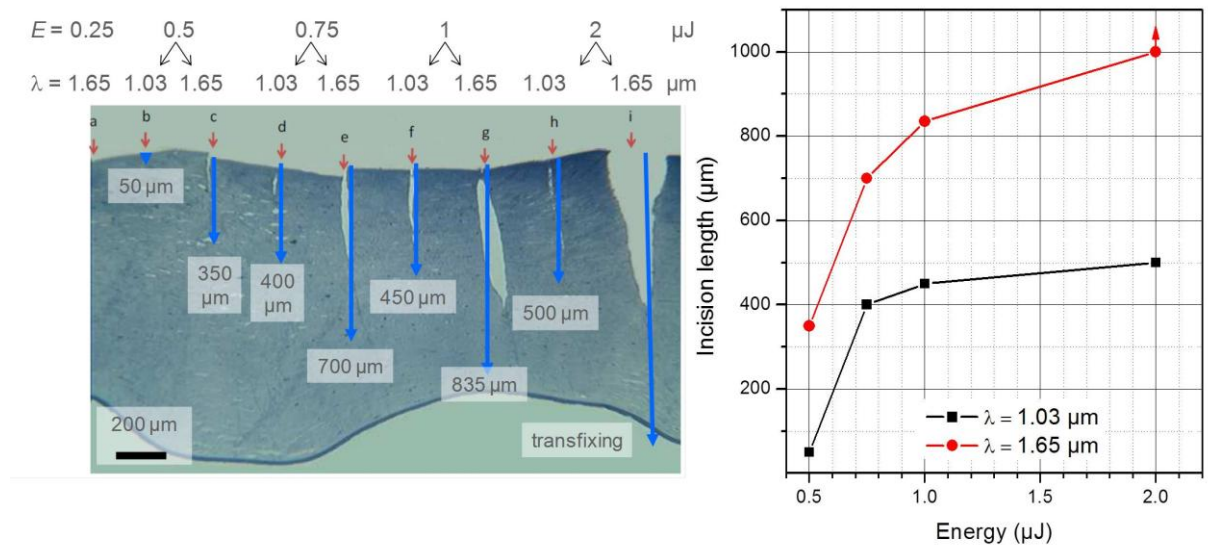


Fig. 5. 11: By making incisions with different energy values will result in different incision length, making a fit to these values will result in penetration depth [Ccr13].

Based on these results, for the healthy porcine corneas used here we may assume a value of about 300 μm for the penetration depth. We can then estimate the available radiant exposure for different distances from the endothelial cells (i.e. 50, 100, 200, 300 and 400 μm) used to obtain the results shown in figure 5.5A. By determining the ratio of this radiant exposure (R) to the threshold radiant exposure (R_{th}) required to create a bubble inside the cornea [Pla10] we can calculate the dimensionless parameter R/R_{th} . For the sake of comparison and later representation of our results we can also define E/E_{th} , where E and E_{th} corresponds to the energy that is required to produce radiant exposure R and R_{th} .

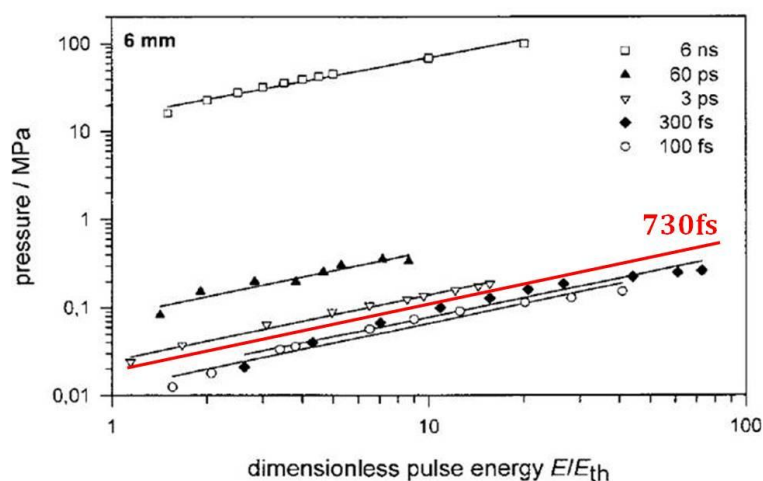


Fig. 5. 12: Stress-wave amplitude at a distance of 6mm (in MPa) for different pulse durations as a function of dimensionless laser pulse energy where the red line represent the linear fit for the pulse duration of our laser source [Vog05].

-
- This parameter can then be used to estimate the shock wave amplitude by using the data in Figure 5.12 (To best of our knowledge, precise data for shockwave by femto-second laser pulses inside corneal tissue at pulse energies as high as those used here is not available.). The data presented in Figure 5.12 has been obtained for microjoule femtosecond laser pulses focused into water, shock wave amplitudes in the mega Pascal were observed at a distance of 6mm in the direction perpendicular to the optical axis. Amplitude of shockwaves inside the cornea can be estimated by extrapolating data presented in figure 5.12 where we have also presented an approximate linear fit for 730 fs (the pulse duration of our laser source).
 - These experiments were performed in water under controlled focusing conditions. For these controlled conditions, calculations show that the shock wave amplitude in radial direction is higher than in axial direction because of the elliptical shape of the plasma generated by the laser pulse. These conditions are not verified in our case where the plasma is created in corneal tissue by a broadened and presumably irregular laser spot. In order to make a meaningful estimate for the average amplitude travelling along the optical axis towards the endothelium, we therefore renormalise the data for isotropic energy dissipation in order to obtain a mean value for our estimation. We can then estimate the resulting amplitude of the shock wave at the endothelial layer by considering a decay law of the form $\text{Pressure} \propto 1/r^n$ where $n = 1.12$ [Vog05]. Because of the various uncertainties of the assumptions made for the estimation, we consider the predicted absolute values to be an estimation of order of magnitude. The values should however be quite consistent with respect to a relative comparison. It has also to be taken into account that at the high pulse energies used for some of our experiments, the laser beam can encounter non-linear effects such as self-focusing. Given the presumably irregular nature of our laser spot, optical breakdown at multiple sites may occur within the cornea leading to multiple shock waves [Hhu10] and anisotropic shock wave propagation [Vog05]. The whole estimation process is summarised in the following block diagram (Fig.5.13).

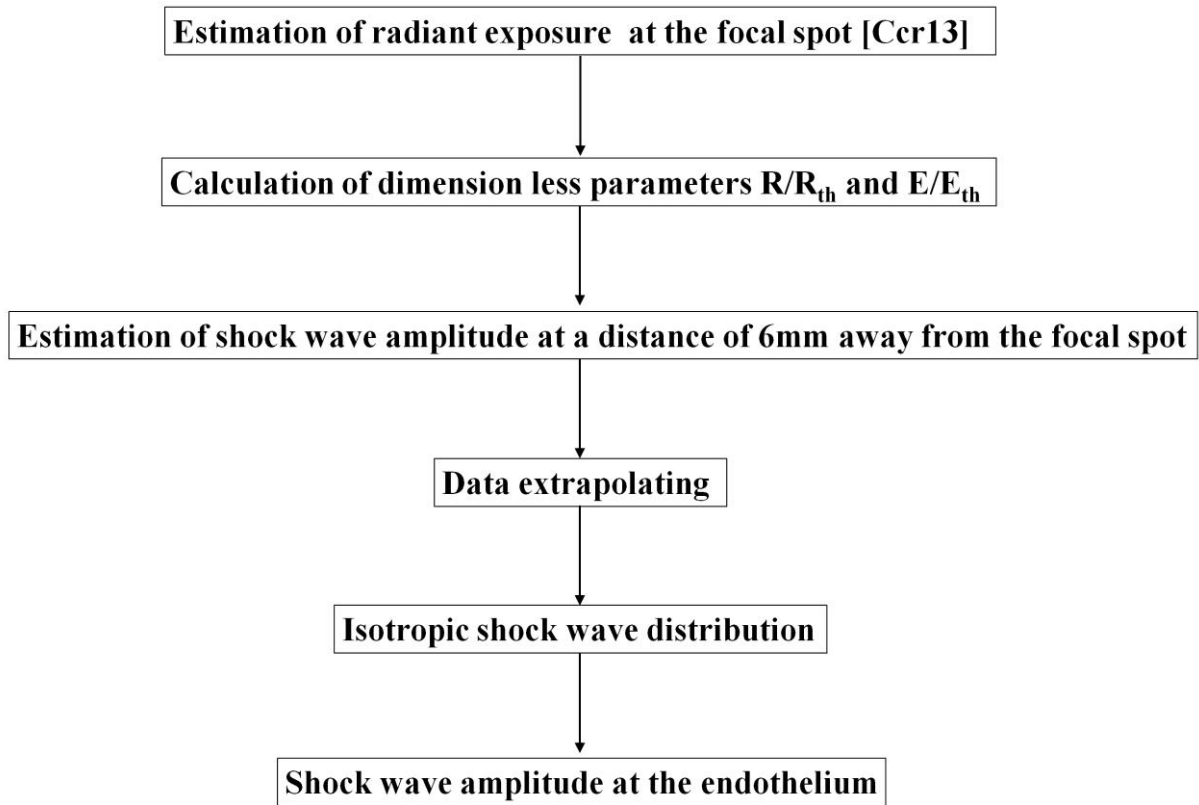


Fig. 5. 13: *Different steps to estimation shock wave amplitude.*

The resulting values for different distances are tabulated in Table 1 and plotted in figure 5.8B. Figure 5.8B shows that for a value of around 27 MPa cell viability will be nil whereas for a value of around 7 MPa the percentage of surviving cells will be well above 90%.

Distance (µm)	Estimated shockwave amplitude (MPa)
50	27
100	14
200	9
300	7
400	6

Table 5. 1: *Estimated shockwave amplitudes for the case of constant energy (16.5 µJ) and variable distance.*

Using the same method we calculated the estimated shock wave amplitude at the endothelium for the case of constant depth and variable energy. The resulting values are tabulated in Table 2 and plotted in figure 5.9B. Again, below a value of about 7 MPa the percentage of surviving cells approaches a maximum value (>90%).

Energy (μJ)	Estimated shockwave amplitude (MPa)
14	25
12	21
10	17
8	15
6	12
4	10
2	7

Table 5. 2: *Estimated shockwave amplitude for the case of variable energy and constant distance of 50 μm from endothelium cells.*

5.5 Conclusion

- We have investigated the effect of ultrashort laser pulses on the viability of porcine corneal endothelial cells as a function of pulse energy and proximity of the incisions to the endothelium.
- Our results show that under our experimental conditions, high pulse energies of about 16.5 μJ compromise the endothelial cell viability when the incisions are positioned within 100 μm distance of the endothelium. Likewise, at a distance of 50 μm , cell viability was affected when using pulse energies of about 4 μJ and higher.
- The exact mechanism responsible for cell death has not been identified conclusively. However, it is generally accepted that the likely cause is shock wave creation during plasma creation and bubble formation. We have made estimates about the shock wave amplitudes having affected the endothelium in our experiments. The onset of cell deterioration and death occurs at amplitudes of the order of 10^2 MPa.

Chapter VI

Dynamics of fs pulse interaction with corneal tissue and a collagen (type I) solution

A note on authorship: This chapter presents a study on the interaction dynamics of femtosecond laser pulses with corneal tissue and an aqueous solution of collagen. This study was initiated by our group; however, the experiments were conducted at the Institute of Electronic Structure and Laser at the Foundation for Research and Technology at Heraklion, Greece, during a two-week stay of myself and Tal Marciano, a previous PhD student of the group, under the supervision of Dimitris G. Papazoglou. The text below has been adapted from a draft manuscript⁴ to which he has made core contributions. Some of the results have been presented previously in the thesis of Tal Marciano.

6.1 Abstract

In this paper, we have dynamics of the interaction process of ultrashort laser pulses with porcine corneal tissue and an aqueous solution of collagen using a pump-probe digital holographic method. The corneal tissue and the collagen solution showed similar interaction dynamics which were however significantly different from water.

6.2 Introduction

Since the development of compact diode-pumped ultrashort pulse laser sources in the late 1990s and the subsequent development and commercialisation of clinical laser systems for ophthalmology, those lasers are now routinely used in eye surgery [Pla10] [Hks09].

When an ultrashort laser pulse is focused inside a transparent tissue it creates a strongly localised plasma via a combination of multiphoton and avalanche ionisation processes. Above the threshold for optical breakdown, a bubble is created and a shock wave travels into the medium away from the focal spot [Vog05]. Due to pressure imbalance between the bubble content and the surrounding medium this bubble can undergo several cycles of collapse and

⁴ In case of a submission of this text for publication, the likely order of authors is will be as follows: D. G. Papazoglou, S. Tzortzakis (IESL-FORTH), S.A. Hussain, Z. Essaïdi, T. Marciano, and K. Plamann (LOA).

expansion associated with the creation of shockwaves with oscillating amplitudes until the contents of the bubble is resorbed by the tissue and a permanent incision remains.. The exact nature of the laser-tissue interaction process and the quantification of the parameters involved still is a research subject of considerable interest. The different physical phenomena are usually studied by considering water as an equivalent to ocular tissue [Tju96], although differences may be expected in particular concerning the ionisation dynamics. In this paper we have studied the interaction dynamics for corneal tissue and a model solution of type I collagen using an pump-probe approach based on the principle of in-line digital holography. The results were compared to data for pure water.

6.3 Experimental technique

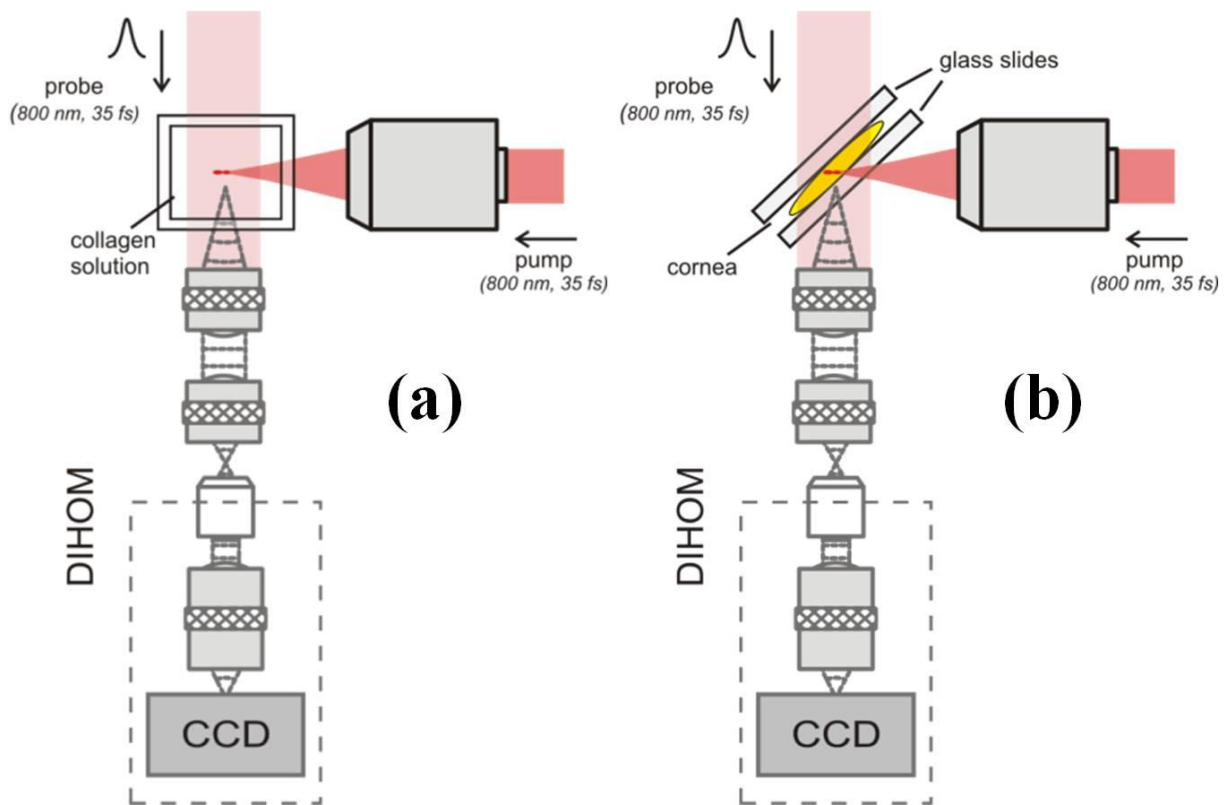


Fig. 6. 1: Pump-probe experimental setups, with an integrated in-line holographic microscope for the observation of the transient dynamics in the focal area (a) transverse pump-probe geometry for the collagen solution (b) tilted 45° geometry in a strongly scattering cornea sample.

6.3.1 Sample preparation

For the experiments shown here we have studied a homemade collagen type I solution 0.38% w in acetic acid and porcine cornea. The collagen solution was put in a rectangular

glass cuvette ($12.5 \times 12.5 \text{ mm}^2$ with 2.5 mm wall thickness) permitting the unperturbed transmission of light both from the front and back and from the sides (Fig.6.1 (a)). The porcine cornea was obtained from a local slaughter house were transport within 4 hrs and remain stored at 4°C . The cornea was sandwiched between the two microscope glass slips (Menzel Gläser, Saarbrücken , Germany).

6.3.2 Experimental set-up

The experimental set-up is shown in Fig 6.1.(a). An amplified Ti:Sapphire laser system producing 35 fs pulses at 800 nm is used. The laser beam is split in two parts in a pump probe scheme. The pump beam is focused in the bulk of the sample via a 0.2 NA microscope objective. The collimated probe beam crosses perpendicularly the pump focal region at various delays, and the induced transient refractive index changes perturb its amplitude and phase. An in-line holographic microscope is then used to remotely retrieve high resolution holographic images of the perturbed probe beam along its propagation. By combining a number of these holographic images and applying a numerical iteration process, both the phase and the amplitude of the probe wavefront are retrieved. Finally, the 3D distribution of the real and the imaginary part of the refractive index perturbation are revealed using Abel inversion. The technique is capable of measuring small transient changes (down to $\sim 10^{-4}$) in both the imaginary and real part of the refractive index of micron-sized volumes. A detailed description of the technique can be found in [Dgp08] [Dab11]. Such a detailed approach is not possible in the case of the cornea samples due to the strong scattering. In this case, as shown in Fig. 6.1(b) we follow a slightly different approach. The cornea sample is placed between two glass slides and tilted at 45° in respect to the pump and probe direction. This approach makes it possible to irradiate the bulk of the cornea and still being able to the perturbation of the probe beam in the focal area. Due to the scattering nature of the cornea sample any pump induced phase perturbation of the probe beam is practically lost but we are still able to monitor any absorption of the probe beam in the focal area. Regarding the temporal resolution this tilted approach, in combination with the scattering nature of the cornea sample, spreads the pump pulse thus reduces the temporal resolution in the initial excitation stage.

6.4 Results and discussion

The normalized absorption of the probe beam in the excitation area for a $0.75 \mu\text{J}$ pump beam is shown in Fig. 6.2(a) for various delays. The traces are shifted vertically for visualization purposes and refer to the longitudinal distribution, along the pump propagation direction, of the absorption of the probe beam. The excited focal area is clearly visible as an absorption peak at ~ -1.33 ps delay. As the delay is further increased the pump beam propagates to the right and the length of the excited region is increased reaching $\sim 23 \mu\text{m}$ at 0 ps delay. The transient absorption dynamics induced by the propagation of the intense pump beam in the cornea reveal the important role of nonlinear propagation effects. Similarly to polymers, such as poly(methyl methacrylate) (PMMA) [Dpa14], such intense beams excite electrons that due to the action of nonlinear propagation effects reach densities well below the critical density [Dpa14] [Dgp07] [Aco07]. The comparative temporal dynamics of the excitation and trapping in cornea and collagen solution, as it revealed through the normalized temporal evolution of the absorption in the focus area, is shown in Fig. 6.2(b).

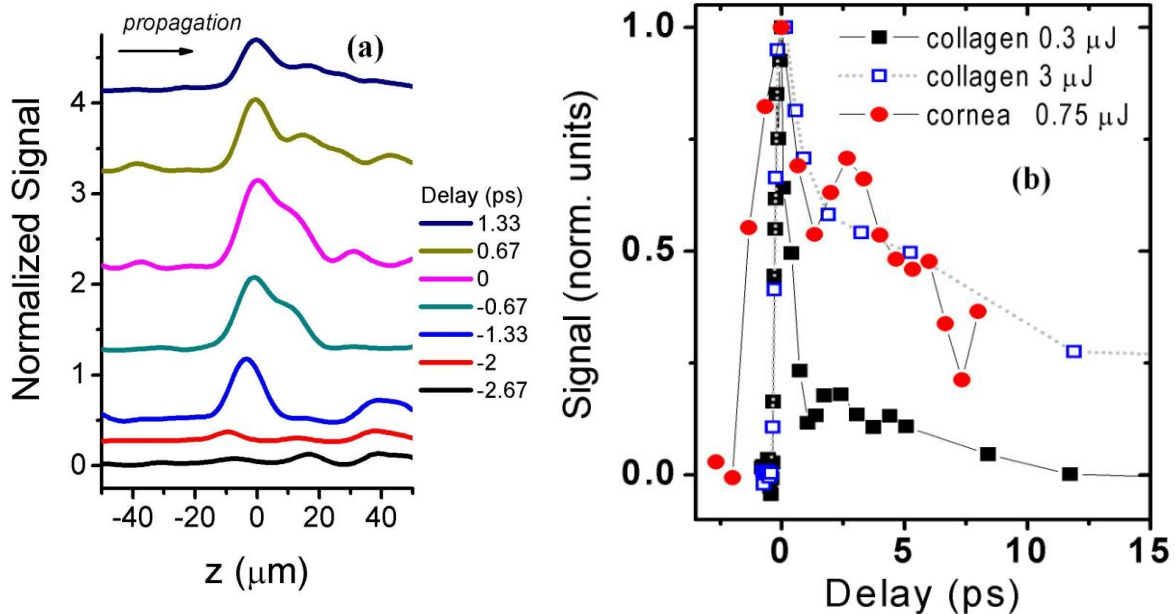


Fig. 6. 2: Normalized absorption signal in the excitation area (a) spatiotemporal evolution of the excitation in the cornea (b) comparative temporal evolution of the normalized absorption signal in the focal area for cornea sample and collagen solution.

The fast absorption increase near zero delay indicates the spatiotemporal overlap of the pump and probe beams and is correlated to the excitation of electrons through multi-photon absorption and ionization. The slower increase of the absorption signal in the case of the cornea sample is a side effect of the tilted geometry and does not affect the post-pulse temporal resolution. Interestingly, the post-pulse temporal dynamics of the cornea and the collagen solution are similar. The similarities in the post-excitation temporal evolution of the absorption between cornea and collagen can be better visualized in Fig. 6.3 where the absorption values are normalized in such a way that the absorption in the secondary peak is similar. Following a fast decay, indicative of electron trapping, the absorption is increased exhibiting a secondary peak at ~ 2.5 ps delay. This increase in absorption is indicative of the formation of a transient species or re-ionization of the medium. The whole effect starts from ~ 1.3 ps and washes out at ~ 4 ps delay and we believe is related to a chemical decomposition [Dpa14] initiated by the dissociative attachment of electrons excited in the initial excitation stage. The transient absorption peak is shadowed if when the excitation energy in the collagen solution reaches $3 \mu\text{J}$.

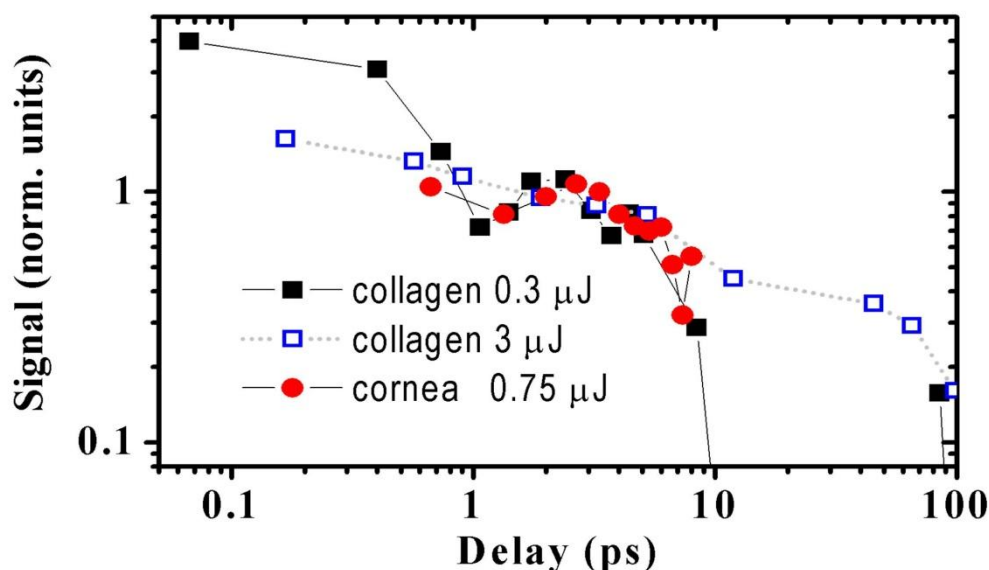


Fig. 6. 3: Comparative post excitation temporal evolution of the normalized absorption signal in the focal area for cornea sample and collagen solution. The absorption values are normalized at the secondary peak.

Finally, in the case of the collagen solution we are able to use the full capabilities of in-line holography and retrieve the 3D distribution of the refractive index perturbation. The spatial distribution of the transient refractive index change in the collagen solution is shown in Fig. 6.4. The transient refractive index change reaches values of $-2 \cdot 10^{-3}$.

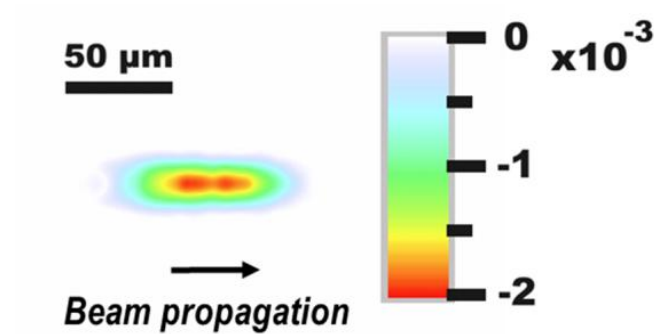


Fig. 6. 4: *Spatial distribution of the refractive index (real part) after excitation of collagen (type I 0.38% w) solution. Pump pulse : 0.3 μ J (35 fs, 800 nm), delay ~ 0 ps*

The similarity in the temporal dynamics following the irradiation with ultra-short intense pulses between cornea and collagen solution indicates that the collagen presence in the cornea strongly influences the photochemistry of the interaction at least at the first few tenths of ps. This hypothesis is strengthened by the fact that in both cases transient absorptive species, even though their true nature is not clear yet, are formed ~ 2.5 ps after excitation.

The observed temporal dynamics in cornea and collagen solution are distinctly different than that of water. To support this we can use some of our previous measurements of the spatiotemporal dynamics in water both unpublished and published [Dfa12] that are also supported by results published by other groups [Csc02] [Smi08].

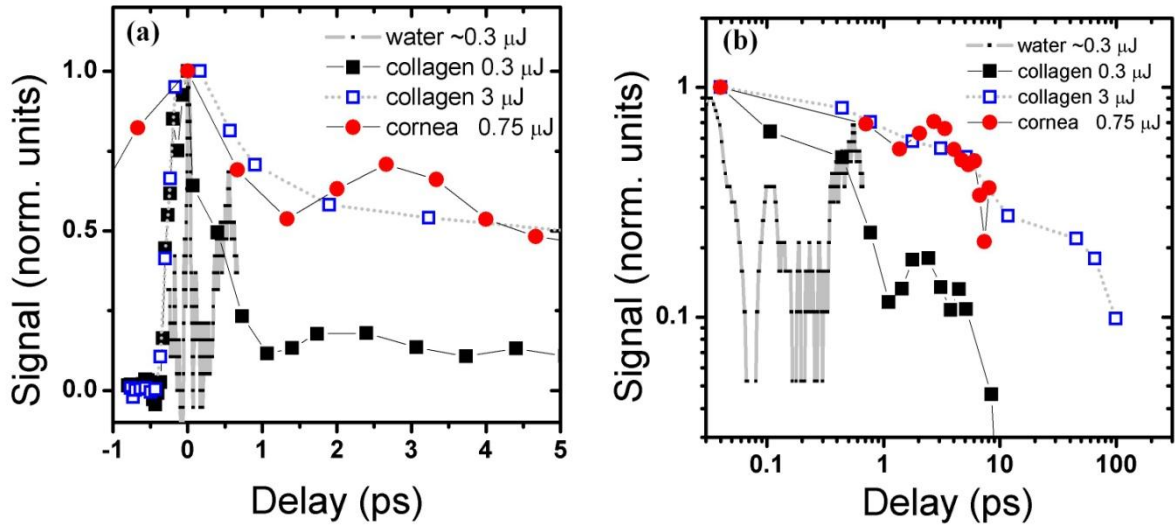


Fig. 6. 5: Comparative temporal dynamics after IR fs excitation in water, cornea and collagen solution. (a) linear scales (b) Log-Log scales.

A direct comparison of the temporal dynamics after IR fs excitation in water, cornea and collagen solution is shown in Fig 6.5. Although our measurements for water reach up to ~ 1 ps there is a distinct difference between water and cornea/collagen. In water electron excitation is followed by a very fast trapping (<150 fs) followed by a secondary signal peak at ~ 600 fs that we have related [Dfa12] to solvated electrons. The delay between the appearance of this secondary peak as a function of the input energy for water IR fs excitation using an axicon is shown in Fig. 6.6. This delay does not seem to depend on the input energy and is 4 times smaller than the 2.5 ps delay of the observed cornea/collagen peak.

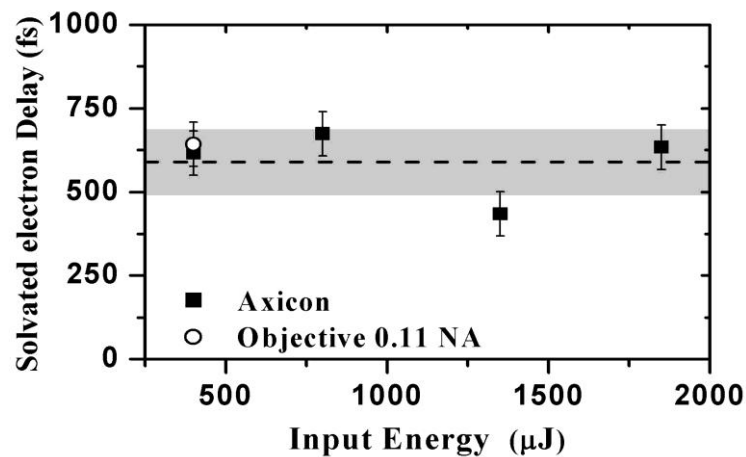


Fig. 6. 6: Delay of the appearance of the peak related to solvated electrons for the experimental conditions of ref. [Dfa12] (for axicon case the 400 μJ input energy is comparable to our experimental conditions)

Our results for water are in agreement to published results of other groups [Csc02] [Smi08] as shown in Fig. 6.7-6.8.

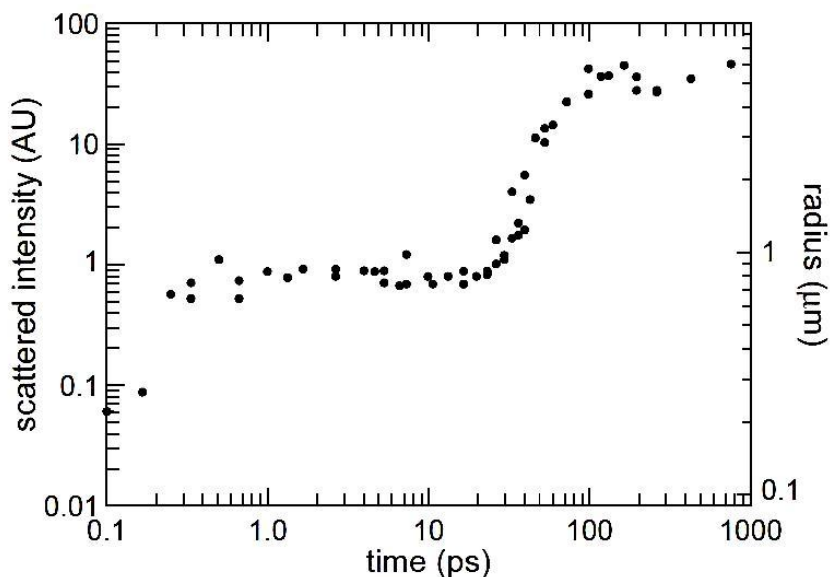


Fig. 6. 7: Signal scattered intensity. Similarities to our results: a minor (in this experiment) peak ~ 500 fs, no other significant peak from 1-10 ps [Csc02].

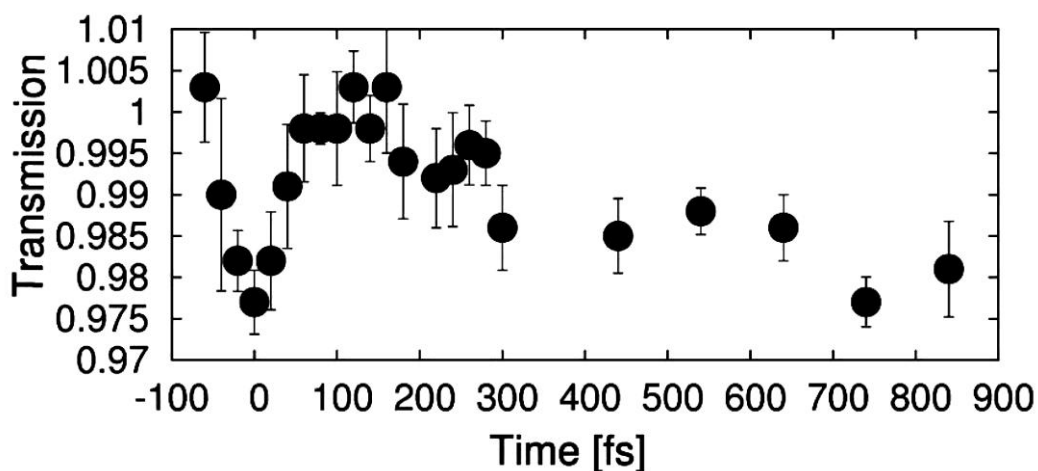


Fig. 6. 8: The absorption results are very similar to our measurements in water [Smi08].

In the future, two additional set of experiments will be performed. One on acetic acid acting as a control and other on various concentration of collagen dissolved in acetic acid acting as a solvent. These experiments will highlight the laser dynamics of acetic acid acting as a

control and different concentrations of collagen solutions will help us to identify the concentration that can produce/close to produce the laser dynamics inside the cornea.

6.5 Conclusion

- We compare the interaction dynamics of femtosecond laser pulses with water, collagen type I solution and cornea.
- Water which is usually use as a model substance for many studies of the interaction dynamics, in our experiment it was found that the interaction dynamics of water are quite different from those of cornea or collagen solution.
- The dynamics observed in the collagen solution and in actual cornea was quite comparable.
- In future, different concentration swill be examined in order to investigate the best concentration that will mimic the laser dynamics inside the cornea and a control experiment with only acetic acid.
- In light of our present findings we suggest to use collagen type I solution as a model solution to study the dynamics inside the cornea instead of water.

Conclusion and outlook

Since the development and commercialisation of the first ultrashort pulse laser system for creating corneal flaps for the LASIK⁵ procedure in refractive surgery in the beginning of the years 2000, their use in eye surgery has become current. Nowadays, they are used for corneal as well as for cataract surgery. In recent years, our group has performed studies in view of improving the performance of these lasers in pathological and therefore strongly light scattering tissue by notably by identifying optimal laser wavelength and by the development of appropriate laser sources.

In this context, the present thesis has addressed three main objectives:

- The development, optimisation and full characterisation of a compact, stable and robust ultrafast laser source that is capable of producing pulses at different wavelengths in the short wave infrared spectral range;
- The study of the effect of ultrashort laser pulses on the viability of porcine endothelial cells after different types of keratoplasty;
- The study of the interaction dynamics of ultrashort laser pulses with tissue and collagen solutions and its comparison to the behaviour of water which has served as a model substance for many studies concerning the interaction of ultrashort laser pulses with matter.

a. Results and conclusion

Development of femtosecond laser source

A laser source based on periodically poled lithium niobate crystals in the configuration of an Optical Parametric Generator (OPG) and an Optical Parametric Amplifier (OPA) has been developed. The crystals are pumped at a wavelength of 1.03 μm a commercial diode-pumped solid state laser system. The developed laser source is able to produce microjoule femtosecond pulses in the short wave infrared range (SWIR). We have performed detailed characterisation measurements concerning output pulse energy, control of the central wavelength and the output spectra, spatial profiles. The systems developed and refined during the

⁵ Laser *In Situ* Keratomileusis

present thesis are notably capable of producing output pulses at a wavelength of 1650 nm with reasonable spectral bandwidth. This wavelength had been previously identified as being optimal for femtosecond laser assisted corneal surgery in the case of pathological, light scattering tissue. The laser source is also able to produce 1300 nm which is may be of interest for optimising cataract surgery assisted by ultrashort pulse lasers. The wavelength conversion system is compact, rugged, and therefore potentially qualified for a use in clinical applications.

Cell viability in the endothelium of porcine cornea exposed to ultrashort laser pulses

We have studied the effect of ultrashort laser pulses on the viability of porcine corneal endothelial cells. Incisions were performed in porcine cornea using ultrashort laser pulses at a wavelength of 1030 nm. The viability of the endothelial cells was evaluated using a fluorescence marking protocol. The percentage of surviving cells was determined as a function of pulse energy and the proximity of the incisions to the endothelium. For high pulse energies ($\sim 17\mu\text{J}$) induced at small distances to the endothelial cells we have observed cell death; the cells survived at lower distances or bigger distances. The observations were reproducible within reasonable limits. The exact mechanism behind the cell death is uncertain; it is however likely that it is related to the amplitude of laser induced shockwaves at the endothelium. Due to unavailability of reliable data concerning shock wave amplitudes at such high energy values inside the cornea we made an estimation based on data available in the literature. For our experimental conditions an onset of cell deterioration and death occurs at estimated amplitudes of the order of 10^2 MPa. Our study may help to define “safe” parameter values; further research is needed to identify the mechanisms responsible for cell death with certainty.

Dynamics of fs pulse interaction with water, corneal tissue and a collagen (type I) solution

We participated in a study aiming to compare the interaction dynamics of femtosecond laser pulses with water, collagen type I solution and cornea. This study has been performed at and in collaboration with the Institute of Electron Structure & Laser and with the implication of another PhD student of the group. While water had been used as a model substance for many studies of the interaction dynamics, it was found that the interaction dynamics of water are quite different from those of cornea or collagen solution whereas the dynamics observed in the collagen solution and in actual cornea was quite comparable. In light of our findings we

suggest to use collagen type I solution as a model solution to study the dynamics inside the cornea instead of water.

b. Future work

The work address in this thesis covers different aspects of the surgery of the anterior segment of eye assisted by ultrashort laser pulses. Further work should address the following:

- The developed laser source can be used to study laser tissue interaction at different wavelengths. It can be use to study the surgical outcomes at different wavelengths and studies can address the effect of different pulse durations. The latter can be increased and maybe decreased by using stretcher and a compressor.
- The viability of cells can be studied further for different types of penetrating keratoplasty and mechanism of cell death can be studied in detail in order to define the parameters responsible for cell death.
- Different concentration of collagen solution will be investigated in order to discover the collagen concentration whose dynamics replicate or close to replicate the interaction dynamics of femtosecond laser pulses inside the cornea. An additional experiment on acetic acid will be needed as a control.

Appendix 1: Transparency of porcine lens

1.1 Introduction

The crystalline lens is a biconvex transparent lens located between iris and vitreous humour. The anterior surface is less convex than the posterior surface and enclosed in a bag known as lens capsule, this bag is attached to zonules known as ciliary zonules (Fig.1.1).

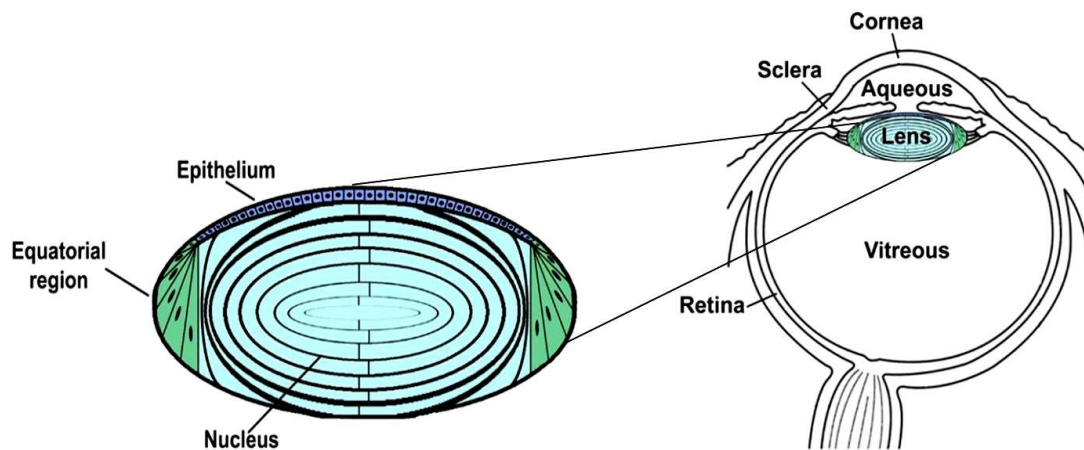


Fig.1. 1: The anatomy of crystalline lens (Modified from [Ecb13]).

The main composition of crystalline lens is water (66%) and proteins (33%), while the remainder consists of ions, glucose, glutathione, inositol and various acids. The main function of the crystalline lens is to provide accommodation for the focusing of the image onto the retina. The crystalline lens is has rotational symmetry around the optical axis. Enclosed in the lens capsule are the epithelium and lens fibres formed by cells arranged in concentric layers in an onion-like arrangement.

Although the structure of the crystalline lens is very different to the one of the cornea, a short range order within this structure is also likely to be responsible for its transparency [Gbe71] [Str62]. The existence of this short order was later confirmed by Delaye and Tardieu by using X-ray scattering techniques. They found that at high concentration of proteins (found in the crystalline lens) this short range order is sufficient to explain lens transparency [Mde83].

The global transparency of the human crystalline lens is shown in Fig. 1.2 (solid line). It is transparent in the whole visible regime and less transparent in the infrared range. Above

about 1000 nm transmission decreases because of the increased absorption particularly of water.

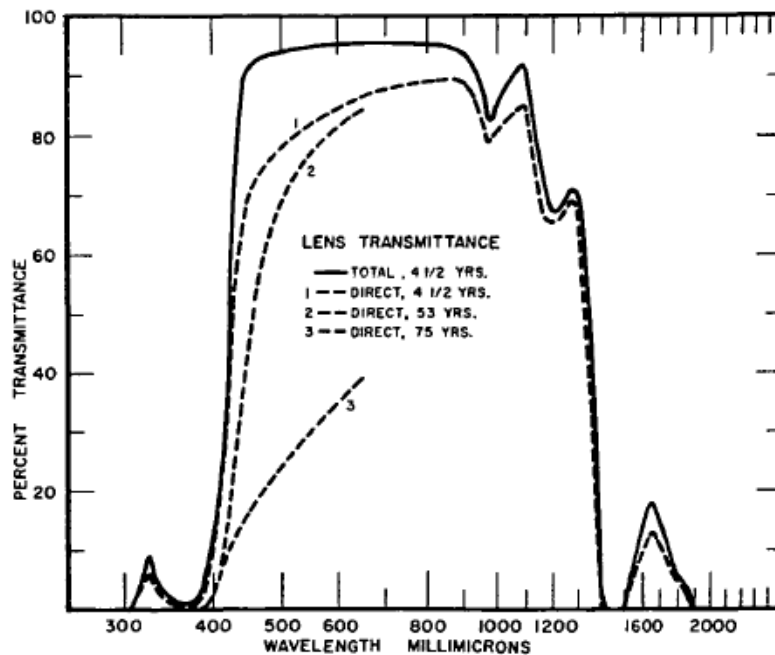


Fig.1. 2: Transparency of human crystalline lens [Eab62].

The development of cataract decreases transparency in the visible regime (400-700 nm). Cataract can then be explained in terms of formation of high molecular weight aggregates. These aggregates scatter light and, depending upon the concentration of these aggregates, the image on the retina is consequently blurred [Gbe71] [Jaj75] [Asp84]. The development of cataract may be caused by age, disease, habits, location and genetic predisposition. Depending upon its nature and severity, cataract can not only affect light scattering but also the lenses ability to focus the light onto the retina. Research studies are being conducted in order to understand effects of different environmental influences on cataract formation which include ultraviolet exposure, calcium level, oxidative stress, formation of reactive oxygen species, selenite level and sugar/glucose level [Trs97][Krh98] [Mab11] [Pgs03] [Jpi11]. There are three main types of cataract which are classified with respect to the affected region of the lens. These are nuclear, cortical, and posterior subcapsular cataracts (Fig.1.3).

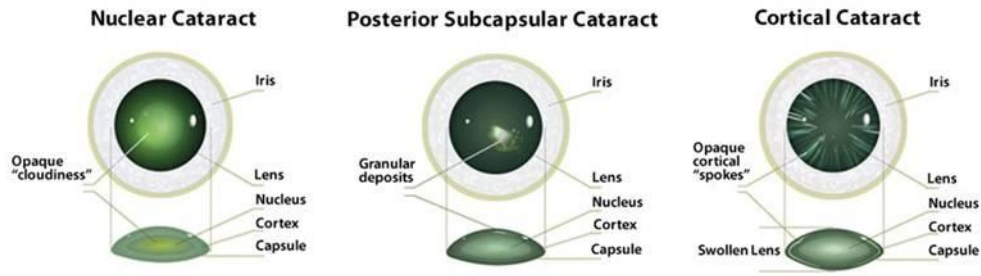


Fig.1. 3: Different types of cataractic lens [Mye].

If the cataract becomes severe, surgery is indicated. The contents of the lens capsule is removed completely and then replaced by an artificial lens usually known as intra ocular lens (IOL) (Fig.1.4). The surgery can be performed by using ultrasonic phacoemulsification or assisted by ultrashort pulse lasers. The main steps that include the removal of the capsule contents and its replacement with an IOL are: capsulotomy (to break up the crystalline lens into small fragments and opening of lens capsule from anterior side), making incisions on the cornea to access the lens fragments, removal of fragments and replacing it with the IOL.



Fig.1. 4: Intraocular lens (IOL) [Riv].

In comparison to underdeveloped countries where due to lack of facilities and awareness the cataract usually become mature before it can be treated, in developed countries the crystalline lens is usually removed in early stages when it still is relatively transparent. In the experiments described below we have studied the transparency of fresh porcine crystalline lens. In analogy to our work on cornea, these studies may help to identify optimal wavelengths for cataract surgery.

1.2 Methods and materials

The experiments presented here were performed on porcine crystalline lenses. Porcine eyes were obtained under permission from a local slaughterhouse. The eyes were retrieved from young pigs with an average age of about 6 months. The eye was transported to our site within 4 hours and used immediately.

For the experiment we have used Petri dishes with optical quality glass bottoms (μ -dish 35 mm high glass bottom, Ibidi, Munich, Germany). The bottom material is Schott borosilicate glass D 263M. The height of the Petri dishes was made shortened to just allow for the crystalline lens to remain covered in BSS (Balanced salt solution) solution. The crystalline lenses were held at a fixed position in the Petri dishes by an additional holder made of plexiglass (Fig. 1.5). This geometry is shown in the figure below.

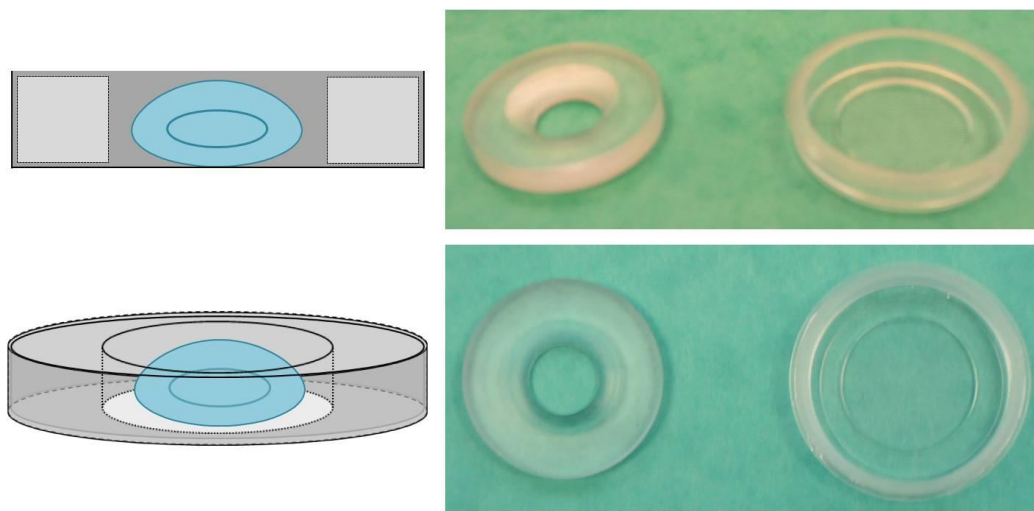


Fig.1. 5: *Petri dish consists of glass bottom along with the holder made of plexiglass.*

In order to study the transparency of the crystalline lens in this geometry we modified a previously developed experimental setup in order to be operational in the vertical direction. The former setup has been presented in [Dap10]. The method is based upon the determination of amount of light that passes through the lens regardless of direction of propagation (total transmission) which is then compared to the light experiencing negligible deviation from initial trajectory (direct transmission). The whole measuring process yields the percentage of light that experiences light scattering deviating the propagation direction out of a small solid angle around the optical axis.

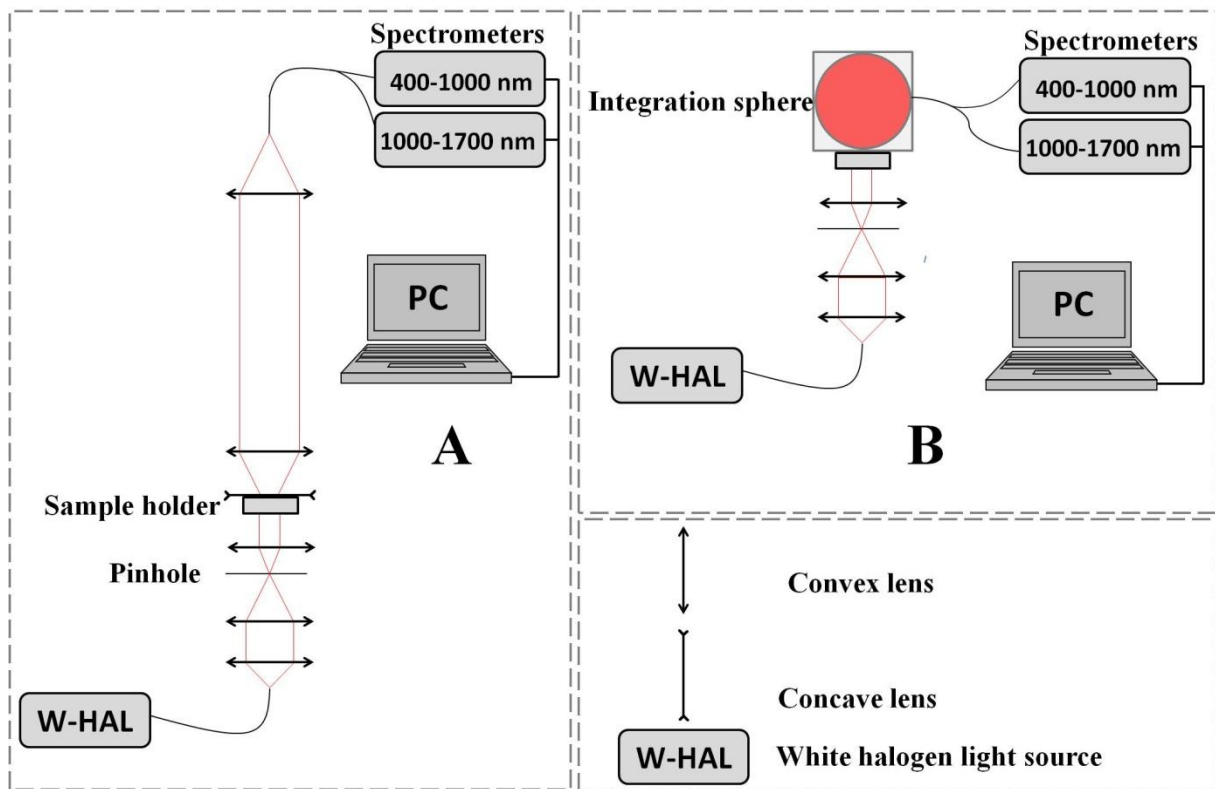


Fig.1. 6: *Experimental setup, direct transmission (A), total transmission (B).*

Figure 1.6 shows the experimental setup. Fig 1.6A shows the measurement of the un-scattered light through the crystalline lens. A continuous white light beam from a halogen-tungsten lamp (W-Hal in Fig. 1.6) (Avalight-HAL, Avantes, Apeldoorn, Netherlands, spectral range: 360 to 2500 nm) is coupled into a multimodal optical fibre. With the help of lenses, the light beam at the output of the fibre is then collimated to a diameter of about 3 mm. The light transmitted by the crystalline lens travels along a distance of 750 mm and is then coupled into a split optical fibre with an entry diameter of 600 μm and two output fibres with diameters of 200 μm . The solid angle (3×10^{-8} sr) was made identical to our previous study [Dap10].

Figure 1.6B represents the experimental setup use for total transmission. The setup uses the technique described previously, however, due to sensitivity of our integration sphere (FOIS-1; Ocean Optics, Dunedin, Florida) we use a slight bigger pinhole for spatial filtering. This pinhole is sufficient for the integration sphere to show noticeable signal however a compromise was made on the spatial quality of the beam. In both experiments a reference measurement (baseline) is recorded for the purpose of normalisation using the same Petri dish without the crystalline lens. Finally, the light was analysed by two spectrometers sensitive to

the visible and NIR light (400 to 1000 nm, AvaSpec 2048TEC, Avantes, Apeldoorn, Netherlands) and NIR-SWIR light (1000 to 1700 nm, AvaSpec-NIR256, Avantes, Apeldoorn, Netherlands), respectively.

1.3 Result, discussion and conclusion

The result obtained on a porcine crystalline lens is shown in figure 1.7. The result we have obtained is similar to those already presented in the previous studies of Boettner and Wolter (Fig. 1.2) [Eab62] and also resembles the transmission of water [Dsa10].

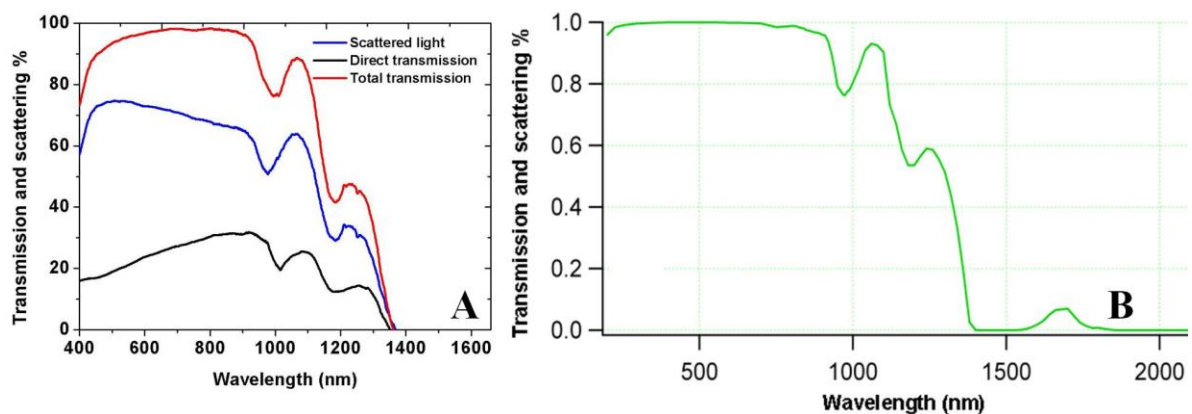


Fig.1. 7: *Transmission of crystalline lens (A), transmission of light through 3mm of thick layer of water (B) [Dsa10].*

The porcine crystalline lens is transparent up to about 900 nm, beyond which its transparency decreases. Like for water and human crystalline lens we also observe secondary peaks around 1100 nm and 1300 nm the amplitude of which is however lower than water and human crystalline lens. The peak at around 1650 nm was not detectable in our case. While light scattering at 1650 nm is expected to be very low, the value of penetration depth limited by light absorption is also very low at this wavelength [Dap10]. By balancing between penetration depth and scattering, 1300 nm could be a viable compromise for a use it for cataract surgery assisted by ultrashort pulse lasers, but further studies and refined measurements will be needed.

Appendix 2: Kerr effect

Non-linear effects can influence the spatial and temporal properties of a propagating laser beam. Different non-linear optical effects have been described in chapter 3 of this thesis. One of them is the Kerr lens phenomenon which depends on the third order susceptibility $\chi^{(3)}$. When a high power beam passes through a medium having a positive $\chi^{(3)}$ it will experience focusing towards the optical axis. In such a case the total refractive index of the medium can be written as:

$$n = n_o + n_2 I , \quad (\text{Eq. Ap. 2. 1})$$

where n is the total refractive index of the material, n_o is the linear refractive index, and n_2 is the non-linear refractive index coefficient, and I is the intensity.

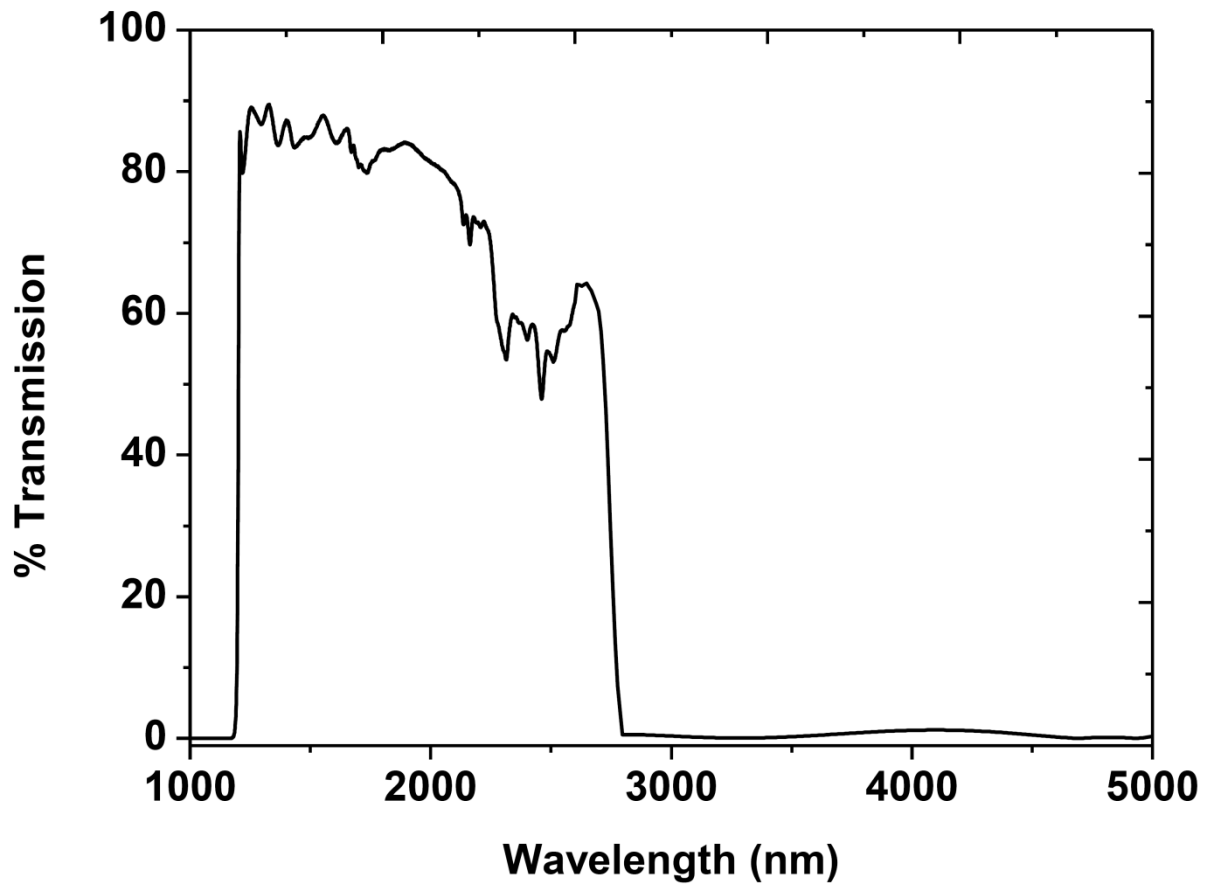
In our experiments we have used beams with profiles close to a Gaussian profile whose intensity is higher at the centre than the periphery. If this beam is propagating through a medium with positive third order susceptibility then the beam profile experiences self focusing towards the optical axis and the whole system will act as a gradient index lens. The formula that can be used to calculate the power for which self focusing occurs is given by:

$$P = \frac{\pi (0.61)^2 \lambda^2}{8 n_o n_2} , \quad (\text{Eq. Ap. 2. 2})$$

where λ is the wavelength of light. Interestingly, the above formula does not depend upon the diameter of the beam. It means that a beam with a large diameter will also experience self focusing if its power is greater than or equal to critical power.

For a beam with a power just equal to critical power, the beam will propagate with constant diameter. However, if the value is greater than the critical power it will continue self focusing until the beam will collapse and experience other nonlinear effects like the formation of filaments.

Appendix 3: Transparency of high pass filter



Appendix 4: NEXPRESSO Project



NEXPRESSO

**Network for EXchange and PRototype Evaluation
of photonicS componentsS and Optical systems**

Final Report

Laser Beam and Tissue Characterisation for Ultrashort Pulse Laser Eye Surgery

R&D lab: ENSTA ParisTech (Karsten Plamann, Zacaria Essaïdi, Syed Asad Hussain)

Component supplier: NETIS System / ALPhANOV (Jean-Pascal Caumes / Bruno Chassagne)

Introduction

The eye is one of the most exciting sense organ of the human body which allows us to see the world surrounding us. Within the eye (figure 1), the cornea is the first biological tissue and a powerful optical element that accounts for approximately two-thirds of the eye's total optical power. It is a layered structure whose transparency plays a key role in vision. Many of its optical properties have been investigated in the past; however further researches remain to be performed to fully understand the related optical phenomena. One of these phenomena is with the scattering of light inside the cornea which is wavelength dependent. Hence the performance of the incisions performed using surgical lasers is wavelength dependent.

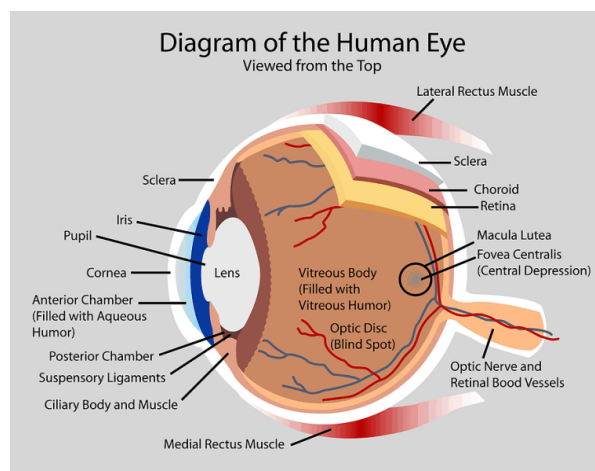


Fig. 1: *Anatomy of the eye* (<http://www.opticalmasters.com>)

Our previous work led us to identify a small spectral window of corneal transparency in the short wavelength infrared range (SWIR). In order to apply this finding to corneal surgery assisted by ultrashort laser pulses we developed a laser source based on non-linear optical crystals that permits us to produce laser pulses at the wavelength of 1650 nm. By the means of the multi-wavelength camera acquired within the NEXPRESSO project, several tasks were performed. In a first step, we developed a procedure to investigate different properties of the beam generated by non-linear optical crystals (periodically poled magnesium doped lithium niobate) in two different geometries known as optical parametric generator (OPG) and optical parametric amplifier (OPA). In this latest part of this project two tasks were investigated. We first performed an experiment to investigate the propagation of spatial frequencies within objects using a Fourier optical approach and to study the beam properties. We then investigated the beam spot size modifications after its propagation through the whole thickness of the cornea in order to study its degradation.

Summary of previous work

1.1 Report 1: Analyses of the spatial beam profile of beams generated by a nonlinear optical system

The multi-wavelength NEXPRESSO camera was used to perform analyses on the 3D spatial profiles of the beams generated by a periodically poled magnesium doped lithium niobate crystal in the configuration of optical parametric generation (OPG). By improving the contrast of the images and analysing the 3D beam profiles, we were able to point out small distortions of the the spatial profile of the beam generated by the nonlinear crystal.

1.2 Report 2: Optimisation of the laser beam quality and analyses of a scattering medium

A new and improved procedure was proposed to treat the images obtained by the NEXPRESSO camera by using FLIR QuickReport. With the proposed technique, the processed images exhibit a better quality and can also be analysed by other software such as MATLAB[®] to yield detailed information.

In addition to the previous work dealing with a beam generated by a non-linear optical crystal, we completed the study by investigating the beam generated by an optical parametric amplifier (OPA). The obtained results showed that the generated beam properties were stable for more than 30 min as well as it spatial profile.

In the last, we proposed an experimental setup that can be used to determine the spot size inside the biological tissue. A an anisotropic diffuser was used as test medium. The obtained results were in a good agreement with the orientation of the diffuser.

“Laser beam and tissue characterisation for ultrashort pulse laser eye surgery”

R&D lab: ENSTA ParisTech (Karsten Plamann, Zacaria Essaïdi, Syed Asad Hussain)

Component supplier: NETIS System / ALPhANOV (Jean-Pascal Caumes / Bruno Chassagne)

1.1 Abstract

In this report, we describe an experimental setup which allows us to investigate the structure of the corneas by using Fourier optics. For this purpose, we measured the quality of the focal spot of a laser beam focused at the back of corneas using a microscope imaging geometry. The beam firstly crosses two microscope objectives set as an afocal system before being focused onto the NEXPRESSO camera sensor plane. As expected a broadening of the beam spot was observed when we insert the cornea in the afocal system. In the next experiment, by moving the sample in the propagation direction, we imaged the focal spot at different planes inside the corneas. The obtained results in terms of FWHM reveal similar evolutions for corneas, and that the camera was sensitive to the thickness variations of the corneas.

1.2 Introduction

In the framework of the NEXPRESSO project, we used the multi-wavelength camera TeraCam to investigate the biological tissues properties through optical means. At the beginning, we present the complete optimisation process used for the images acquisition of camera. With the help of the camera, we were able to investigate the beam properties at different wavelengths, mainly those used to perform refractive surgery in our research. For this purpose, different wavelengths in SWIR were generated by using non-linear crystals in a geometry based on Optical Parametric Generation (OPG) and Optical Parametric Amplification (OPA). This work helped us to fully optimise the beams quality: spatial profile and its stability. An experimental setup was proposed in order to determine the spot size of focused laser beam inside tissue. Results obtained on an anisotropic diffuser were in good agreement with the expectations.

In this latest report, we describe experiments which use the abilities of the camera and the previous optimisations to investigate optical and structural properties of porcine corneas. By the means of Fourier Optics, we firstly investigate the focal spot of a laser beam focused at the back (endothelium) of corneas. Then, by moving the sample, we studied the changes of the focused beam at different depth of the cornea.

1.3 Materials and Methods

For this study, healthy porcine eyes were obtained under the permission of local authorities from a local slaughterhouse. The thicknesses of the corneas were firstly measured by ultrasonic pachymetry (Tomey, United States). The corneas were then carefully extracted from the eye and washed in a balanced salt solution. For our experiment that requires a flat surface, these latest were sandwiched between two microscope coverslips (Menzel Gläser, Germany).



Fig.2: Picture of a healthy porcine cornea set between two microscope coverslips.

Figure 3 shows the experimental setup used to investigate the spot size of the laser beam inside the cornea as a function of thickness. A diode pumped femtosecond laser system emitting at the wavelength 1030 nm was used as a source. The generated beam was expanded with the help of a beam expander, then focused by the means of a microscope objective with a numerical aperture of 0.45 (Olympus, Japan) inside the sample (porcine cornea). The transmitted beam was then re-collimated by another microscope objective with a numerical aperture of 0.65 (Nacht, France) and finally focused by an achromatic doublet lens of 200 mm (AC508-200-C-ML, Thorlabs, Germany) onto the NEXPRESSO camera sensor. This latest focal plane correspond to the Fourier plane where one can observe the spatial distribution of frequencies of the beam transmitted through the sample structure located between the two microscope objectives.

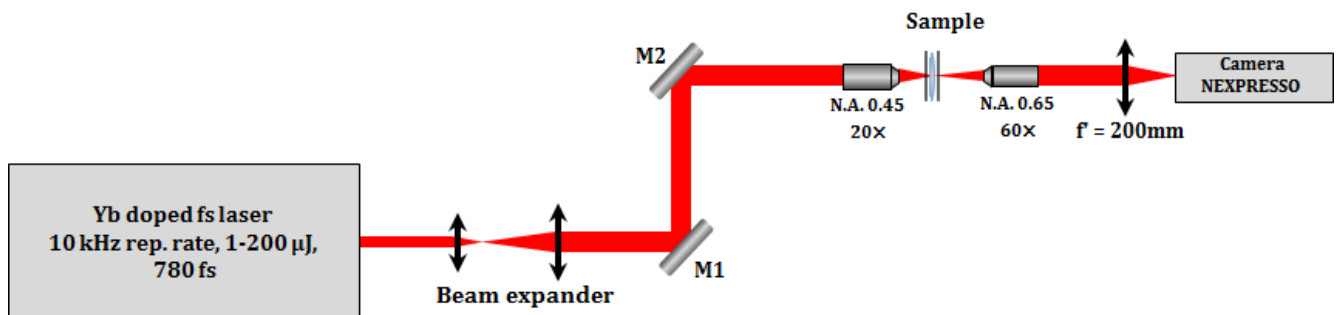


Fig.3: *Experimental setup use to investigate the spot size of the laser beam.*

1.4 Results and discussion

Focal spot with and without cornea

The laser beam spot sizes measured on the camera whose sensor was located at the focal plane were compared with and without sample as shown in figure 4. Figure 4.A represents the case of the focal spot of a beam propagating through the optical system without sample. Figure 4.B shows the case with a sample where the laser beam crosses the whole thickness of the cornea and focused on the endothelium.

For both cases, an example of images obtained for the focused beam spot detected on the camera are given. The comparison of these images reveals a slight broadening of the focused beam spot when the cornea is placed between both microscopes objectives. This broadening is attributed to the structure of the cornea that affects the laser beam spot in the focal plane.

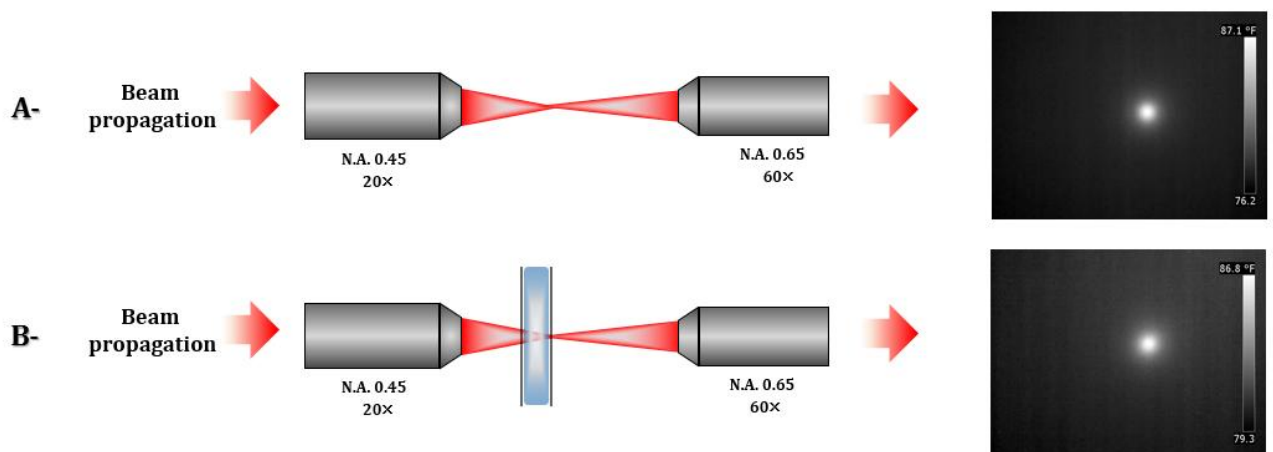


Fig. 4: Schematic of the experimental setup used to investigate the structures of the porcine corneas. (A) Without sample in between the two microscope objective, (B) With the cornea in between the two microscope objective.

The raw images acquired by the camera were processed and analysed using MATLAB software. The corresponding 3D profiles were obtained by converting the gray scale to Z coordinates. Figure 5 and 6 show the resulting 3D profiles measured for corneas with thicknesses of 641 μm and 867 μm respectively. For each case, the profile was normalized and compared to the one obtained without sample. In comparison to the focal spot in air the beam that passes through a clear cornea with a thickness of 641 μm got broadened. For our application in corneal surgery, this broadening may affect the laser procedure in two different ways. First, the Strehl ratio will be lower which means that a higher amount of energy will be required to make incisions. The second point is that more energy will be dissipated in the vicinity of the incision, which can damage the tissue around it. The same phenomenon was also observed for cornea 2 with a thickness

of $867 \mu\text{m}$ (Fig. 6). For all cases, full widths at half maximum (FWHM) were determined on X and Y profiles. Figures 7 and 8 show the transversal cuts of the beam profiles at FWHM and clearly indicate a larger value for FWHM in the presence of the sample.

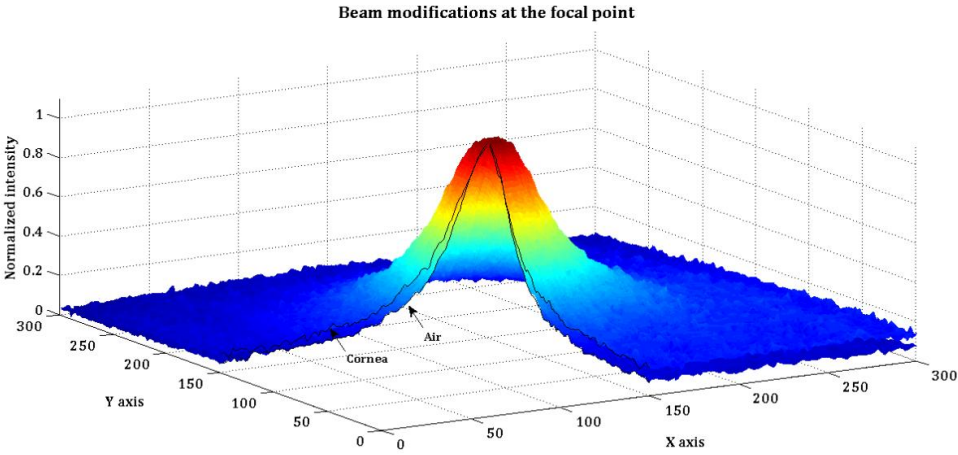


Fig. 5: Comparison of the focal spot when it passes through air and cornea 1 ($641 \mu\text{m}$)

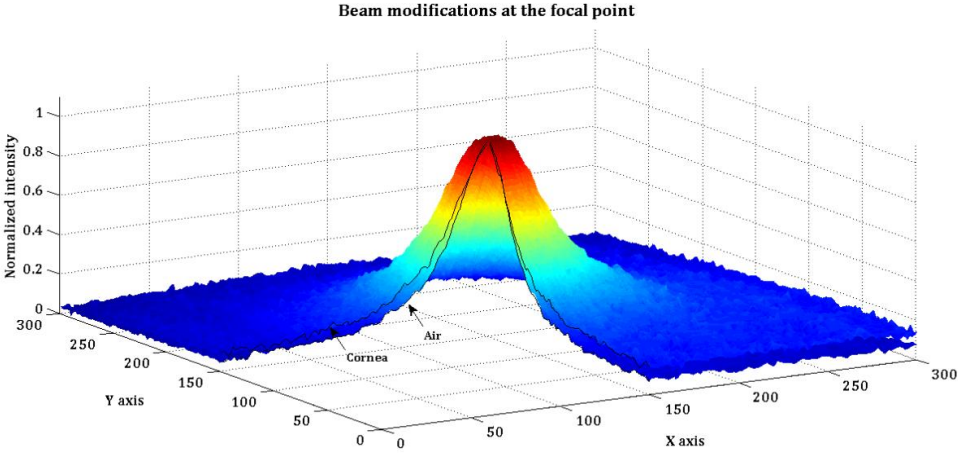


Fig. 6: Comparison of the focal spot when it passes through air and cornea 2 ($867 \mu\text{m}$)

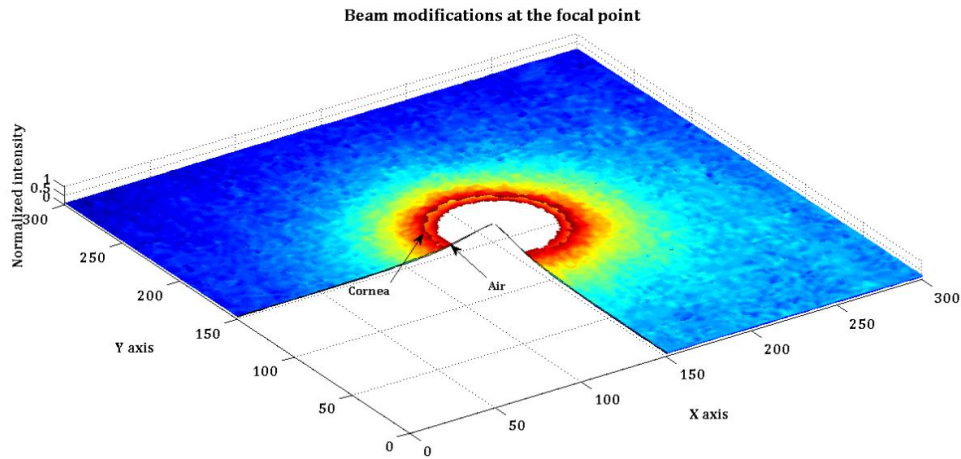


Fig. 7: Comparison of FWHM when the beam passes through the air and through the cornea 1 (641 μm)

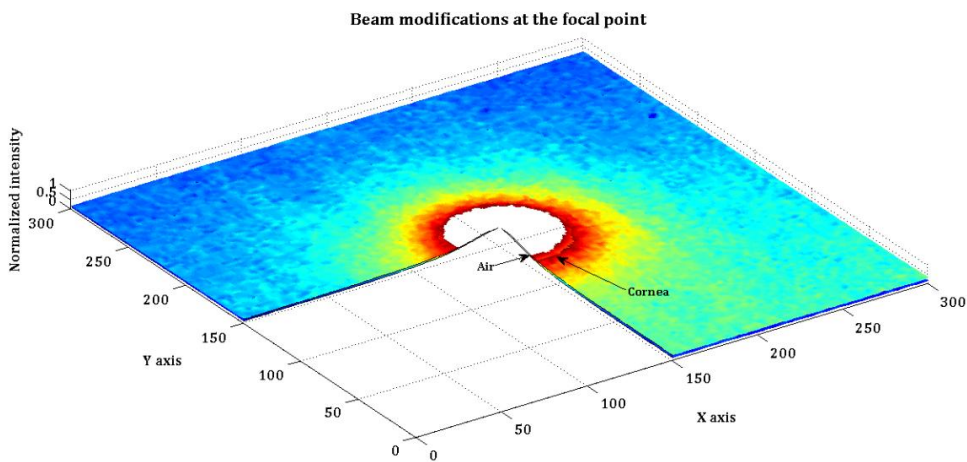


Fig. 8: Comparison of FWHM when the beam passes through the air and through the cornea 2 (867 μm)

Spot size at different planes inside the cornea

For the experiment shown in figure 9, we used the same experimental set-up as described previously (figure 3). However, to probe different planes inside the cornea and their effects on the beam spot, the sample was moved with a motorized z-stage. The thickness of the cornea was divided into 10 equally spaced planes. The beam spot at the focal plane on the camera associated to each position was recorded and processed to extract quantitative data such as the FWHM. The initial position (the zero) represents the posterior side (endothelium) of the cornea and the latest position represents the anterior side (epithelium).

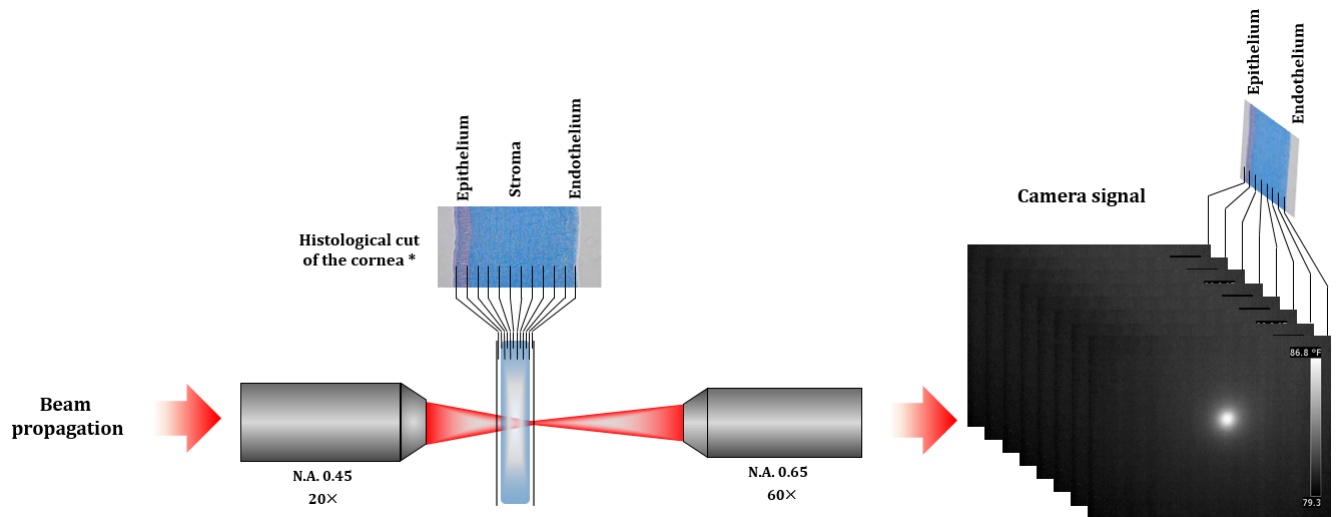


Fig. 9: Schematic of the procedure that was used in this case. The thickness of the cornea was divided into ten equally separated planes. For each plane we imaged the focal spot. Where the zero represents the posterior side (endothelium) of the cornea and the highest position represents the anterior side (epithelium).

For each cornea, a set of two measurements performed at different positions were taken into account. The FWHM was determined on normalized X and Y profiles of the beam spot approximated by a Gaussian function and averaged. The depth probing on the cornea allows us to investigate the changes in the beam spot within a layered structure. The variation of the focal beam spot on the camera is given in terms of FWHM for each position inside the cornea. Figures 10 and 11 show the evolution obtained for a cornea (Cornea 1) with an average thickness of $641\ \mu\text{m}$ and a cornea (Cornea 2) with an average thickness of $867\ \mu\text{m}$, respectively. For both locations within a same cornea, one can see the decrease of the focal beam spot size as we go towards the anterior side of the cornea. Since we are able to probe these changes for clear corneas, these results appear to be promising for oedematous cases and show that the camera resolution and sensitivity are appropriate for investigating the corneas' properties. Due to the small variations in the FWHM values, additional corneas are under study. The wavelength dependence for this experiment is currently under investigation.

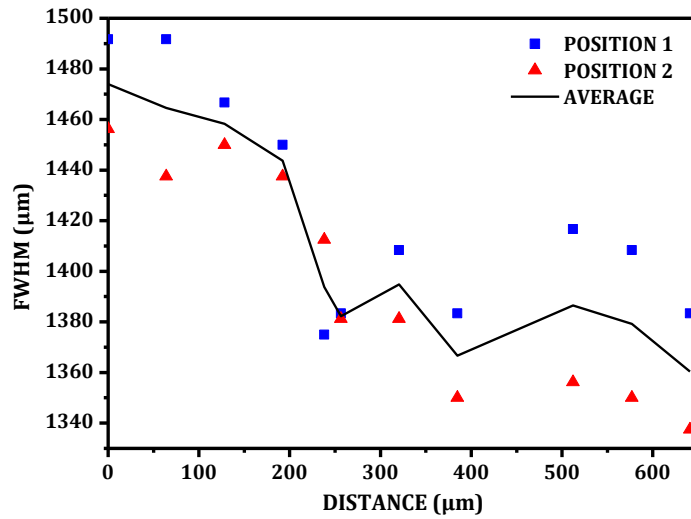


Fig. 10: Averaged FWHM values obtained along the x and y profiles of the beam spot measured on the camera. The full squares and triangles represent calculated FWHM for two different positions on the cornea of 641 μm thickness. The black line shows their average.

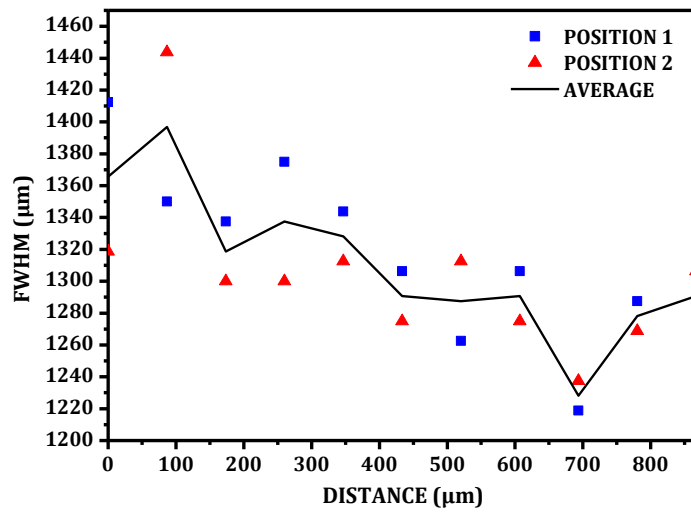


Fig. 11: Averaged FWHM values obtained along the x and y profiles of the beam spot measured on the camera. The full squares and triangles represent calculated FWHM for two different positions on the cornea of 867 μm thickness. The black line shows their average.

On figure 12, we reported the averaged FWHM depth evolution obtained on both corneas (Cornea1 and Cornea2). The comparison of both measurements show a same trend in the FWHW values of the focal beam spot changes.

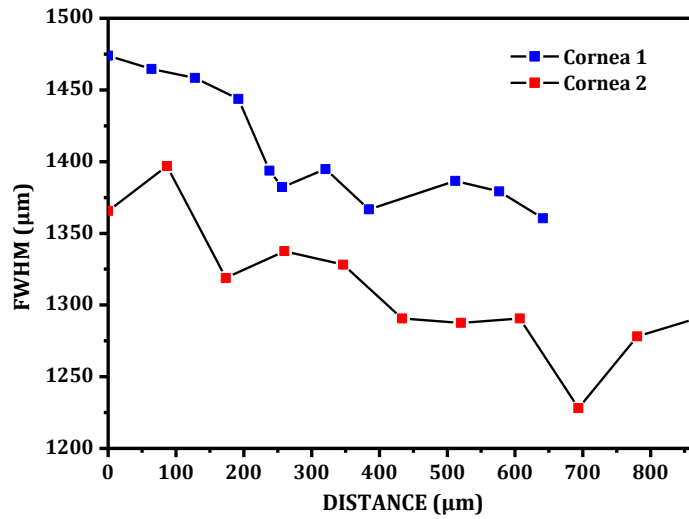


Fig. 12: Average FWHM for the case of cornea 1(641 μm) and cornea 2(867 μm).

1.5 Conclusion

In conclusion, we developed an experimental set-up to investigate the spatial frequency spectrum of beams having interacted with light scattering objects. A beam is firstly focused on the sample with a microscope objective, then refocused on the NEXPRESSO camera sensor (Fourier plane). The resulting beam spot in the Fourier plane was recorded and the collected images were processed using MATLAB software in terms of 3D shape and FWHM values. The results obtained show a broadening of the beam spot in the Fourier plane in presence of corneas with respect to the profile measured in the absence of the sample (in the air). The measurements were performed at different depths inside the cornea. The results are preliminary and will require additional measurement for stable statistics and a wavelength dependence study.

Main conclusion

By acquiring a multi-wavelength camera TeraCam under the NEXPRESSO project, several targets were achieved:

- ✓ Beam characterization measurements

After the full testing and characterization of the NEXPRESSO camera, a method to treat the obtained images was developed and optimised. The NEXPRESSO camera was used to investigate the beam quality of the laser beams generated by nonlinear optical systems. We have analysed different properties of the laser beam for our system developed for corneal surgery. We were able to

optimise the beam quality and to demonstrate the long term stability of the generated sources.

The obtained results are promising and a paper will be submitted soon.

✓ Tissue characterisation measurements

We developed an experimental setup involving Fourier optics to investigate the focal spot of a laser beam focused at the back (endothelium) of corneas. The corneas were extracted from healthy pig eyes. The set-up was used to investigate the changes in the spatial frequencies of objects placed in an afocal system. The presence of a structured medium such as the corneas at the focal point showed the beam keeps its spatial symmetry but exhibits a broadening related to the structure of the corneas. Further analyses for edematous cases are under study.

In a second experiment, we probed the FWHM of the refocused beam spot in the Fourier plane for several planes inside the cornea. The obtained results showed that the camera was sensitive to the changes in the thickness of the corneas, and the evolution of the FWHM with the thickness are reproducible.

We further developed a digital holographic experimental set up for several wavelengths and associated numerical tools. Its application to the study of corneal optics is currently underway.

References

- [Aaa94] A.A. Angelutz, D.P. Krindach, A.V. Pakulev, V.I. Surmii, “*Kerr lens modulation processes in femtosecond Ti:sapphire laser*”, SPIE Proceedings Vol. 2095, pp.73-76 (1994).
- [Aco07] A. Couairon and A. Mysyrowicz, “*Femtosecond filamentation in transparent media*”, PhR 441, 47-189 (2007).
- [Ada97] A. Daxer, P. Fratzl, “*Collagen fibril orientation in the human corneal stroma and its implication in keratoconus.*” IOVS, 38(1):121-9, (1997).
- [Aga97] A. Galvanauskas, M. A. Arbore, M. M. Fejer, M. E. Fermann, and D. Harter, “*Fiber-laser-based femtosecond parametric generator in bulk periodically poled LiNbO₃*” Opt. Lett. 22, 105 (1997).
- [Akk07] A. K. Khurana “*Comprehensive ophthalmology, fourth edition*” New Age International (P) Ltd., Publishers New Delhi, India, (2007).
- [All07] Allan, B.D., Terry, M.A., Price Jr, F.W., Price, M.O., Griffin, N.B. and Claesson, M., “*Corneal transplant rejection rate and severity after endothelial keratoplasty,*” Cornea 26(9), 1039-42 (2007).
- [Aly04] Al-Yousuf, N, Mavrikakis, I, Mavrikakis, E, and Daya, S. M., “*Penetrating keratoplasty: indications over a 10 year period,*” Br. J. Ophthalmol. 88(8), 998–1001, (2004).
- [Ash06] Anjali Shah, “*External Cavity Diode Lasers and Non-Linear Optical Frequency Conversion in Spectroscopic Applications*”, PhD thesis, University of St Andrews, (2006).
- [Bea07] B. E. A. Saleh and M. C. Teich. *Fundamentals of Photonics*. Hardcover,(2007).
- [Bfj08] B. F. Johnston, “*Fabrication and characterisation of poled ferroelectric optical crystals*”, PhD thesis, Macquarie University, (2008).
- [Car] <http://www.cardiff.ac.uk/optom/contactsandpeople/research/young-rob.html>
- [Cas91] C. A. Sacchi, “*Laser-induced electric breakdown in water*” JOSA B, Vol.8, 337, (1991).
- [Cbo03] C. Boote, S. Dennis, R. H. Newton, H. Puri and K. M. Meek, “*Collagen fibrils appear more closely packed in the prepupillary cornea- optical and biomechanical implications*”, IOVS, 44, 2941-2948, (2003).
- [Cbo05] C. Bootea, S. Dennisa, Y. Huangb, A. J. Quantocka, K. M. Meeka, “*Lamellar orientation in human cornea in relation to mechanical properties*”, Journal of Structural Biology, 149, 1–6, (2005).
- [Cbs01] C. B. Schaffer, *Interaction of Femtosecond Laser Pulses with Transparent Materials*, Ph.D. Thesis, Harvard University, (2001).
- [Ccr13] C. Crotti, F. Deloison, F. Alahyane, F. Aptel, L. Kowalczyk, J.-M. Legeais, D. A. Peyrot, M. Savoldelli, and K. Plamann, “*Wavelength Optimization in Femtosecond Laser Corneal Surgery*”, IOVS, Vol. 54 , No. 5, 3341, (2013).
- [Cew10] C. E. Willoughby ,D. Ponzin , S. Ferrari , A. Lobo , K. Landau , and Yadollah Omidi PhD,“*Anatomy and physiology of the human eye: effects of mucopolysaccha-*

-
- ridoses disease on structure and function – a review*ceo_2363 2..11”, *Clinical and Experimental Ophthalmology*, 38, 2–11, (2010).
- [Cfa08] C. Faber, E. Scherfig, J. Ulrik Prause, and K. E. Sørensen, “*Corneal Thickness in Pigs Measured by Ultrasound Pachymetry In Vivo*”, *Scand. J. Lab. Anim. Sci.*, 35(1), (2008).
- [Cgd12] C. G. Durfee, T. Storz, J. Garlick, S. Hill, Jeff A. Squier, M. Kirchner, G. Taft, K. Shea, H. Kapteyn, M. Murnane, and S. Backus, “*Direct diode-pumped Kerr-lens mode-locked Ti:sapphire laser*”, *OPT. EXP.*, Vol. 20, 13, (2012).
- [Cho97] C. Horvath, A. Braun, H. Liu, T. Juhasz, and G. Mourou, “*Compact directly diode-pumped femtosecond Nd:glass chirped-pulse-amplification laser system*”, *Opt. Lett.* 22, 1790, (1997).
- [Ckh06] C.K. Hitzenger, E. Götzinger, M. Pircher, “*Birefringence properties of the human cornea measured with polarization sensitive optical coherence tomography*”, *Bull. Soc. belge Ophtalmol.*, 302, 153-168, (2006).
- [Cmc98] C. McGowan, D. T. Reid, Z. E. Penman, M. Ebrahimzadeh, and W. Sibbett, “*Femtosecond optical parametric oscillator based on periodically poled lithium niobate*”, *J. Opt. Soc. Am. B*, Vol. 15 No. 2, 694-701, (1998).
- [Cme07] C. Meltendorf, C. Ohrloff, P. Rieck, J. Schroeter, “*Endothelial cell density in porcine corneas after exposure to hypotonic solutions*”, *Graefes Arch Clin Exp Ophthalmol.*, 245(1),143-7, (2007).
- [Cru04] C. Rullière, *Femtosecond laser pulses: principles and experiments*. 2004, Springer.
- [Csc02] C. Schaffer, N. Nishimura, E. Glezer, A. Kim, and E. Mazur, “*Dynamics of femtosecond laser-induced breakdown in water from femtoseconds to microseconds*”, *Opt. Express* 10, 196-203, (2002).
- [Dab11] D. Abdollahpour, D. G. Papazoglou, and S. Tzortzakis, “*Four-dimensional visualization of single and multiple laser filaments using in-line holographic microscopy*”, *Phys. Rev. A* 84, 053809, (2011).
- [Dap10] D.A. Peyrot, F. Aptel, C. Crotti, F. Deloison, S. Lemaire, T. Marciano, S. Bancelin, F. Alahyane, L. Kowalczyk, M. Savoldelli, J.-M. Legeais, K. Plamann, “*Effect of Incident Light Wavelength and Corneal Edema on Light Scattering and Penetration: Laboratory Study of Human Corneas*”, *J. Refract. Surg.* 26, 786-795, (2010).
- [Dbr15] D. Brewster, “*Experiments on the de-polarization of light as exhibited by various mineral, animal and vegetable bodies with a reference of the phenomena to the general principles of polarization*,” *Philos. Trans. R. Soc. London* 1, 21–53, (1815).
- [Ddb08] D. D. Brouwere, H. Ginis, G. Kymionis, I. Naoumidi, and Ioannis Pallikaris, “*Forward Scattering Properties of Corneal Haze*”, *Optometry and Vision Science*, Vol. 85, No. 9, (2008).
- [Des91] D. E. Spence, P. N. Kean, and W. Sibbett, “*60-fs pulse generation from a self-modelocked Ti: sapphire laser*”, *Optics Letters*, 16, 42-44, (1991).
- [Dfa12] D. Faccio, E. Rubino, A. Lotti, A. Couairon, A. Dubietis, G. Tamošauskas, D. G. Papazoglou, and S. Tzortzakis, “*Nonlinear light-matter interaction with femtosecond high-angle Bessel beams*”, *Phys. Rev. A* 85, 033829, (2012).
- [Dgd06] D. G. Dawson, M. A. Watsky, D. H. Geroski and H. F. Edelhauser, “*Cornea and Sclera*”, Chapter 4, *Duane’s ophthalmology*, (2006).
-

-
- [Dge06] D. Geskus, “*Design and construction of regenerative amplifier and compressor for chirped pulse amplification*”, PhD thesis, University of Twente, (2006).
- [Dgp07] D. G. Papazoglou, I. Zergioti, and S. Tzortzakis, “*Plasma strings from ultraviolet laser filaments drive permanent structural modifications in fused silica*”, *Opt. Lett.* 32, 2055-2057, (2007).
- [Dgp08] D. G. Papazoglou and S. Tzortzakis, “*In-line holography for the characterization of ultrafast laser filamentation in transparent media*”, *Appl. Phys. Lett.* 93, 041120, (2008).
- [Dgr79] D. Grand, A. Bernas, E. Amouyal, “*Photoionization of aqueous indole; conduction band edge and energy gap in liquid water*”, *Chem Phys*, Vol. 44, 73, (1979).
- [Dhj06] D.H.Jundt, “*Temperature-dependent Sellmeier equation for the index of refraction, n_e , in congruent lithium niobate*” *Opt. Letts.* 22, 1553, (1997).
- [Dik08] Dijkink, R., S. Le Gac, ., C.-D. Ohl. “*Controlled cavitation-cell interaction: transmembrane transport and viability studies*”. *Phys. Med. Biol.* 53:375–390, (2008).
- [Djj06] D. J. JOHN PARK and JAMES KARESH, “*Topographic Anatomy of the Eye: An Overview*”, Chapter 1, Duane’s ophthalmology, (2006).
- [Dmm72] D. M. Maurice, “*The location of the fluid pump in the cornea*”, *J Physiol.*, 221(1), 43–54, (1972).
- [Dmm84] D.M. Maurice: *The Eye: “The Cornea and Sclera”*, 3rd ed. New York: Academic Press, (1984).
- [Dnn83] D. N. Nikogosyan, A. A. Oraevsky, V. I. Rupasov, “*Two-photon ionization and dissociation of liquid water by powerful laser UV irradiation*”, *Chem Phys* Vol. 77, 131, (1983).
- [Dpa14] D. Papazoglou, D. Abdollahpour, and S. Tzortzakis, “*Ultrafast electron and material dynamics following femtosecond filamentation induced excitation of transparent solids*”, *Applied Physics A* 114, 161-168, (2014).
- [Drd12] Duna Raoof-Daneshvar, Roni M Shtein, “*Femtosecond Lasers in Ophthalmology*” *US Opht. Rev.*, 6(1), (2013).
- [Dsa10] D. Sacchet, “*Tomographie par coherence optique plein champ lineaire et non lineaire*”, PhD these , Laboratoire Charles Fabry de l’Institut d’Optique, (2010).
- [Dsh07] D. S. Hum, M. M. Fejer, “*Quasi-phasematching*”, *C. R. Physique* 8, 180–198, (2007).
- [Eab62] E. A. Boettner, and Wolter JR. “*Transmission of the ocular media*”, *IOVS*,1, 776-783, (1962).
- [Egö07] E. Götzinger, M. Pircher, I. Dejaco-Ruhswurm, S. Kaminski, C. Skorpik, and C. K. Hitzenberger, “*Imaging of birefringent properties of keratoconus corneas by polarization-sensitive optical coherence tomography*,” *Invest. Ophthalmol. Vis. Sci.* 48(8), 3551–3558, (2007).
- [Eso01] E. Sorokin, I.T. Sorokina and E. Wintner., “*Diode-pumped ultrashort-pulse solid-state lasers*”, *Appl. Phys. B* 72, 3, (2001).
- [Fmo09] F. Morin, F. Druon, M. Hanna, and P. Georges, “*Microjoule femtosecond fiber laser at 1.6 μm for corneal surgery applications*”, *Opt. Lett.*, Vol. 34, 13, (2009).
-

-
- [Fsa02] F. Salin, A. Courjaud, R. Maleck-Rassoul, N. Deguil and C. Hönninger, “*Advances in Solid State Lasers*” (Trends in Optics and Photonics Series vol 68) ed M Fermann and L Marshall (Washington, DC: Optical Society of America) paper MC2, (2002).
- [Fwi76] F. Williams, S. P. Varma and S. Hillenius, “*Liquid water as a lone-pair amorphous semiconductor*”, J Chem Phys, Vol. 64, 1549, (1976).
- [Gbb71] G. B. Benedek, “*Theory of Transparency of the Eye*”, Applied Optics, 10: 459-473, (1971).
- [Gks60] G.K. Smelser, “*The transparency of the cornea*”. Oxford: Blackwell, (1960).
- [Gol08] G. Olivie, D. Giguère, F. Vidal, T. Ozaki, J.-C. Kieffer, O. Nada, and I. Brunette, “*Wavelength dependence of femtosecond laser ablation threshold of corneal stroma*”, Optics Express, Vol. 16, 4121, (2008).
- [Gow82] G. O. Waring, W. M. Bourne, H. F. Edelhauser, K. R. Kenyon, “*The corneal endothelium: normal and pathologic structure and function*”, Ophthalmology 89:531, (1982).
- [Gpa03] G. Paltauf, P.E. Dyer, “*Photomechanical processes and effects in ablation*”, Chemical reviews 103 (2), 487-518, (2003).
- [Gpa99] G. Paltauf, H. Schmidt-Kloiber, “*Photoacoustic cavitation in spherical and cylindrical absorbers*”, Applied Physics A, Volume 68, Issue 5, pp 525-531, (1999).
- [Grm06] GR Melles, T San Ong, B Ververs, J van der Wees, “*Descemet membrane endothelial keratoplasty (DMEK)*”, Cornea, Vol.25, 987, (2006).
- [Hel08] Hellman, A. N., K. R. Rau, ., V. Venugopalan “*Biophysical response to pulsed laser microbeam-induced cell lysis and molecular delivery*”. J. Biophotonics. 1:24–35, (2008).
- [Hfe00] H. F. Edelhauser, “*Castroviejo Lecture: The resiliency of the corneal endothelium to refractive and intraocular surgery*”, Cornea 19,263, (2000).
- [Hhu10] H. Hu, X. Wang, H. Zhai, N. Zhang and P. Wang, “*Generation of multiple stress waves in silica glass in high fluence femtosecond laser ablation*”, Appl. Phys. Lett. 97, 061117 (2010).
- [Hks09] H. K. Soong; J. B. Malta, “*Perspective Femtosecond Lasers in Ophthalmology*” AJO, 147(2), 189-197 (2009).
- [Hsd13] H. S. Dua, L. A. Faraj, D. G. Said, T. Gray, and J. Lowe, “*Human Corneal Anatomy Redefined : A Novel Pre-Descemet's Layer (Dua's Layer)*”, Ophthalmology, Volume 120, Issue 9, 1778, (2013).
- [Hsd14] H. S Dua, L. A Faraj, M. J Branch, A. M. Yeung, M. S. Elalfy, D. G. Said, T. Gray, and J. Lowe, “*The collagen matrix of the human trabecular meshwork is an extension of the novel pre-Descemet's layer (Dua's layer)*”, Br J Ophthalmol, (2014).
- [Ije14] I.J.E. van der Meulen, “*Straylight in anterior segment disorders of the eye*”, Dissertation, University of Amsterdam, (2014).
- [Ima06] I. Maxwell, “*Application of femtosecond lasers for subcellular nanosurgery*”, Doctoral thesis, Harvard University, (2006).
- [Isa11] I. Sanchez, R. Martin, F. Ussa and I. Fernandez-Bueno, “*The parameters of the porcine eyeball*”, Graefes Arch Clin Exp Ophthalmol, 249, 475–482, (2011).

-
- [Jaa62] Armstrong, J.A., N. Bloembergen, J. Ducuing, and P.S. Pershan, *Interactions between Light Waves in a Nonlinear Dielectric*, Physical Review 127 (6) 1918-1939, (1962).
- [Jam03] J. Amann, G. P. Holley, S. B. Lee, H. F. Edelhauser, “*Increased endothelial cell density in the paracentral and peripheral regions of the human cornea*”. Am J Ophthalmol 135:584, (2003).
- [Jkr13] J. Krauth, A. Steinmann, R. Hegenbarth, M. Conforti, and H. Giessen, “*Broadly tunable femtosecond near- and mid-IR source by direct pumping of an OPA with a 41.7 MHz Yb:KGW oscillator*” Opt. Exp. 11516, Vol. 21, No. 9, (2013).
- [Jng67] J. N. Goldman, and G. B. Benedek, “*The relationship between morphology and transparency in the nonswelling corneal stroma of the shark*”, Investigative Ophthalmology 6: 574-600, (1967).
- [Jno98] J. Noack, A. Vogel, “*Single-Shot Spatially Resolved Characterization of Laser-Induced Shock Waves in Water*” Appl. Opt. 37, 4092, (1998).
- [Jon13] Jonathan L. Compton, Amy N. Hellman, and Vasani Venugopalan, “*Hydrodynamic Determinants of Cell Necrosis and Molecular Delivery Produced by Pulsed Laser Microbeam Irradiation of Adherent Cells*”, Biophysical Journal Vol. 105 , 2221–2231, (2013).
- [Jsc12] Johannes Schindelin, Ignacio Arganda-Carreras, Erwin Frise, Verena Kaynig, Mark Longair, Tobias Pietzsch, Stephan Preibisch, Curtis Rueden, Stephan Saalfeld, Benjamin Schmid, Jean-Yves Tinevez, Daniel James White, Volker Hartenstein, Kevin Eliceiri, Pavel Tomancak and Albert Cardona “*Fiji: an open-source platform for biological-image analysis*”, Nature Methods 9(7): 676-682, (2012).
- [Jwa04] J. Wang, T. L. Simpson, and D. Fonn, “*Objective Measurements of Corneal Light-Backscatter during Corneal Swelling, by Optical Coherence Tomography*”, IOVS, Vol. 45, No. 10, (2004).
- [Svp07] S. V. Patel, E. J. Winter, J. W. McLaren, and W. M. Bourne, “*Objective Measurement of Backscattered Light from the Anterior and Posterior Cornea In Vivo*”, Vol. 48, No. 1, (2007).
- [Kbk06] K. B. Kim, L. M. Shanyfelt, and D. W. Hahn, “*Analysis of dense-medium light scattering with applications to corneal tissue: experiments and Monte Carlo simulations*”, Vol. 23, No. 1, J. Opt. Soc. Am. A, (2006).
- [Koz13] Kemal Ozulken, Florence Cabot, and Sonia H Yoo , “*Applications of femtosecond lasers in ophthalmic surgery*” Expert Review of Medical Devices, Vol. 10, No. 1, (2013).
- [Lja08] L. Jay, A. Brocas, K. Singh, J.-C. Kieffer, I. Brunette, and T. Ozaki, “*Determination of porcine corneal layers with high spatial resolution by simultaneous second and third harmonic generation microscopy*”, Optics Express, Vol. 16, Issue 21, pp. 16284-16293 (2008).
- [Ljb91] L.J. Bour, “*Polarized light and the eye*”, Visual optics and instrumentation, CRC Press, Boca Raton, FL, 310-325 , (1991).
- [Lku07] L. Kuznetsova and F. W. Wise, “*Scaling of femtosecond Yb-doped fiber amplifiers to tens of microjoule pulse energy via nonlinear chirped pulse amplification*”, Optics Letters, Vol. 32, Issue 18, pp. 2671-2673, (2007)

-
- [Lln95] Taken and modified from LLNL S&TR of September 1995(https://www.llnl.gov/str/pdfs/09_95.2.pdf).
- [Lvk65] L. V. Keldysh, “*Ionization in the field of a strong electromagnetic wave*”, Soviet Physics JETP, Vol. 20, 1307, (1965).
- [Mcs04] M. Csele, “*Fundamentals of light sources and lasers*”, John Wiley & Sons, Inc, (2004).
- [Mgd99] M. G. Ducros, J. F. de Boer, H. E. Huang, L. C. Chao, Z. P. Chen, J. S. Nelson, T. E. Milner, and H. G. Rylander, “*Polarization sensitive optical coherence tomography of the rabbit eye,*” IEEE J. Sel. Top. Quantum Electron. 5, 1159–1167, (1999).
- [Mha09] M. Hanna, D. Papadopoulos, F. Druon, and P. Georges, “*Distributed nonlinear fiber chirped-pulse amplifier system*”, Optics Express, Vol. 17, Issue 13, pp. 10835-10840, (2009).
- [Mhn93] M. H. Niemz, *Laser-Tissue Interactions: Fundamentals and Applications*. Berlin, Heidelberg, New York: Springer-Verlag, 3rd ed., (1996).
- [Mjh71] M. J. Hogan, J.A. Alvarado, J. E. Weddell, “*Histology of the Human Eye*”, Philadelphia, WB Saunders, (1971).
- [Mjo03] M. J. Orozco-Arellanes, R. S. Cudney, “*Indirectly-seeded optical parametric generation in periodically poled lithium niobate*” Opt. Exp., Vol. 11, Issue 1, 20-26, (2003).
- [Mks06] M. K. Smolek and S. D. Klyce, “*Cornea*”, Chapter 8, Duane’s Ophthalmology, (2006).
- [Mlb95] M. L. Bortz, M. A. Arbore, and M. M. Fejer, “*Quasi-phase-matched optical parametric amplification and oscillation in periodically poled LiNbO₃ waveguides*” Opt. Lett., Vol. 20, No. 1, (1995).
- [Mle13] M. LEVENIUS, “*Optical parametric devices in periodically poled LiTaO₃*”, Doctoral Thesis, Royal Institute of Technology, (2013).
- [Mma07] M. Marangoni, R. Osellame, R. Ramponi, G. Cerullo, A. Steinmann, and U. Morgner, “*Near-infrared optical parametric amplifier at 1 MHz directly pumped by a femtosecond oscillator*” OPTICS LETTERS / Vol. 32, No. 11 1489, (2007).
- [Mmj11] M. M. Jawad, S. T. A. Qader, A.A. Zaidan, B.B. Zaidan, A.W. Naji and I. T. Abdul Qader, “*An Overview of Laser Principle, Laser-Tissue Interaction Mechanisms and Laser Safety Precautions for Medical Laser Users. International Journal of Pharmacology*”, 7: 149-160, (2011).
- [Mpa13] M. Parekh, G. Salvalaio, A. Ruzza, D. Camposampiero, C. Griffoni, A. Zampini, D. Ponzin, and Stefano Ferrari, “*Posterior Lamellar Graft Preparation: A Prospective Review from an Eye Bank on Current and Future Aspects*”, Journal of Ophthalmology, (2013).
- [Mra02] M. Rahm, U. Bäder, G. Anstett, J.-P. Meyn, R. Wallenstein and A. Borsutzky, “*Pulse-to-pulse wavelength tuning of an injection seeded nanosecond optical parametric generator with 10 kHz repetition rate*”, Appl. Phys. B 75, 47–51, (2002).
- [Mus] <http://musom.marshall.edu/>
- [Mye] <http://www.myeyes.com/>

-
- [NcJ03] N. C. Joyce, “*Proliferative capacity of the corneal endothelium*”, Prog. Retin. Eye Res., 22, 359-89, (2003).
- [Nid] Nidek Technologies.
- [Noa98] J. Noack, D. X. Hammer, G. D. Noojin, B. A. Rockwell, A. Vogel , “*Influence of pulse duration on mechanical effects after laser-induced breakdown in water*”. J Appl Phys 83:7488-7495, (1998).
- [Nob10] N. Linz, “*Controlled Nonlinear Energy Deposition in Transparent Dielectrics by Femtosecond and Nanosecond Optical Breakdown*” Phd thesis, University of Lübeck, (2010).
- [Nta07] N. Takahashi, M. Wakuta, N. Morishige, T.-I. Chikama, T. Nishida, and Y. Sumii, “*Development of an Instrument for Measurement of Light Scattering at the Corneal Epithelial Basement Membrane in Diabetic Patients*” Jpn J Ophthalmol, 51:185–190, (2007).
- [Osa06] Olan Suwan-Apichon, Johann M G Reyes, Neil B Griffin, Jerry Barker, Patrick Gore, Roy S Chuck, “*Microkeratome versus femtosecond laser pre-dissection of corneal grafts for anterior and posterior lamellar keratoplasty*”, Cornea, (2006).
- [Per] Personal communication with colleagues at University hospital, Université Jean Monnet, Saint-Étienne, France.
- [Pip11] Pipparelli, A., Thuret, G., Toubeau, D., He, Z., Piselli, S., Lefèvre, S., Gain, P. and Muraine, M., “*Pan-Corneal Endothelial Viability Assessment: Application to Endothelial Grafts Pre-dissected by Eye Banks*” IOVS, 52(8), (2011).
- [Pla10] K. Plamann, F. Aptel, C. Arnold, A. Courjaud, C. Crotti, F. Deloison, F. Druon, P. Georges, M. Hanna, J.-M. Legeais, F. Morin, É. Mottay, V. Nuzzo, D. A. Peyrot, M. Savoldelli, “*Ultrashort pulse laser surgery of the cornea and the sclera*”, J. Opt. 12, 084002, (2010).
- [Pru79] P Ruusuvaara, “*Effects of corneal preservation, donor age, cadaver time and postoperative period on the graft endothelium*”, Acta ophthalmologica, 57(5):868-81, (1979).
- [Pwr11] Peter W. Roth, Alexander J. Maclean, David Burns and Alan J. Kemp, “*Direct diode-laser pumping of a mode-locked Ti:sapphire laser*”, OPT. LETT. , Vol. 36, 2, (2011).
- [Rau04] K. R. Rau, A. G. Guerra, III, ., V. Venugopalan, “*Investigation of laser-induced cell lysis using time-resolved imaging*”, Appl. Phys. Lett. 84:2940–2942, (2004).
- [Rau06] Rau, K. R., P. A. Quinto-Su, V. Venugopalan “*Pulsed laser microbeam-induced cell lysis: time-resolved imaging and analysis of hydrodynamic effects*”. Biophys. J. 91:317–329, (2006).
- [Rba06] R. Blake and R. Sekuler, *Perception*, 5th Edition , McGraw-Hill Higher Education, Burr Ridge, USA, (2006).
- [Rby97] R. Byer, “*Quasi-Phase-matched Nonlinear Interactions and Devices*”, J. Non. Opt. Phy. & mat., Vol. 6 No. 4, 549-592, (1997).
- [Rhn98] NEWTON R.H., MEEK K.M. “*The integration of the corneal limbal fibrils in the human eye*”, Biophysical Journal, 75, 2508–2512, (1998).
- [Riv] <http://www.riverside-eye-center-maine.com/>
-

-
- [Rlb77] R. L. Byer and R.L. Herbst, *Parametric oscillation and mixing, in Nonlinear Infrared Generation*, Y.R. Shen, editor. Springer Berlin Heidelberg. 81-137, (1977).
- [Rlm07] R. L. McCally, D. E. Freund, A. Zom, J. Bonney-Ray, R. Grebe, Z de la Cmz, and W. R. Green, “*Light-scattering and ultrastmcture of healed penetrating corneal wounds*” IOVS, 48: 157-165, (2007).
- [Rrp] www.rp-photonics.com
- [Rwb08] R. W. Boyd, “*Nonlinear optics*”, Academic Press, (2008).
- [Rwh69] R.W. Hart, and R.A. Farrell, “*Light scattering in the cornea*”, JOSA, 59, 6, 766-773, (1969).
- [Rwy85] R. W. Yee, M. Matsuda, R.O. Schultz, and H.F. Edelhauser, “*Changes in the normal corneal endothelial cellular pattern as a function of age*”, Current Eye Research, 4, 671-678, (1985).
- [Sba95] S. Backus, J. Peatross, C. P. Huang, M. M. Murnane, and H. C. Kapteyn , “*Ti:sapphire amplifier producing millijoule-level, 21-fs pulses at 1 kHz*”, Opt. Lett. 20 (19), 2000 (1995).
- [Sck11] S S. C. Kumar, A. Agnesi, P. Dallochio, F. Pirzio, G. Reali, K. T. Zawilski, P. G. Schunemann, and M. Ebrahim-Zadeh, “*Compact, 1.5 mJ, 450 MHz, CdSiP2 picosecond optical parametric oscillator near 6.3 μm* ”, Opt. Lett. Vol. 36 No. 16, 3236-3238 (2011).
- [Shc99] S. H. Cho, B. E. Bouma, E. P. Ippen, and J. G. Fujimoto, “*Low-repetition-rate high-peak-power Kerr-lens mode-locked TiAl_2O_3 laser with a multiple-pass cavity*” Optics Letters, Vol. 24, Issue 6, pp. 417-419 (1999).
- [Shö01] S. Höfer, A. Liem, J. Limpert, H. Zellmer, A. Tünnermann, S. Unger, S. Jetschke, H.-R. Müller, and I. Freitag, “*Single-frequency master-oscillator fiber power amplifier system emitting 20 W of power*”, Optics Letters, Vol. 26, Issue 17, pp. 1326-1328 (2001).
- [Smi08] S. Minardi, A. Gopal, M. Tatarakis, A. Couairon, G. Tamosauskas, R. Piskarskas, A. Dubietis, and P. Di Trapani, “*Time-resolved refractive index and absorption mapping of light-plasma filaments in water*”, Opt. Lett. 33, 86-88, (2008).
- [Spa95] S. Patel, J. Marshall, F. W. Fitzke III, “*Refractive index of the human corneal epithelium and stroma*”, J Refract Surg., 11(2), (1995).
- [Spe] Specification S-Pulse Amplitude Systèmes.
- [Ssa06] S. Saika, “*TGF β pathobiology in the eye*”, Laboratory Investigation 86, 106–115, (2006).
- [Sto] <http://www.stokeseye.com/>
- [Str85] Strickland D and Mourou , “*Compression of amplified chirped optical pulses*”, Optics Communication, 56 219–21, (1985).
- [Tju96] T. Juhasz, G.A. Kastis, C. Suárez , Z. Bor Z, W. E. Bron, “*Time-resolved observations of shock waves and cavitation bubbles generated by femtosecond laser pulses in corneal tissue and water*”, Lasers Surg Med.,19(1),23-31, (1996).
- [Tsu01] T. Südmeyer, J. A. d. Au, R. Paschotta, U. Keller, P. G. R. Smith, G. W. Ross and D. C. Hanna, “*Novel ultrafast parametric systems: high repetition rate single-pass OPG and fibre-feedback OPO*”, J. Phys. D: Appl. Phys. 34, 2433–2439, (2001).
-

-
- [Ukr03] U. Keller, “Recent developments in compact ultrafast lasers”, NATURE, Vol 424, (2003).
- [Vog03] A. Vogel, and V. Venugopalan, “Mechanisms of Pulsed Laser Ablation of biological Tissues”, Chem. Rev., 103, 577-644, (2003).
- [Vog05] A. Vogel, J. Noack, G. Huettmann, G. Paltauf, “Mechanisms of femtosecond laser nanosurgery of cells and tissue”, Appl Phys B 81:1015, (2005).
- [Vog08] A. Vogel, N. Linz, S. Freidank, G. Paltauf, “Femtosecond-Laser-Induced Nanocavitation in Water: Implications for Optical Breakdown Threshold and Cell Surgery”, PRL 100, 038102, (2008).
- [Vpe09] V. Petrov, A. Gaydardzhiev, M. Ghotbi, I. Nikolov, I. Buchvarov, P. Tzankov and Frank Noack, “Femtosecond optical parametric generators and amplifiers for the near infrared based on BiB3O6”, Proc. of SPIE Vol. 7501 750102, (2009)
- [Whl80] W. H. Lowdermilk, “The multipass amplifier: theory and numerical analysis”, J. Appl. Phys. 51 (5), 2436, (1980).
- [Wla13] W. Lauterborn, A. Vogel, “Shock wave emission by laser generated bubbles”, Bubble Dynamics and Shock Waves, 67-103, (2013).
- [Wmb01] W. M. Bourne, “Cellular changes in transplanted human corneas”, Cornea, 20(6):560-9, (2001).
- [Wsi12] W. Sibbett, A. A. Lagatsky, and C. T. A. Brown, “The development and application of femtosecond laser systems” Opt. Exp., Vol. 20, No. 7, (2012).
- [Wsv06] W. S. Vanmeter, W. B. Lee and D.G. Katz, “Corneal Edema”, Chapter 16A, Duane’s ophthalmology, (2006).
- [Ylk04] Y. L Kim, J. T. Walsh Jr, T. K. Goldstick and Matthew R Glucksberg, “Variation of corneal refractive index with hydration”, Phys. Med. Biol., 49, 859–868, (2004).
- [Ypu07] Y. Pu, J. Wu, M. Tsang, and D. Psaltis, “Optical parametric generation in periodically poled KTiOPO4 via extended phase matching”, App. Phy. Lett. 91, 131120, (2007).
- [Yrs92] Y. R. Shen. “The principles of nonlinear optics”. John Wiley & Sons, (1992).
- [Yza08] Y. Zaouter, J. Bouillet, E. Mottay, and E. Cormier “Transform-limited 100 μ J, 340MW pulses from a nonlinear-fiber chirped-pulse amplifier using a mismatched grating stretcher–compressor” Optics Letters, Vol. 33, Issue 13, pp. 1527-1529, (2008)
- [Yze01] Y. Zeng, J. Yang, K. Huang, Z. Lee, and X. Lee, “A comparison of biomechanical properties between human and porcine cornea”, Journal of Biomechanics, 34, 533–537, (2001).
- [Zsu07] Z. Sun, M. Ghotbi and M. Ebrahim-Zadeh, “Widely tunable picosecond optical parametric generation and amplification in BiB3O6” Opt. Exp. Vol. 15, No. 7, 4139-4148, (2007).